MODELING AND SIMULATION OF SHAPED CHARGES

A THESIS SUBMITTED TO
THE GRADUATE SCHOOL OF NATURAL AND APPLIED SCIENCES
OF
MIDDLE EAST TECHNICAL UNIVERSITY

BY

ESER GÜREL

IN PARTIAL FULFILLMENT OF THE REQUIREMENTS
FOR
THE DEGREE OF MASTER OF SCIENCE
IN
MECHANICAL ENGINEERING

JULY 2009

Approval of the thesis:

MODELING AND SIMULATION OF SHAPED CHARGES

submitted by **ESER GÜREL** in partial fulfillment of the requirements for the degree of **Master of Science in Mechanical Engineering Department, Middle East Technical University** by,

Prof. Dr. Zafer Dursunkaya _____
Dean, Graduate School of **Natural and Applied Sciences**

Prof. Dr. Süha ORAL _____
Head of Department, **Mechanical Engineering**

Assoc. Prof. Dr. Cüneyt SERT _____
Supervisor, **Mechanical Engineering Dept., METU**

Examining Committee Members:

Prof. Dr. Orhan YILDIRIM _____
Mechanical Engineering Dept., METU

Prof. Dr. Haluk Aksel _____
Mechanical Engineering Dept., METU

Assoc. Prof. Dr. Cüneyt SERT _____
Mechanical Engineering Dept., METU

Assoc. Prof. Dr. İlker TARI _____
Mechanical Engineering Dept., METU

M.Sc. Eng. Burak TARKAN _____
Warhead Design Team, Mechanical Design Department, Engineering and Development Directorate, ROKETSAN

Date: 24/07/2009

I hereby declare that all information in this document has been obtained and presented in accordance with academic rules and ethical conduct. I also declare that, as required by these rules and conduct, I have fully cited and referenced all material and results that are not original to this work.

Name, Last Name: Eser GÜREL

Signature :

ABSTRACT

MODELING AND SIMULATION OF SHAPED CHARGES

Gürel, Eser

M.Sc., Department of Mechanical Engineering

Supervisor: Asst. Prof. Dr. Cüneyt Sert

July 2009, 130 Pages

Shaped charges are explosive devices with a high penetration capability and are used for both civilian and military purposes. In civilian applications shaped charge devices are used in demolition works, oil drilling and mining. In the military applications, shaped charges are used against different kinds of armors, primarily as anti-tank devices.

This thesis work involves the modeling and simulation of shaped charge devices, with the focus being on anti-tank warhead design. Both numerical simulation and analytical calculation methods are used to predict shaped charge performance; in the aspects of jet formation, breakup and penetration. The results are compared within themselves and with the data available in the literature.

AUTODYN software is used for the numerical simulations. Different solver and modeling alternatives of AUTODYN are evaluated for jet formation and penetration problems. AUTODYN's Euler solver is used to understand how the jet formation is affected by the mesh size and shape and the presence of air as the surrounding medium. Jetting option in the AUTODYN-Euler simulations are used to simulate jet formation as an alternative to simulations performed using AUTODYN's Euler solver. In the jetting option liner elements are modeled as Lagrangian shell elements, rather than Eulerian elements.

Analytical codes are written to study the jet formation, breakup and penetration processes. Many alternative formulas that can be used in the analytical calculations are listed and discussed. Parameters of these formulas are varied to investigate their effects on the results. Necessary constants for the analytical formulas are obtained using the results of AUTODYN simulations.

Keywords: Shaped charge, anti-tank warhead, jet formation, jet breakup, penetration, AUTODYN

ÖZ

ÇUKUR İMLALARIN MODELLEME VE BENZETİMİ

Gürel, Eser

Yüksek Lisans, Makina Mühendisliği Bölümü

Tez Yöneticisi: Y.Doç. Dr. Cüneyt Sert

Temmuz 2009, 130 sayfa

Çukur imlalar askeri ve sivil amaçlar için kullanılabilen yüksek delme yeteneğine sahip patlayıcılı araçlardır. Sivil kullanım alanları arasında imha ve yıkım işleri, petrol çıkarma ve madencilik bulunmaktadır. Askeri alanda ise genellikle çeşitli özellikteki zırhlara karşı kullanılmakta olup, öncelikli kullanım alanları tanksavar mermilerdir.

Bu tez çalışmasında, çukur imlaların modelleme ve sayısal benzetimi, tanksavar mermi tasarım odağında ele alınmıştır. Çukur imla başarımının; jet oluşumu, jet kopma ve delme etkinliği kapsamında incelenmesinde analitik ve sayısal yöntemler kullanılmıştır. Değişik tekniklerle elde edilen sonuçlar kendi aralarında ve literatürdeki kaynaklardan bulunan sonuçlarla karşılaştırılmıştır.

AUTODYN yazılımının farklı çözücü ve modelleme alternatifleri jet oluşumu ve delme problemlerinin çözümünde kullanılmış, AUTODYN-Euler çözücüsünde ağ sıklığı ve şekli ile çevre ortamı olarak havanın varlığının çözüme etkileri incelenmiştir. AUTODYN-Euler benzetimlerinde bulunan "Jetting" seçeneği jet oluşumunun incelenmesinde AUTODYN-Euler benzetimlerine alternative olarak kullanılmıştır. "Jetting" seçeneğinde, astar elemanları, Euler elemanlar yerine hücre "Lagrange" elamanlar ile modellenmiştir.

Jet oluşumu, jet kopması ve delme süreçlerini incelemek üzere analitik bir kod geliştirilmiştir. Açık literatürde bulunan ve analitik hesaplamalarda kullanılan formüller listelenmiş ve bu formüllerde bulunan değişkenlerin alabileceği farklı değerlerin çözüme etkileri incelenmiştir. Analitik formüllerde ihtiyaç duyulan sabitleri hesaplamak için AUTODYN benzetimlerinin sonuçları kullanılmıştır.

Anahtar kelimeler: Çukur imla, tanksavar mermi, jet oluşumu, jet kopması, delme, AUTODYN

To My Family

ACKNOWLEDGEMENTS

I would like to express my gratitude and regard to my supervisor Asst. Prof. Dr. Cüneyt SERT for his guidance and support throughout this work.

I would also like to thank to ROKETSAN Missile Industries for their software and hardware support. I am grateful to all my friends, my superiors and colleagues in ROKETSAN for their support, patience and valuable comments.

Last but never the least, I offer sincere thanks with my all love to my family, Halil İbrahim Gürel, Elif Gürel and Hasan Ersel Gürel; for their unshakable faith in me and their willingness to endure me through my whole education and life.

TABLE OF CONTENTS

LIST OF FIGURES

FIGURES

LIST OF TABLES

TABLES

NOMENCLATURE

A	Deflection angle
c	Local speed of sound at collapse point
C	Charge mass
CD	Charge diameter
D	Detonation velocity
dm	Infinitesimal liner mass
dm_j	Infinitesimal jet mass corresponding to an infinitesimal liner mass
dm_s	Infinitesimal slug mass corresponding to an infinitesimal liner mass
E_{gur}	Gurney energy
JC	Johnson-Cook constitutive model
M	Metal (casing/shell) mass
$r_c(t)$	Crater radius with respect to time
r_{cm}	Maximum crater radius
r_0	Jet radius
R_t	Target resistance term (Tate-Alekseevski penetration model)
$R_{t(R)}$	Resistance of target to radial crater growth during penetration
t	Time
t_b	Breakup time
U	Penetration velocity
U_{det}	Tangential sweep velocity of the detonation wave

U_{min}	Cutoff penetration velocity for penetration cease
V_{cl}	Collapse point velocity
V_{in}	Collapse flow velocity
V_j	Jet velocity
V_{min}	Cutoff jet velocity for penetration cease
V_0	Collapse velocity
$V_0{}'$	Differentiation of the collapse velocity with respect to the distance along the symmetry axis
V_{pl}	Experimental constant of Hirsch breakup formula (plastic velocity)
V_r	Velocity of the rearmost jet element
V_s	Slug velocity
V_{tip}	Jet tip velocity
x	Position along axis of the liner
Y	Yield strength of a liner element
Y_p	Penetrator resistance term (Tate-Alekseevski penetration model)
$z(x,t)$	Position of the liner element
$z_0(x)$	Initial jetting position of a liner element
ZA	Zerilli-Armstrong constitutive model

Greek Symbols :

β	Collapse angle
β^+	Steady state collapse angle
β_c	Critical collapse angle
γ	Angle of incidence
δ	Projection angle

ΔV	Velocity difference between jet elements
ΔX	Distance difference between jet elements
η_0	Initial strain rate
ρ_j	Jet density
ρ_{liner}	Liner material density
ρ_0	Initial explosive density
ρ_t	Target density
τ	Acceleration time constant

CHAPTER 1

INTRODUCTION

1.1 Classification of warhead types

A warhead is defined in [1] as "the specific device or part of an armament system that damages a target and renders it incapable of performing its intended function". It is possible to consider warheads in two broad categories, as defined by Carleone [1]:

a) Those use energy of the explosive that is carried within the warhead body, to accelerate metal or produce blast effect to cause desired damage. In these types of warheads, accelerated metal is either severely deformed or fragmented.

b) Those in which propellants accelerate metal penetrators to lethal velocities. In this type, generally, accelerated metal penetrator has a certain initial form, which is retained till the beginning of target interaction.

Traditionally, the former type is called warhead, or chemical energy warhead, and the latter is called kinetic energy penetrator. However, this terminology does not refer to the true mechanisms involved because the so called chemical energy warheads, except blast effect, also use kinetic energy of the accelerated metal to cause the intended damage on the target.

Conventional warheads can be divided into two categories, directed energy and omni-directional, as shown in the Figure 1-1. Directed energy warheads focus the explosive energy by the use of a cavity lined metal, most commonly an accelerated

liner. Approximately 15-20 % of the total chemical energy of the warhead explosive can be converted into the kinetic energy of the liner. Directed energy warheads can be divided further into shaped charge, hemispherical charge, and explosively formed penetrator (EFP), as shown in Figure 1-2, although there are no clear dividing lines between these types of warheads. The most extreme case of the directed energy warheads is a shaped charge, which produces metal jets with 7-10 km/s tip speeds. On the other hand EFP warheads can produce a penetrator with a velocity of 2-3 km/s. Shaped charge warheads utilize only a portion of the metal liner to form the penetrator, whereas EFP warheads utilize almost all of the liner. This thesis work focus on the performance analysis of shaped charges from jet formation, breakup and penetration points of view.

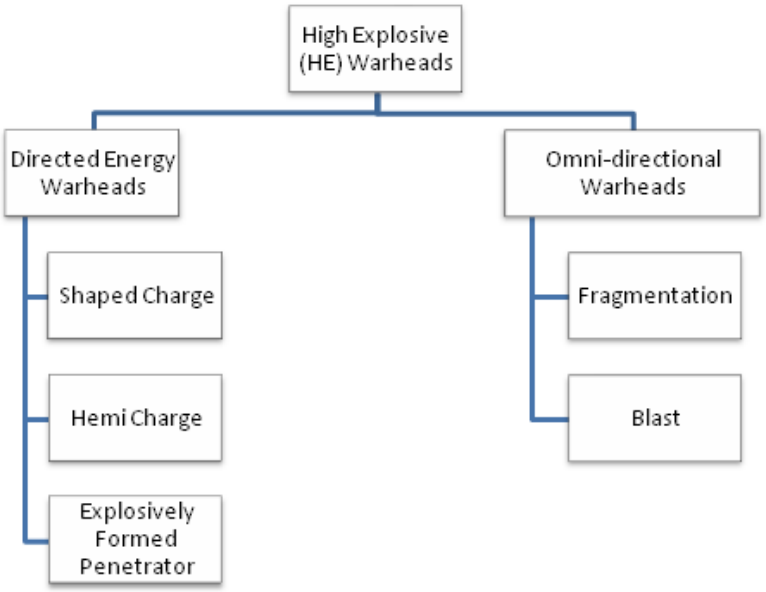

Figure 1-1 Classification of high explosive warheads [1]

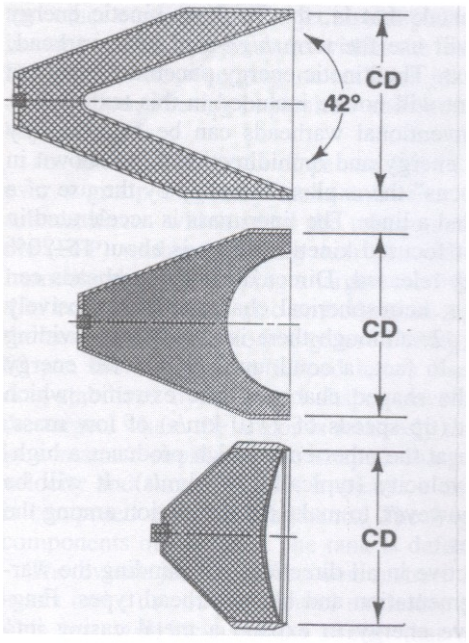

Figure 1-2 Three types of directed energy high explosive warheads; Shaped charge, hemispherical charge and explosively formed penetrator from top to down, where CD is the charge diameter [1]

Omni-directional warheads are effective in all directions surrounding the warhead [1]. Omni-directional warheads can be divided into two categories as fragmentation and blast. Fragmentation warheads accelerate large number of metal fragments. Fragment size and amount and the emerging angles can be either controlled or produced by natural fragmentation of casing due to expansion. Blast type warheads utilize the chemical energy of the warhead to produce a high pressure shock wave in the air. Blast type warheads can also have a fragmentation capability and fragmentation warheads may create a blast wave. The distinction between these categories can be determined by the inspection of primary defeat mechanism. Besides these warhead types, primary damage mechanism like fragmentation and blast can be combined to design a multipurpose warhead.

1.2 Introduction to Shaped Charges

Walters [2] defines a shaped charge as “a cylinder of explosive with a hollow cavity at the end opposite of the initiation train”. A cross-sectional view of the standard BRL-82 charge that is studied in this thesis is shown in Figure 1-3 [3]. If the cavity does not contain a liner, it is referred as a hollow charge or an unlined-cavity charge. If it contains a liner made from metal, alloy, glass, ceramic, wood or another material, the device is called a shaped charge or cumulative charge (in the former Soviet Union) or Hohlladung (in Germany) [2]. Generally used liner geometries are conical, hemispherical, parabolic or any acute shape. For the EFP charges, generally bow shaped liners are used. Those charges also referred to “as the self-forging fragment, ballistic disc, P-charge projectile and Miznay - Schardin device. In shaped charge warheads, generally narrow angled cone-like geometries are used. Optimized liner geometries may have double or variable angled cones, tulip or trumpet shapes. Of course, there is no clear distinction between shaped and EFP charges; since a wide angled and thick walled shaped charge liner may form a penetrator similar to EFP. The term “hollow charge” was apparently coined by A. Marshall in 1920 and the terms “shaped charge” was coined in the U.S during World War II [2]. In Table 1-1, a brief history of the shaped charges is given.

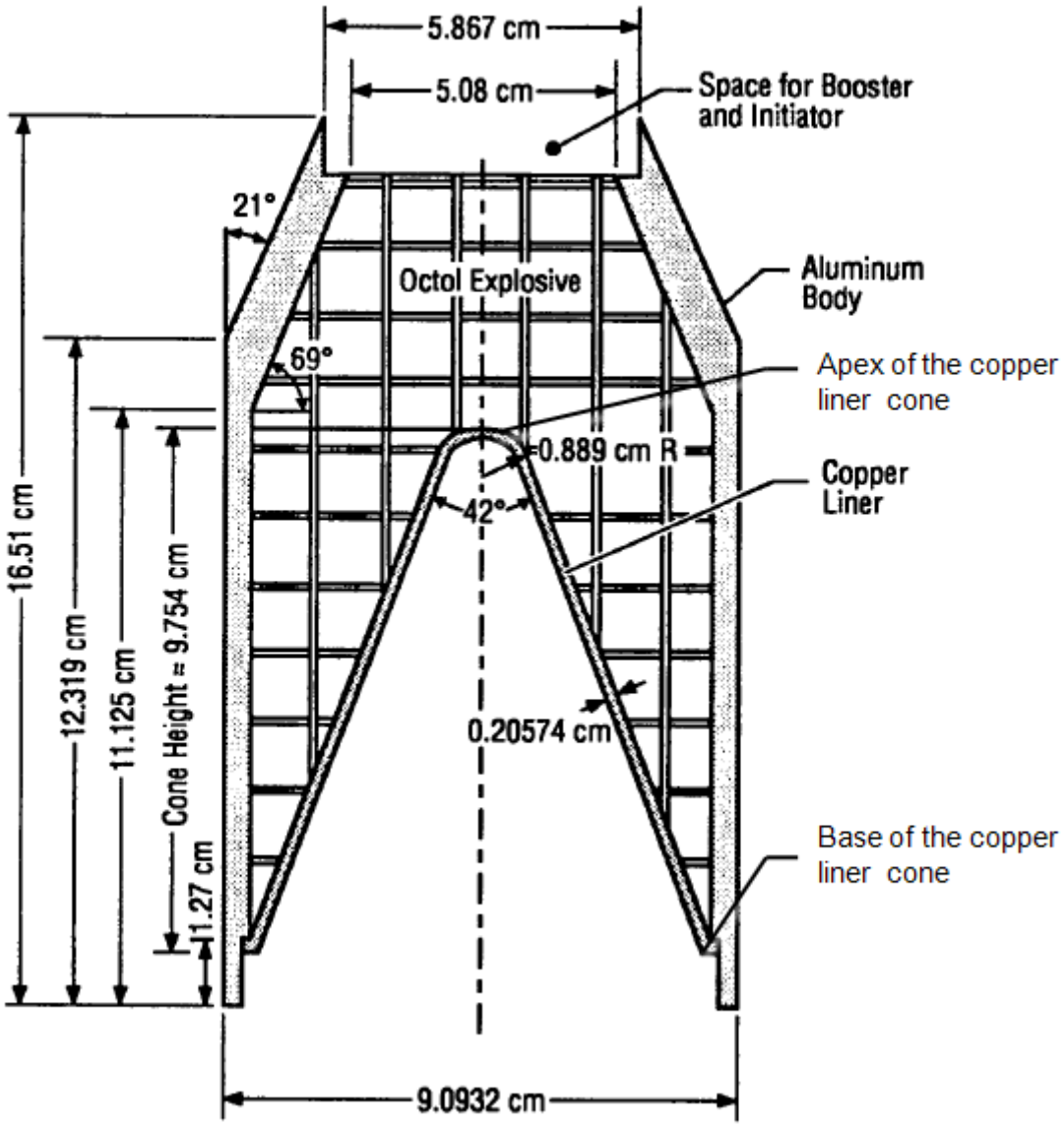

Figure 1-3 Section view of the BRL-82 charge showing shaped charge elements [3]

Table 1-1 Brief history of the shaped charge [2]

Date	**Scientist or Country**	**Invention/Contribution**
1792	Franz von Bader	Focused the energy of an explosive blast using a hollow charge. However, his experiments utilized black powder which can not detonate.
1867	Alfred Nobel	Invented detonator.
1883	Von Foerster	Demonstrated the hollow cavity effect.
1888	Charles Munroe	Conducted experiments with explosive charges having cavities in contact with a steel plate. He is famous with his explosive engraving experiment, in which initials of USN (United States Navy) are engraved a steel target.
1911	E. Neumann	Demonstrated the unlined cavity effect by showing that an explosive with cavity can generate a greater penetration than a solid cylinder block of explosive.
1940	U.K.	No.68 shaped charge rifle grenade was put into British Service.
1941	U.S.	U.S. produced 2.36 in. high explosive anti-tank (HEAT) machine gun grenade and the 75- and 105-mm HEAT artillery projectiles. Later, the machine gun grenade was modified to include a rocket motor and shoulder launcher and became the bazooka. Bazooka was first used in North Africa.

Table 1-1 Brief history of the shaped charges [2] (continued)

1941	Germany	A hemispherical hollow cavity charge, with and without iron liner is tested against ship armor steel at different distances to target. Penetration of 0.4 CD (charge diameter) is achieved for unlined cavity at zero target distance. For the lined cavity, penetration was 0.7 CD at zero target distance and 1.2 CD for target distances between 0.5 CD and 1.5 CD.
WW-II	Germany	Flash X-ray is used to investigate liner collapse and jet formation processes. Various liner geometries were studied including conical, hemispherical and ellipsoidal liners. The effects of varying the cone angle, wall thickness and standoff distance were studied. It was concluded that 60/40 Cyclotol (a RDX-TNT mixture) is the optimum explosive fill for shaped charges
WW-II	Germany	A 65-cm-diameter shaped charge called SHL 500 was used against light ships. The largest of SHL series called Beethoven, had a diameter of 180 cm with 500 kg of explosive
WW-II	Japan	Japanese developed SAKURA I and II bombs for kamikaze plane attacks.

The theory behind the shaped charge is continued to develop during the 1950s, boosted by the Korean War. Starting from 1950s significant developments in the shaped charge technology were made by the perfection of experimental techniques such as high speed photography and flash radiography. Other advances emerged from the development of computer codes to simulate the collapse, formation and growth of the jet form a shaped charge liner. These codes provide excellent simulations of the formation of the jet.

1.2.1 Shaped Charge Principles

The most common shaped charge consists of a detonator-booster explosive train for initiation of a right circular cylinder of explosive which upon detonation collapses a metallic lined cavity at the opposite end of the detonator. In Figure 1-3 components and geometric details of the BRL-82 charge are given. Schematics of the explosive detonation, liner collapse and resulting jet formation processes are shown in Figure 1-4.

Upon initiation of the explosive, a spherical detonation wave propagates outward from the point of initiation. This high pressure shock wave propagates at the detonation velocity of the explosive (typically greater than 8 km/s) and at a pressure equal to the Chapman-Jouget pressure (P_{cj} > 0.25 Mbar). As the detonation wave impinges upon the lined conical cavity the material is accelerated inward collapsing the cone on the axis of symmetry. The collapse of the liner material on the centerline forces a portion of the liner to squirt out in the form of a jet with velocities as high as 12 km/s [4]. The final frame of Figure 1-4 shows a fully formed jet.

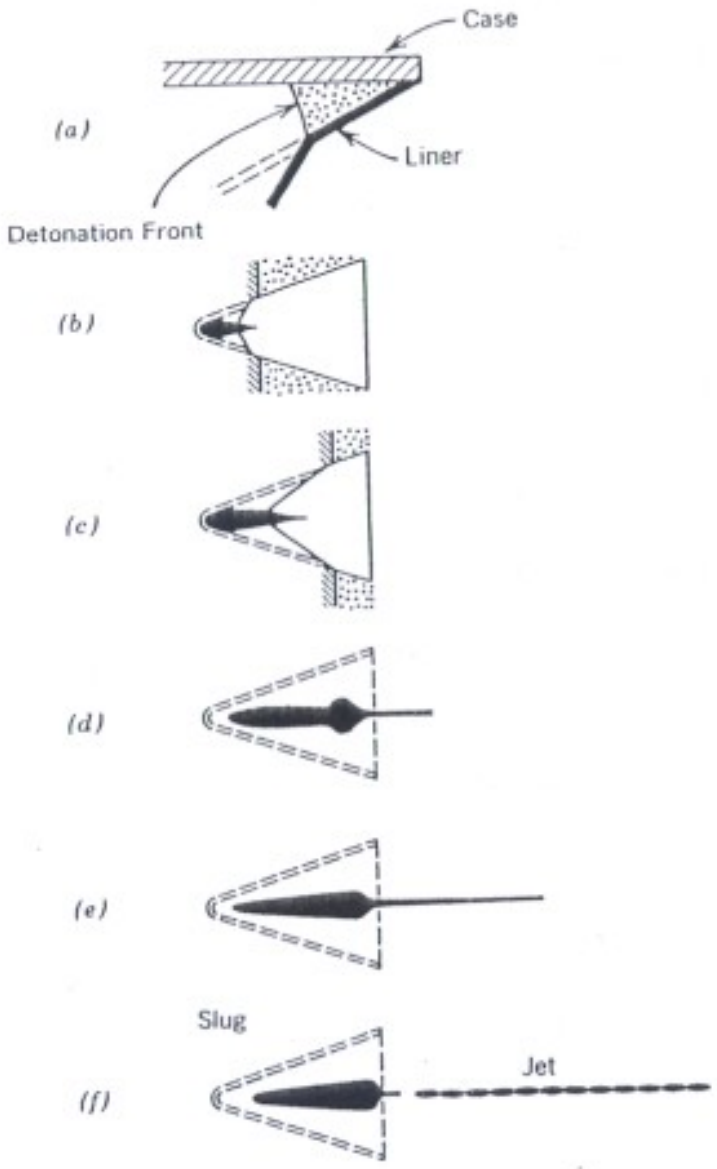

Figure 1-4 Schematic description of explosive detonation, liner collapse and jet formation showing liner as bold black lines [5]

Because of the extreme directionality of the energy residing in the jet, it is possible to deliver it to a specific location on a target. The pressure generated in the region of impact has been shown to be so great that the strength of the jet and target material could be ignored, and therefore, these materials could be treated as perfect fluids. In 1948, Birkhoff, MacDoughall, Pugh and Taylor showed that as the high velocity jet impinges upon the target material it produced pressures close to a million atmospheres which forces the target material to flow plastically out of the path of the jet [6]. A description of this phenomenon in the form of a piecewise penetration process is shown in Figure 1-5.

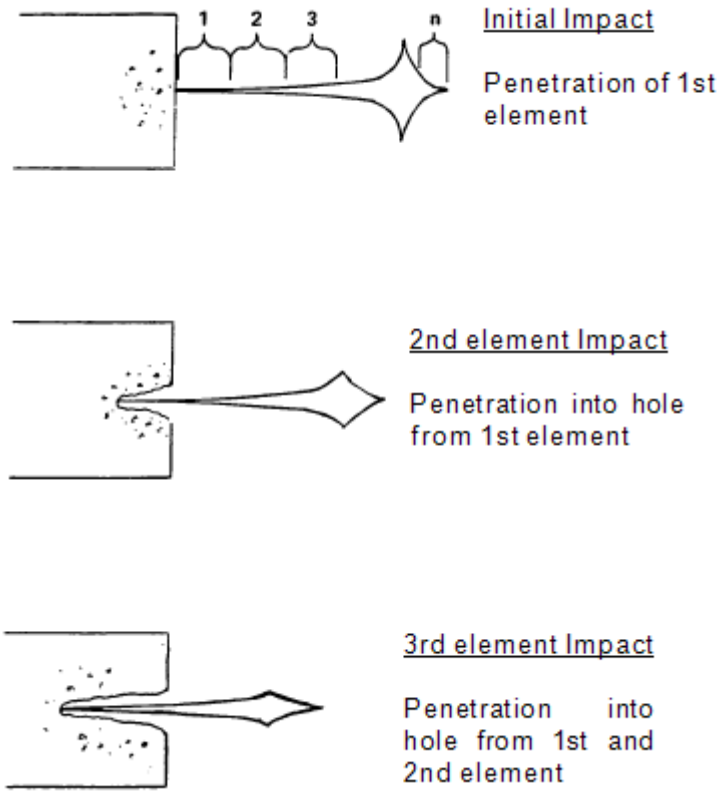

Figure 1-5 Schematic description of jet penetration process [4]

In Figure 1-5 we assume that the jet is divided into n elements each penetrating the target in a sequential manner. At initial impact, the first element penetrates the target, creating a hole. The second element impacts the target at the bottom of the hole created by the first element. Penetration continues until the jet is totally consumed while doing work on the target in creating the hole.

The overall process, from explosive detonation to total target penetration, occurs in under half of a millisecond, for short target distances. Due to the extremely high pressures, short time durations, and the harsh environment that exist in the jet/target interaction region, this is an exceedingly complex phenomenon to describe analytically and diagnose experimentally [4]. As early as mid 1940's, however, experimentalists have shown that penetration performance trends exist when certain shaped charge and target parameters are varied. Similarly, analysts have developed methods to predict the trends with the overall objective of maximizing depth of penetration in metallic targets. Generally, analytical methods predict either the configuration of the jet without considering the target penetration process, or predict the target penetration assuming some prior knowledge of the jet configuration.

1.3 Review of Anti-tank Missiles

Armor and anti-armor have been playing a cat-and-mouse game ever since they were invented. Today, the warhead seems to have a great advantage because of the weight penalty it imposes on armored vehicles as modern warheads can achieve armor penetration greater than 1000 mm RHA (Rolled Homogeneous Armor) equivalent [7]. Besides, modern anti-tank missiles have advanced maneuvering capabilities so that they can hit less protected areas of the tanks. An example is "top-attack" mode of some missiles, in which the missile tracks a climbing trajectory followed by a sudden dive aiming turret top as one of the less protected area on the tank. Another example is "over-fly top attack" mode, in which the missile flies over the tank and activates warhead(s) at the instant it is above the turret top.

In Table 1-2 a brief survey of common anti-tank missiles, with the emphasis being on tandem warhead, is given. Different types of warheads can be used in tandem configuration, but here the phrase "tandem warhead" is used for tandem shaped charge warheads. In the tandem configuration there are actually two warheads; first one is to defeat ERA and the second one is for main armor of the target. The first one is smaller in size and placed in the front region of the missile. The second one is the main warhead and generally placed at the optimum standoff in the missile.

Table 1-2 Brief survey of common anti-tank missiles [7]

Missile	**Producer**	**Missile Weight (kg)**	**Length & Diameter (mm)**	**Range (km)**	**Penetration Performance (mm - RHA)**
Hellfire -II (AGM-114K)	Lockheed Martin	45.7	1626 178	8	900
Brimstone	MBDA	50	1800 178	8	900
Mokopa	Kentron	49.8	1995 178	10	1300
Ingwe	Kentron	45	1750 127	5	1000
Vikhr (9M121)	KBP	45	2450 130	10	-
Ataka-V (9M120)	KBM	49.5	1830 130	6	-
TOW-2B (BGM71F)	Raytheon	22.6	1168 147	3.75	-
HOT	MBDA	24	1270 150	4	1300
TRIGAT-LR	MBDA	48	1620 145	7	-
Spike-ER	Rafael	33	1670 170	8	750

1.4 Review of Armor

Armor has a broad range of applications; such as personal protection (body armor), vehicle protection and building protection. Vehicle applications of armor include both civilian and military armored vehicles. In this part of the text, light armored vehicle and main battle tank armor applications are briefly discussed since the primary point of interest of the current work is on anti-armor warhead applications.

As anti-tank weapons aim to focus high energy and momentum over the smallest possible area to achieve high penetration performance, armors are designed to dissipate energy over a large volume and spread the load to reduce local pressure [8]. Increasing penetration performance of the anti-tank missiles cause the necessity of transferring the armor mass to more vulnerable sections of the tank, due to the weight requirements. Generally turret front of a tank is the most protected region. When a threat is recognized, the tank turns its main gun to the threat for counter attack, facing its most protected area. Turret side and rear, skirts and turret top are lesser protected areas.

In Table 1-3 density and hardness values of different armor materials are given. Among the armor materials used in modern tanks, steel is the most common one and it accounts for half of the weight of the tank. Although there exist many different types of steel, only few of them have a practical value in terms of being used as armor material. In order to survive the pressure and strain of the impact, steel must be strong and ductile. The class of High Strength Low Alloy steel (HSLA) is one of the commonly used armor steel type. An example of this type is 4340 steel having a ductility of 8-1 0% with an ultimate tensile strength of 1.0-1.1 GPa [5].

Table 1-3 Density and hardness values of different armor materials [9]

Material	**Density (kg/m^3)**	**Vickers Hardness**
RHA	7850	240-380
Dual Hard Steel, Face	7850	600-750
7039 Aluminum	2780	150
Aluminum oxide 85 %	3450	900-970
Aluminum oxide 99 %	3900	1500-1700
Silicon carbide	3150	2200-2500
Titanium diboride	4250	2500-2700
Boron carbide	2450	3000

Rolled Homogeneous Armor (RHA) is one of the most commonly used armor material. RHA is also used as a reference material for the penetration resistance performance of other armor materials and configurations. High hardness steel (HSS) is a version of RHA, which has about 500-600 BHN hardness. HSS is difficult to weld and can only be manufactured in thin plates.

Aluminum is an attractive alternative to steel, since its density is nearly one thirds that of steel. It is lighter with a density of 2.66 g/cm^3 and has high corrosion resistance. Aluminum is generally employed in skirt armors of the modern main battle tanks.

Titanium is another alternative with a density of 4.5 g/cm^3 and a penetration resistance of 80-90 % of RHA [5]. However its price is many times that of Aluminum which itself is already twice as expensive as RHA. Titanium can still be used in modern main battle tanks to reduce weight.

Many different composite materials have also been tested for armor systems. Composites generally consist of a high strength fiber material suspended in a matrix for stiffening and reinforcement purposes. Common matrix materials are types of epoxy, thermoplastics, vinlyester, polyester and phenolic. Strength of the composite materials is primarily based on the strength of the fibers. Composites are soft

materials and their resistance to shaped charge penetration is low. They are generally used to reinforce other materials, like ceramics, in armor configurations.

Ceramics are low density materials with high bulk and shear modulus which are two of the main requirements of an armor system to reduce weight and prevent large deformations. Also they have high yield strength to prevent failure. Another requirement for an armor material is to have high dynamic tensile strength to avoid material rupture when tensile waves appear [8]. Ceramics are vulnerable to tensile waves generated by compressive waves reflected from the free surfaces since they are brittle. This makes ceramic armors vulnerable in multi-hit scenarios and suffer from sustaining post-hit structural integrity. For these reasons, ceramics are generally supported by a ductile backing layer, enhancing both tensile fracture behavior and post-hit structural integrity. Aluminum and composites are effective examples of backing materials.

One of the first methods to enhance armor of tanks is the spaced plate arrangement. It is known that if the armor plates are arranged with air gaps within, the total effectiveness of the plates are greater than in-touch arrangement. One of the reasons of this effect is that shaped charge jets have an optimum effective standoff distance, over which penetration decreases. Also, in a spaced arrangement, it is possible for jet particles to divert from the axis of flight. If the spaced plate arrangement is layered with different materials, the effectiveness of the armor can be increased further.

Explosive Reactive Armor (ERA) is a special type of armor, in which a layer of explosive is placed between two metallic plates in a sandwich arrangement. When ERA is struck with a shaped charge jet (or kinetic energy penetrator), the explosive layer of ERA is detonated with the pressure developed at the penetration interface. Detonating explosive layer accelerates two plates of ERA in opposite directions. As the plates are moving, they intersect the route of the shaped charge jet by a line on the plates, so that the jet does not punch a hole but rather creates a slot on the plates. By this way effective thickness of the plates is increased. ERA can be employed as an add-on armor, mounted on the main armor of the vehicles in a box arrangement. In each ERA box a single layer of sandwich may be employed or multiple (generally

double) layers can be used. Also ERA can be developed as an integrated part of the armor system.

Non-explosive reactive armor (NERA) is a version of ERA, in which an elastic material is used instead of the explosive layer between metallic plates. As the penetrator struck the plates, elastic material bulges with the effect of internal pressure developed, and accelerates metallic plates. The same defeat mechanism as ERA is employed afterwards. The effectiveness of NERA is less compared to ERA.

1.5 Literature Survey

It is known that there are numerous studies performed on shaped charge devices and armor systems in Middle East Technical University BİLTİR SAV-SİS center. To the best knowledge of this author there exits one master's thesis and one doctorate dissertation available in open sources, performed at Turkish universities.

First one is "Formation and Penetration of the Shaped Charge Jets" written by Özel [10]. In this study, main parameters, including the material properties, of a shaped charge affecting the jet formation are examined from the penetration point of view. A computer program is developed for the analytical calculation of jet formation and resulting penetration. Densities ranging from 1 g/cm^3 to 13 g/cm^3 for the casing and liner materials are considered. Six different explosive materials are taken into account. The effect of material properties on the jet velocity and penetration and the effect of two limiting conditions for the propagation of detonation wave on penetration are investigated.

The second study is a doctorate dissertation by Aksoy titled as "Investigation of Liner Collapse in the Shaped Charge Technology" [11]. In this work numerical simulation of BRL-82 charge is performed by DYNA2D software. In the simulations liner thickness, explosive type and initiation point are varied and their effect on the performance of the charge is investigated.

There are numerous foreign studies present on shaped charge jet formation, breakup and penetration. In the following paragraphs, foreign studies that are used in the current study will be mentioned.

Birkhoff, MacDougal, Pugh and Taylor were one of the first to state that explosives produce more penetration when there is a cavity in the explosive [6]. In their famous paper "Exposives with Lined Cavities, they reviewed shaped charge history and tactical military applications of shaped charge warheads. Also they discussed the jet formation and penetration for constant and variable velocity penetrators.

Walters presents a brief history of the shaped charge [2]. Carleone discussed the physics of the warhead, warhead-target interaction and tactical use [1]. Walters and Zukas discussed the formation, breakup and penetration of shaped charge jets together with the common properties and production methods [5].

In the PhD thesis of Baker, liner collapse and formation are investigated with the focus being on wave shaper design. Wave shaper is an inert material placed in explosive to change the propagation direction of detonation wave. The calculations are performed by CALE analytical code. An optimization procedure is applied to find the optimum wave shaper geometry and position [12].

Chou and Flis discussed recently used jet formation, breakup and penetration formulas in their paper [13]. Bolstad, and Mandell worked on numerical simulations of shaped charge jet formation and penetration using MESA-2D and MESA-3D numerical codes [3]. Chanteret also discussed recently used analytical jet formation, breakup and penetration formulas and suggest a different method for the calculation of collapse angle [14]

Walters and Summers made a review for the breakup models in their paper and gave breakup measurements for BRL-82 charge [15]. Pappu performed numerical simulations for explosively formed penetrators. In his work microstructure of the soft recovered EFP's are investigated. They discussed the affects of strain, strain rate and temperature on the final microstructure [16].

Rosenberg and Dekel performed penetration velocity measurements of long rods in different target materials to calculate materials' resistance terms that are used in the penetration formulas. They compared their results with the numerical simulations performed by PISCES and AUTODYN software [17]. In their further work, a calculation method for the material the resistance is suggested [18].

Hancock gave penetration data for BRL-82 charge for different standoff distances [19]. Also, variation of penetration cutoff velocity is given with respect to the standoff distance. In his Ph.D. work Murphy investigated the shaped charge penetration in concrete with penetration velocity experiments. Penetration velocity is measured with break switches placed in the concrete target. Experimental results are compared with the analytical penetration calculations [4].

Held discussed the radial crater growth process in his paper. He gave formulas for crater radius as a function of time and for maximum crater radius. He also discussed resistance of target to radial crater growth. He compared his results with experimental data of flash X-ray measurements [20].

1.6 Outline of the Current Work

In the current thesis work, different methods of modeling and simulating shaped charge warhead performance in the aspects of jet formation, breakup and penetration are discussed.

In the current study, numerical simulation and analytical calculation methods are used alone and successively for the prediction of shaped charge performance. Rather than shaped charge parameters, parameters that are affecting numerical simulation and analytical calculations are investigated. Jet breakup is discussed in detail, as an addition to other available Turkish studies. Also a method for combining numerical jet formation and analytical penetration calculations is suggested, for calculating both penetration depth and crater radius. AUTODYN software is used for numerical

simulation of jet formation and penetration. Formulas that are used in the analytical calculation of shaped charge jet performance are given and investigated. Constants for the analytical formulas are calculated by numerical simulations when necessary. The results of both analytical calculation and numerical simulations are compared with the available data in the references.

In Chapter 2, analytical formulas and numerical methods that are used in the jet formation, breakup and penetration calculations are given.

In Chapter 3, numerical simulations and analytical calculations for the jet formation process are discussed. Different solvers and modeling methods of AUTODYN software is used for jet formation and penetration problems. Effect of mesh size and shape and presence of air on numerical jet formation simulations using AUTODYN-Euler solver are investigated Jetting option in the AUTODYN-Euler simulations are used as a comparison and as an input for some of the analytical calculations.

In Chapter 4, breakup of shaped charge jets is analyzed. Five different breakup calculation methods are discussed; using jet data from the numerical simulations and analytical calculations as an input. The results are compared with the available data in Walters and Summers [15].

In Chapter 5, penetration of the shaped charge jets is discussed in the aspects of penetration depth and crater formation. Numerical simulation and analytical calculation results for the penetration depth and crater radius are compared. Also a method for combining numerical jet formation and analytical penetration calculations is discussed, for calculating both penetration depth and crater radius.

Finally in Chapter 6, results obtained in the previous chapters are summarized and discussed. Shortcomings of the current work and possible future studies are listed.

CHAPTER 2

MODELING OF SHAPED CHARGE

This chapter is mainly about formulas that can be used in the analytical performance calculations of shaped charges. Most of the formulas listed here will directly be used in the upcoming analytical analyses. In addition, last section of the chapter discusses numerical methods that can be used in shaped charge analysis.

The term shaped charge is used to designate devices that induce severe liner jetting. The idealized phenomena of shaped charge liner collapse and jet formation is described by the separate processes of explosive detonation, liner collapse, collapse point jetting and jet stretching. Referring to Figure 2-1, an idealized technical description of these processes is given by Baker as follows [12],

1-) The first stage of functioning of a shaped charge is explosive detonation. The Explosive is detonated at the back end of the shaped charge device. Explosive detonation front propagates through the explosive with a velocity D. The detonation sweeps across the liner surface with a tangential sweep velocity U_{det} which is greater than D due to the angle of incidence γ.

2-) As the detonation wave propagates through the explosive, it interacts with the liner mounted in the explosive. In the second stage of the process, high pressures generated by the explosive accelerate successive liner elements towards the axis with collapse velocity V_0 and projection angle δ . The velocity vector of the element changes both in magnitude and direction during the acceleration.

3-) Liner elements, which are collapsing radially, meet at the symmetry axis and form a jetting region. Center of this region on the axis is known as the collapse point. Collapse point moves along the axis at a velocity V_c that changes during the entire jet formation process. Collapsing liner elements enter the jetting region at a collapse angle β. Mass of the liner elements are separated into two parts, each moving in opposite directions along the axis away from the collapse point. The mass element moving forward with a velocity of V_j is known as the jet. Mass moving backwards with a velocity of V_s is known as the slug. Slug may even have negative velocity with respect to a stationary coordinate system in particular designs.

4-) Because of the changing collapse velocities and angles both the jet velocity V_j and slug velocity V_s are changing during the entire process. In the case of the jet, a positive velocity gradient causes jet stretching and a negative gradient causes mass accumulation. Negative velocity gradient is often called as inverse velocity gradient. Mass accumulation typically occurs at the tip of the shaped charge jets, and the rest of the jet stretches at a high rate. The jet will stretch to several times of its original length and eventually breakup into small particles. Breakup of the jet may cause the jet particles to divert form the axis of flight, which may result in the decrease of total penetration.

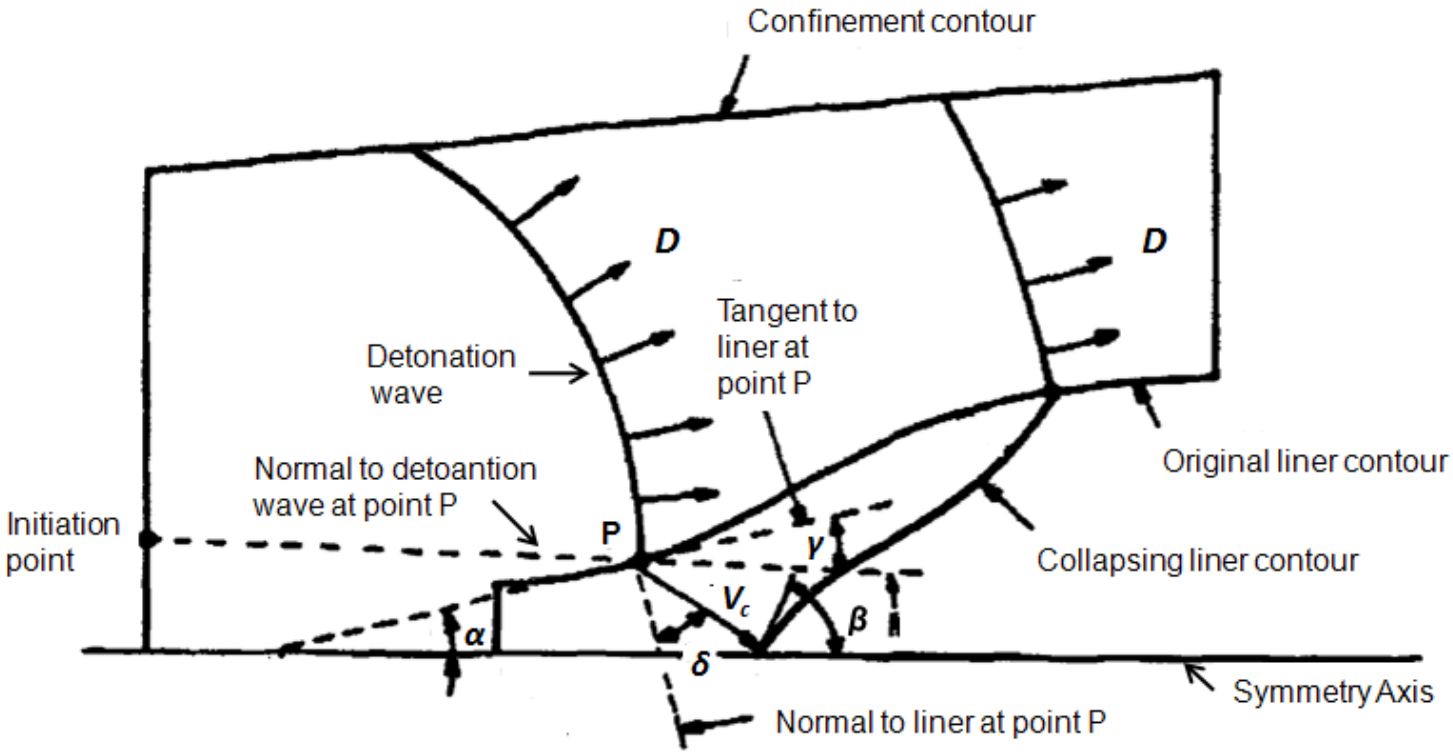

Figure 2-1 Charge geometry and collapse [10]

2.1 Analytical Modeling of Shaped Charges

2.1.1 Shaped Charge Modeling

The terms “analytical” or “one-dimensional” shaped charge jet formation model are used to specify a complete mathematical shaped charge model that defines formation processes of the jet. An analytical shaped charge model is divided into separate models describing explosive detonation behavior, liner velocity and acceleration, liner angular projection, collapse point jetting, sonic criterion, jet tip formation and jet stretching. A solution is achieved by treating the liner as a collection of discrete mass elements, each having the same thickness of the liner. Equations are applied on each individual liner element to predict the final jet characteristics.

2.1.2 Explosive Detonation Behavior

Classical detonation theory provides a stable, constant detonation velocity solution for a jump discontinuity from the unreacted explosive to completely reacted detonation products [12]. The theory assumes that the detonation products are in thermodynamic equilibrium described by a thermodynamic equation of state. The solution is known as Chapman-Jouget detonation, after the first two scientists to propose a solution. Chapman and Jouget independently hypothesized that the flow at the fully reacted state, just behind the detonation front, is sonic with respect to the detonation velocity. Experiments verify that, on a macroscopic level, Chapman-Jouget detonation is often rapidly approached after explosive initiation. The constant Chapman-Jouget detonation velocity, D, is either obtained through experimentation or calculated using a thermodynamic equation of state. When a constant Chapman-Jouget detonation velocity is assumed, both the time t_0 that the detonation reaches a

liner element and the liner sweep velocity of each element $U_{det} = D/\sin(\gamma)$ can easily be calculated using the location of the initiation point and the liner geometry.

2.1.3 Liner Collapse and Acceleration

In the simplest treatment of liner explosive interaction, the liner acceleration is ignored and the liner collapse velocity is assumed to be constant. By assuming a final linear distribution of radial gas velocity, constant radial density distribution, and no axial effects, Gurney derived a formula for the terminal collapse velocity V_0 for exploding cylindrical or spherical shells. This formula can be expressed in the following general form

$$V_0 = \sqrt{2E_{gur}}f(\mu) = \sqrt{2E_{gur}}\left[\frac{C}{M} + \frac{n}{n+2}\right]^{\frac{1}{2}} \tag{2.1}$$

where C is the explosive mass behind the element, M is the liner mass, μ is the liner to explosive mass ratio and n is the spatial geometry constant which is 0 for planar, 1 for cylindrical and 2 for spherical geometries. The value of the Gurney energy E_{gur} is an explosive property and it represents the explosive's available specific kinetic energy (about 70 % of the heat of detonation). The term $\sqrt{2E}$ is known as the Gurney velocity constant and its value for different kinds of explosives are available in many references.

Other formulas used in the literature for liner collapse velocity are given below, where D is the detonation velocity.

Trinks [21] :

$$V_0 = 0.36D \tan^{-1}\left(\frac{2}{3\mu}\right) \tag{2.2}$$

Chou-Flis [13] :

$$V_0 = \sqrt{2E}\left[\frac{1}{4\mu^2 + 5\mu + 1}\right]^{1/2} \tag{2.3}$$

Duvall [22] :

$$V_0 = D\left[1 + \frac{27\mu}{16}\left(1 - \sqrt{1 + \frac{32}{27\mu}}\right)\right] \tag{2.4}$$

Mikhailov and Dremin [23] :

$$V_0 = \frac{0.602D}{1 + 2\mu} \tag{2.5}$$

Shushko [24] :

$$V_0 = 0.61D\left[\frac{18\mu^2 + 12\mu + 1 - 6\mu\sqrt{9\mu^2 + 12\mu + 2}}{1 + 6\mu}\right] \tag{2.6}$$

These terminal collapse velocity formulas do not explicitly treat liner acceleration. More often, empirical relationships for the liner acceleration are incorporated with a final velocity model. The most commonly used acceleration formula, proposed by Randers-Pehrson is the following exponential formula [25],

$$V(t) = V_0 \left[1 - exp\left(-\frac{t - t_0}{\tau}\right)\right] \tag{2.7}$$

Based on initial momentum considerations, Chou suggests the following form for the time constant τ [13]

$$\tau = C_1 \frac{MV_0}{P_{cj}} + C_2 \tag{2.8}$$

where P_{cj} is the Chapman Jouget pressure of explosive. Constants C_1 and C_2 are explosive parameters that can be determined empirically from experiments and finite element calculations.

2.1.4 Liner Projection

During the liner collapse process, liner element velocity vector makes an angle of δ with the normal of the original liner surface (see Figure 2-2). Line PJ designates the path along which liner element collapse to the axis. Taylor developed a formula relating the projection angle δ to liner collapse and sweep velocities [26]

$$\sin \delta = \frac{V_0}{2U_{det}} \tag{2.9}$$

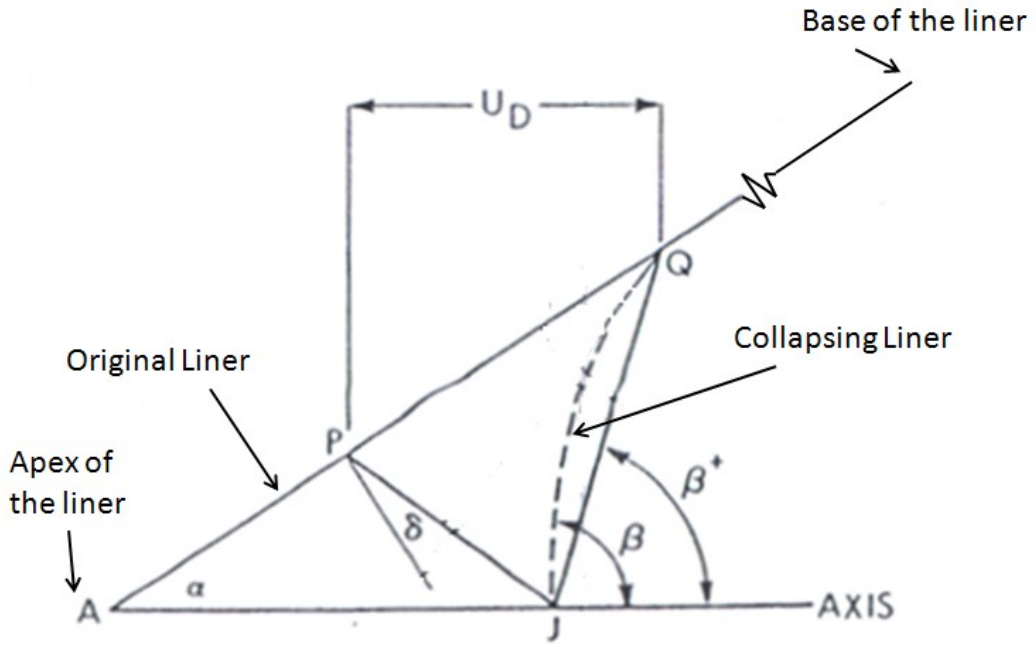

Figure 2-2 Collapse process for variable collapse velocity [5]

In deriving this formula the collapse process is assumed to be steady-state with respect to a coordinate system moving with the sweep velocity U_{det}.

As the liner is accelerated with an angle with respect to the normal of the liner surface, it begins to collapse towards the axis of the cone. The collapse angle, which is the angle at which liners elements reach the jetting region, is necessary to study the jetting process. If a constant and unique acceleration is assumed for all collapsing liner elements successive collapsing liner elements will be on the line JQ (see Figure 2-2). For such a case the collapse surface remains conical since all liner elements will move the same amount during the same time period. In such a case, the collapse process can be assumed to be a steady state process and "steady-state" collapse angle β^+ can be calculated by the following equation as a first approximation.

$$\beta^{+} = \alpha + 2\delta \tag{2.10}$$

However, the collapse velocity decreases from apex to base, and a collapsing surface with a non-conical contour, as shown with the dashed line in Figure 2-2, occurs. In this case the collapse angle can no longer be calculated by Equation 2.10. Corrected collapse angle β can be calculated by Equation 2.11, considering the effect of changing collapse velocity by using the derivative of the collapse angle with respect to cone height, which is denoted by V_0'.

$$\tan\beta = \frac{\sin\beta^{+} - \mathrm{X}\sin\alpha(1 - \tan\mathrm{A}\tan\delta)\frac{\mathrm{V_0'}}{\mathrm{V_0}}}{\cos\beta^{+} + \mathrm{X}\sin\alpha(\tan\mathrm{A} + \tan\delta)\frac{\mathrm{V_0'}}{\mathrm{V_0}}} \tag{2.11}$$

$$\text{where} \quad A = \frac{\beta^{+} + \alpha}{2}$$

Note that the deflection angle, A, is defined as the angle that a liner element moves toward the axis, given by,

$$A = \alpha + \delta \tag{2.12}$$

2.1.5 Collapse Point Jetting

Birkhoff, MacDougall, Pugh and Taylor [6] published the first theory of shaped charge formation. Due to very high pressures during the jetting process, they neglected the liner strength and treated the liner as an inviscid fluid. Furthermore they treated the jet formation as a steady incompressible hydrodynamic event,

producing a constant velocity jet [12]. By applying the steady incompressible irrotational Bernoulli equation and momentum conservation in the axial direction to a constant angle liner, they derived the following formulation,

$$V_{cl} = \frac{V_0 \cos\left(\frac{\beta - \alpha}{2}\right)}{\sin\beta} \tag{2.13)a}$$

$$V_{in} = \frac{V_0 \cos\left(\frac{\beta + \alpha}{2}\right)}{\sin\beta} \tag{2.13)b}$$

$$V_j = V_{in} + V_{cl} \tag{2.14)a}$$

$$V_s = V_{in} - V_{cl} \tag{2.14)b}$$

$$m_j = \frac{m}{2}(1 - \cos\beta) \tag{2.15)a}$$

$$m_s = \frac{m}{2}(1 - \sin\beta) \tag{2.15)b}$$

where V_{in} is the flow velocity, V_{cl} is the stagnation point velocity, m_j is the jet mass, and m_s is the slug mass (see Figure 2-3). If a coordinate is selected to move with stagnation point J of Figure 2-2, flow velocity is the velocity of the liner element collapsing towards point J. Stagnation point velocity is the velocity of the stagnation point along the *x*-axis. Birkhoff et.al. noted that although experimental observation agreed qualitatively with many aspects of their theory, constant velocity jets were not observed. In fact, most of the shaped charges produce a large jet velocity gradient, causing the jet to stretch and eventually break up.

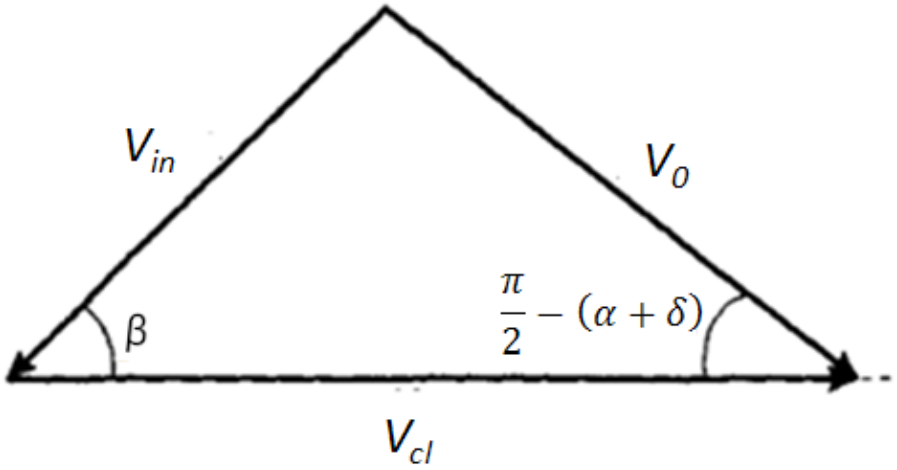

Figure 2-3 Geometrical relation between the collapse velocity, flow velocity and stagnation velocity [14]

Pugh, Eichelberger and Rosteker modified the steady state theory in order to account for the jet velocity gradient [27]. The resulting theory, known as the P-E-R theory, is based on the same assumptions as the steady state theory. The difference is that the final collapse velocities of liner elements are not the same, but depend on the original positions of the elements. Thus, the projection angle δ and the collapse angle β are no longer constants. In P-E-R formulation, jet and slug velocities are given as

$$V_j = \frac{V_0 \cos\left(\alpha + \delta - \frac{\beta}{2}\right)}{\sin\frac{\beta}{2}} \tag{2.16a}$$

$$V_s = \frac{V_0 \cos\left(\alpha + \delta - \frac{\beta}{2}\right)}{\cos\frac{\beta}{2}} \tag{2.16b}$$

As a general behavior collapse velocity V_0 and projection angle δ decrease, whereas the collapse angle β increases, from apex to base. As a result, the jet velocity is normally predicted to decrease from tip to tail, causing jet elongation. The P-E-R theory serves as the basis for almost all currently used analytical shaped charge models [12].

2.1.6 Jet Tip Formation

Generally, the induced liner collapse velocity decreases from liner apex to liner base, causing a positive jet velocity gradient and consequent jet stretching. The reason is that, as one moves from apex to base, charge to liner mass ratio decreases because of the cone shaped liner of a conventional shaped charge. However, near the apex, liner elements are not at sufficient distances from the axis to accelerate considerably. Consequently, there often exists a region near the liner apex that produces a negative velocity gradient on the jet. The negative jet velocity gradient causes jet mass to accumulate at the jet tip, which is known as the jet tip formation process. For purely conical charges, the first 30- 40% of the liner, from the apex, forms the jet tip which has a much larger radius than the rest of the jet. Modified jet tip velocity V_{tip} should be calculated by summing the shaped charge jet divided by the summed mass

$$V_{tip} = \frac{\int_o^{m_{\text{tip}}} V_j dm_j}{\int_o^{m_{tip}} dm_j} \tag{2.17}$$

Similarly, radius of the jet can be calculated by the mass weighted average of the radius of the jet elements. A more accurate prediction of the jet radius can be made calculation of velocity (so the strain) of the jet tip elements depending on time.

2.1.7 Jet Stretching Behavior

Since velocity of the jet is decreasing from tip to tail, the jet elongates during its flight. To study the jet stretching behavior, strength of the jet is neglected and strain is based on the velocity and mass distribution along the jet elements. The position z of each Lagrangian jet element is expressed in terms of the initial element jetting position z_0 , the current time t, the initial element jetting time t_0 and the element jet velocity V_j as given below.

$$z(x,t) = z_0(x) + (t - t_0)V_j(x) \tag{2.18}$$

The z coordinate is measured along the liner axis with an origin of user's choice and x represents the liner position of the Lagrangian element. Using the above expression and assuming jet incompressibility, time dependent jet radius distribution can be determined [12].

2.2 Analytical Modeling of Jet Breakup

In general, a shaped charge jet has a decreasing velocity from tip to tail. Because of this velocity distribution, shaped charge jet elongates, which results in a great penetration power. However, as a result of continuous elongation, radius of the jet decreases and necking occurs at particular locations on the jet. Eventually, jet breaks up into segments. After jet breakup, jet segments begin to tumble and disperse from the flight axis. Also, as the jet gets broken into small segments, it can no longer elongate as a whole and small jet segments tend to have a constant resultant velocity.

Jet breakup process is important to understand the affect of the standoff distance on the penetration performance of a shaped charge. Increasing standoff allows shaped charge jet to elongate and increasing jet length enables a greater penetration. However, as the jet breaks up, not all jet particles can reach the bottom of the

penetration crater due to their dispersing and tumbling behavior and this degrades the penetration performance. So, the optimum point of penetration-standoff curve is related to the breakup time of the jet. If the whole jet is assumed to breakup simultaneously, optimum standoff distance should be very close to the breakup distance; considering the combined effect of jet dispersion-tumbling and afterflow. Afterflow effect may cause a separated penetrator to have a better penetration performance compared to a solid penetrator. However, jet dispersion-tumbling is generally said to be the dominant effect for all practical purposes. Also note that, jet dispersion-tumbling after breakup depends on the homogeneity of shaped charge materials and precision of the production process.

As a result of the great influence of breakup on the penetration performance of a shaped charge jet, researchers showed a great interest to understand the nature of it. It is known that metals exhibit extreme ductility under dynamic conditions involved in the operation of shaped charge, and undergo dynamic elongations of 1000 % or more [15]. The problem is complicated by the fact that the material properties of the liner materials are not known well under the intense dynamic conditions involved in the collapse, formation and growth of the jet. The accuracy of the hydrocodes is also limited to the extent that how accurate material models attributed to liner material predict the dynamic behavior of it. Also the fracture mechanism involved is not fully understood.

One of the few methods to visualize and diagnose the shaped charge jet formation and elongation process is the flash X-ray method. In this method a long X-ray film is placed along the flight path of the jet and instantaneous x-ray photos of one or a few scenes are taken by X-ray illumination. Breakup time of the shaped charge jets can also be determined experimentally by a number of other ways, each leading to different results compared to the flash X-ray technique. Based on the experimental results, researchers developed a number of different semi-empirical formulas for the jet breakup time. Four of these formulations will be discussed next.

2.2.1 V_{pl} Breakup Model

This formula for the jet breakup time was developed by Hirsch [28]. In this formula the breakup time is related to the smallest characteristic dimension (original liner thickness) and an empirical constant V_{pl}. V_{pl} is called as "plastic velocity" by some authors, and some others consider it to be the velocity of the propagation of plastic instabilities on the jet. V_{pl} can also be understood as the average velocity difference between successive jet particles after breakup and this is observed in experiments. As a first assumption V_{pl} can be calculated as

$$V_{pl} = \sqrt{\frac{Y}{\rho_{liner}}} \tag{2.19}$$

where Y is the dynamic yield strength of liner material and ρ_{liner} is the liner material density. If there is available experimental data, V_{pl} can also be calculated as

$$V_{pl} = \frac{V_j - V_r}{n} \tag{2.20}$$

where V_j is the jet tip velocity, V_r is the velocity of the rear of the jet and n is the number of jet particles. If V_{pl} is known, breakup time t_b can be calculated as

$$t_b = \frac{2r_0}{V_{pl}} \tag{2.21}$$

where r_0 is the initial jet radius, measured at the moment of jet formation. The formula can also be represented using liner thickness, using the relation between liner thickness and collapse angle,

$$t_b = \frac{1}{V_{pl}}\sqrt{8\,R\,T_L}\sin\left(\frac{\beta}{2}\right) \tag{2.22}$$

where R and T_L are the radius and the thickness of the element, respectively and β is the collapse angle. Note that t_b must be calculated for each liner element, and reference time for t_b is arrival of the detonation wave to the liner element.

In the further work of Hirsch, SCAN code and a set of experiments with charges of varying liner thicknesses are used [28]. He stated that V_{pl} is a function of liner thickness and named $1/V_{pl}$ as specific breakup time of the liner, given by

$$\frac{1}{V_{pl}} = 13.886 - 101.49\frac{T_L}{CD} \tag{2.23}$$

where CD is the charge diameter. He stated that the dimension of the $1/V_{pl}$ is $\mu s/mm$ when V_{pl} is used in km/s. Equation 2.23 can be substituted into Equation 2.22 to calculate breakup time. Since Hirsch's formula does not take the strain rate into account, its application is limited. Interestingly, in his paper he stated that optimum liner thickness values for maximum energy transfer to the liner and maximum breakup time are different.

2.2.2 Pfeffer Model

Pfeffer gives the following jet breakup time formula by assuming that the breakup time is inversely proportional to the initial strain rate, depends weakly on the initial jet radius and is independent of the jet strength [15],

$$t_b = \frac{1.4}{\eta_0} + 48.5\frac{r_0}{C_0} \tag{2.24}$$

where $\eta_0$is the initial strain rate, $r_0$is the initial jet radius and C_0 is the shock velocity in the jet. Note that subscript 0 corresponds to the time when a liner element first reaches the symmetry axis and breakup time is given with respect to this time.

2.2.3 Chou-Carleone Model

Chou and Carleone expressed the following dimensionless breakup time, using results of a number of experiments with different charges [5]

$$\bar{t}_b = 3.75 - 0.125\bar{\eta}_0 + \frac{1}{\bar{\eta}_0} \tag{2.25}$$

where dimensionless breakup time and dimensionless initial strain are related to the corresponding dimensional terms as $\bar{t}_b = C_p t_b / r_0$, $\bar{\eta}_0 = \eta_0 r_0 / C_p$ and $C_p = \sqrt{Y/\rho_0}$. Chou and Carleone obtained this equation using a dynamic ductility value of 0.3, which is said to be in agreement with the experimental data available during the course of their study. Also they noted that if a different dynamic ductility is chosen, the constants in the equation must be changed. The dynamic yield strengths of some liner materials are given in Table 2-1, which are used in the calculation of C_p to calculate breakup time using Equation 2.25.

Table 2-1 Dynamic yield strength of some liner jet materials [5]

Liner material	Y, Jet Yield Strength (GPa)
Copper ETP	0.2
Copper OFHC	0.27
Aluminum	0.1

2.2.4 Chou Model

In his recent studies, Chou formulated the breakup time as follows, using curve fitting to experimental data

$$t_b = k\left(\frac{r^2 t}{{c_p}^2}\right)^{1/3} \tag{2.26}$$

where η is the strain rate, r is the jet radius and k is an experimental constant. Experimental constant k is reported to be 5 [15].

2.3 Analytical Modeling of Shaped Charge Penetration

Analytical models are capable of predicting the penetration of shaped charge jets into various target materials. Shaped charge penetration is a multi-disciplinary problem since shaped charges are used to penetrate or perforate armor, as well as rocks, soil, wood, ice and some other nonmetallic materials. Analytical models can provide fast predictions on early design stages in case time and computational resources are limited. The accuracy of these predictions may vary depending on the model used and the assumptions made.

2.3.1 Shaped Charge Penetration

Analytical penetration formulae usually assume one-dimensional flow and employ other simplifying assumptions. Early models were based on the Bernoulli principle. Later, empirical factors were introduced to account for non-uniform velocity distribution and particulation of the jet. Researchers also included terms to account

for jet and target strength effects, compressibility effects and the effects of the jet drift, particle dispersion and particle tumbling.

Birkhoff developed a simple penetration theory form the hydrodynamic theory of impinging jets [6]. Because of the high velocity of the shaped charge jet, pressures produced at the jet-target interface far exceed the yield strength of most materials. Therefore, as a first assumption, the strength and viscosity of both jet and target materials are neglected. By this way, hydrodynamic assumption of incompressible, inviscid flow can be used.

Consider a shaped charge jet with a constant velocity of V, penetrating into a stationary, semi-infinite, monolithic target with a resulting penetration velocity of U. Let us use a coordinate system moving with this velocity U. In this case, the target material is assumed to be moving with velocity U towards the jet, and the jet is moving with velocity $V - U$. A stationary surface exists at the jet-target interface with equal pressures on both sides. For this steady state process Bernoulli equation can be applied along an axial streamline, resulting in the following equation

$$\frac{1}{2}\rho_j(V-U)^2 = \frac{1}{2}\rho_t U^2 \tag{2.27}$$

where ρ_j is the density of the jet material and ρ_t is the density of the target material. Assuming that steady state conditions are reached instantaneously and penetration ceases when the rear of the jet reaches bottom of the hole created by the penetration, total amount of penetration P can be expressed as

$$P = l\sqrt{\frac{\rho_j}{\rho_t}} \tag{2.28}$$

l being the length of the jet. There are several limitations to this simple theory, such as

i-) According to this theory, penetration ceases as the rear of the jet reaches the bottom of the hole, meaning that the jet is totally consumed. However, at the instant the jet is consumed, the interface on the target has a certain velocity and inertia so that hole may grow in depth and in radial direction. This additional depth is known as the secondary penetration or afterflow. The penetration that occurs till the jet is consumed is called the primary penetration.

ii-) Penetration depends only on the density, as a material property. As a result, according to this theory, two different materials with the same density experience exactly same penetration, which disregards all other material characteristics including material strength, strain and strain rate. These properties affect penetration especially at low velocities, at which hydrodynamic assumption loses its validity.

iii-) For shaped charge jets the average penetration reaches an optimal value at a certain standoff distance. At standoff distances greater than the optimal value, penetration decreases due to tumbling and dispersion of the jet particles.

Pack and Evans noted the importance of target material strength on jet penetration [29]. To account for the strength effects, they proposed the following semi-empirical correction to Equation 2.28,

$$P = l\sqrt{\frac{\rho_j}{\rho_t}}\left(1 - \frac{\alpha Y}{\rho_j V^2}\right) \tag{2.29}$$

where Y is the yield strength of the target material and α is an experimental constant. They showed that for steel the correction term $\alpha Y/\rho_j V^2$ is as great as 0.3, that is the effect of material strength on penetration can be as high as 30 %. Also note that, having the V^2 term on the denominator; strength effects are more dominant at low velocities, as expected. For the penetration into ductile targets, such as lead, it is recommended to add a secondary penetration term that is equal to the radius of the hole created by the jet.

Tate and Alekseevski also modified the hydrodynamic penetration theory to take account for target and penetrator strengths [17]. In some references, this theory is also known as "modified hydrodynamic penetration theory". To account for target and penetrator resistances, the target and penetrator resistance terms R_t and Y_p are added to the hydrodynamic equation, for the stress levels over which material behaves hydrodynamically. These terms are different from the static yield stresses of the materials instead they define materials resistance to hydrodynamic penetration. Tate-Alekseevski penetration equation is given as

$$\frac{1}{2}\rho_t U^2 + R_t = \frac{1}{2}\rho_p (V-U)^2 + Y_p \tag{2.30}$$

For the terms Y_p and R_t different correlations based on yield stresses are given. In Rosenberg and Dekel, 4.5 times the yield stress is suggested for RHA [17]. They suggested the use of a yield stresses factor of 4-5 for aluminum targets of different kind, and a factor of 5-6 for steel targets. For the analytical penetration calculations of this study, a yield stress factor of 4.5 is used for RHA steel. However it is more accurate to use different factors for different targets, and it is better to correlate the results with experimental data [18].

Matuska investigated steady-state jet penetration by a computational approach [13]. Based on the simulations with the two-dimensional Eulerian hydrocode HULL, he determined the values of the parameters of the following modified Bernoulli equation

$$\frac{\gamma}{2}\rho_j (V-U)^2 + \beta\sigma_j = \frac{\rho_t U^2}{2} + \alpha\sigma_t \tag{2.31}$$

where $\alpha = 1$, $\beta = 0.3$ and $\gamma = 0.47 + 0.028\rho_j - 0.00086{\rho_j}^2 + 0.072 \ln V$. All one-dimensional analytical models need to use a V_{min} criterion to simulate the termination of the penetration. This is because the physical phenomena of wavering and tumbling of jet particles after break-up can not be modeled by one-dimensional models. Some analytical models use a U_{min} criterion instead of V_{min}; and

terminating penetration this way leads to more accurate results. However, studies show that both V_{min} and U_{min} vary strongly with jet and target materials, standoff and charge diameter. So, both termination criteria are actually case dependent and it is advised to support analytical models with experimental data and numerical analyses.

In some analytical models Monte Carlo technique is applied to model the effect of tumbling and dispersion of jet particles, which are considered as stochastic processes. It is claimed that, with proper selection of statistical parameters for dispersion of jet particles, excellent agreement with the test results can be achieved. After the jet particles are distributed according to the statistical distribution, a suitable penetration model can be applied.

2.3.2 Crater Growth Process

Penetration formulas discussed in the previous section are used to calculate the penetration depth, for given jet and target parameters. Since these formulas are solving penetration problem in 1-D, only penetration depth in the line of sight of the jet can be obtained. Separate formulas must be used to find the crater radius of the penetration hole. These formulas are again 1-D formulas and use the previously calculated penetration velocity as an input. One of the crater growth formulas is given by Held as [20],

$$r_c(t) = \sqrt{\frac{A}{B} - \left(\sqrt{\frac{A}{B} - {r_j}^2} - t\sqrt{B}\right)^2} \tag{2.32a}$$

$$A = {r_j}^2 u^2 \tag{2.32b}$$

$$B = 0.5\frac{R_{t(R)}}{\rho_t} \tag{2.32c}$$

where r_j is the jet radius, ρ_t is the target density, u is the penetration velocity and $R_{t(R)}$ is the target resistance to radial crater growth. $R_{t(R)}$ term is different from the target resistance term R_t used in the penetration depth formulas. It represents the resistance of the target to radial crater growth. Radial cratering velocity decreases from the penetration velocity u to zero in time [20]. This causes the target to deform with an initially high strain rate, in contrast to the penetration in the axial direction. As a result, resistance of the target to radial cratering is lower than that in the penetration direction. For these reasons, targets resistance to radial cratering is taken to be half of the penetration resistance in this study.

Note that, in Equation 2.32a crater radius is given with respect to cratering time. The maximum radius of the fully formed crater is given as

$$r_{cm} = \sqrt{\frac{A}{B}} \tag{2.33}$$

2.4 Numerical Modeling of Shaped Charges

Besides the analytical formulae given in the previous sections, highly nonlinear and time-dependent events, like shaped charge jet formation and penetration, can also be

simulated using transient, dynamic wave propagation codes, called hydrocodes [16]. The name "hydrocode" refers to the codes that are generally used for the problems involving large pressures so that material strength can be neglected. Recent and most commonly used commercial hydrocodes are AUTODYN, LS-DYNA and DYTRAN. AUTODYN is used for the numerical simulations of this study. It utilizes the differential equations governing unsteady material dynamic motion expressed as the conservation of mass, momentum and energy.

AUTODYN has different solver types corresponding to different numerical solution methods. The solver types are Lagrange, Euler, Arbitrary Lagrange Euler and Smoothed Particle Hydrodynamics. In the current study Lagrange solver is used for penetration problems and Euler solver is used for jet formation problems. There is a "Jetting" option present in the Euler solver, which is also invoked in the jet formation problems as an alternative. In the following sections numerical solver types are discussed briefly, based on the AUTODYN Theory Manual [30].

2.4.1 Lagrange Solver

The Lagrangian method in AUTODYN is derived from the HEMP code developed by Wilkins. The Lagrange solver operates on a structured numerical mesh. The term, "mesh" is used to define the numerical grid used in the solution procedure. In the Lagrangian description, nodes of the mesh move with the material flow velocity. Material remains within its initial cell definition with no transport from cell to cell. Since material remains within the cell, strain calculations are more accurate in Lagrange solvers.

Compared to the Eulerian approach, which will be discussed below, the Lagrangian formulation tends to be faster computationally since there is no transport of material through the mesh. Also, since no material transport form cell to cell is possible, only the materials present in the problem need to be meshed, rather than meshing the space that surrounds materials.

The major disadvantage of Lagrange solver is that if excessive material movement occurs, the numerical mesh may become highly distorted leading to an inaccurate and inefficient solution. Further, this may also lead to the improper termination of the solution. Erosion technique is used for the treatment of highly distorted mesh cases. Procedures are incorporated into AUTODYN hydrocode to remove highly distorted cells from the calculation, once a predefined strain (instantaneous geometric strain, incremental geometric strain or effective plastic strain) exceeds a specified limit. Once a cell is removed from the calculation process, the mass within that cell can either be discarded or distributed to the corner nodes of the cell. If the mass is retained, conservation of inertia and spatial continuity of inertia are maintained. However compressive strength and internal energy of the material within the cell are lost whether or not the mass is retained. This discard model is known as erosion. However it is important to note that, in general, this is not the true modeling of a physical phenomena but only a numerical treatment introduced to overcome the difficulties associated with the abrupt mesh geometry changes. In general users are recommended to use limiting values as high as possible in absence of any experimental evidence.

Lagrange solver is used for the penetration problems in this thesis work. Euler jet formation simulation results are used as an input to the penetration problems. Penetration depth and crater radius are obtained as a result of the Lagrangian simulations.

2.4.2 Euler Solver

In the Euler solver, a control volume method is used to solve the equations that govern conservation of mass, momentum and energy. The integral and discrete forms of these equations are expressed in conservation form to obtain accurate and stable solutions. A two step numerical procedure is used to solve the finite difference equations. In the first step, which is the called as Lagrangian step, the Lagrangian

form of the equations are updated or advanced one time interval (time step). In the second step, the Euler step, updated variables are mapped onto the Eulerian mesh. Multiple materials are handled either through a volume fraction technique or an interface capturing technique. All variables are stored in a cell centered fashion.

Euler solver is suitable for handling problems including large deformations and fluid flow. However, it is difficult to track free surfaces, material interfaces and history dependent material behavior. Also, Euler solver is computationally less efficient in a way that the mesh of the problem needs to be extended beyond the initial physical material limits since material is allowed to flow out of these initial limits.

In this thesis work Eulerian solver is used to simulate jet formation problems. The results can be directly used in the penetration solution with Lagrange solver by the methods available in AUTODYN. Alternatively results can be processed by user to be used in further analytical calculations, as it is done in analytical breakup and penetration calculations discussed later in the text.

AUTODYN has a “Jetting” option that can be used to simulate shaped charge problems. If jetting options is used, jet collapse and formation parameters can be calculated without modeling the liner in the Eulerian mesh. In the jetting option, the charge is modeled same as the Euler solver except liner. The liner is modeled as shell Lagrangian elements. As the Lagrange and Euler solvers are coupled, the resultant pressure forces of explosive detonation solution are applied to Lagrangian liner elements. As the Lagrangian elements collapse and enter a pre-calculated jetting zone, analytical jetting calculations are performed. With the jetting option; collapse velocity, collapse angle, deflection angle, jet and slug masses, jet and slug velocities can be obtained as an output.

CHAPTER 3

ANALYSIS OF JET FORMATION

3.1 Numerical Simulations with AUTODYN-Euler Solver

Numerical simulations of warhead and target interaction are a vital supplement to design and testing of warhead systems. In this thesis work, AUTODYN software is used for numerical simulation of shaped charge jet formation and target penetration. Euler solver of the AUTODYN is used in jet formation simulations and Lagrange solver is used for penetration simulations. "Jetting" option in Euler solver of the AUTODYN is also invoked to simulate jet formation, as an alternative.

For the numerical simulations presented in this chapter the standard charge of BRL-82 mm (BRL 3.3 inch) is used, since the geometry and some of the performance data of this warhead are available in the literature. The shape and the dimensions of BRL-82 can be seen in Figure 1-3. This warhead is known to be a "precision warhead" because of its carefully controlled manufacturing process that provides very small tolerances on the wall thickness and concentricity of the liner.

The equation of state and material models used in the model are given in Table 3-1. In this table, the medium surrounding the shaped charge is given as background material. In AUTODYN, cells that are not occupied by any material are simulated as

they are occupied by void material, meaning that these cells are empty but they are still included in the computational model. JWL equation of state is a programmed detonation model for explosives. Shock equation of state relates density, pressure, internal energy, particle velocity and shock velocity considering Rankine-Hugoniot equations, and used for the problems including high pressure and strain rate deformations.

Table 3-1 EOS and material models used in the jet formation simulations

Part	**Material**	**Equation of State**	**Strength Model**
Liner	Cu-OFHC	Shock	Steinberg-Guinan
Case	Aluminum 6061-T6	Shock	None
Explosive	Octol	JWL	None
Background	Void	Void	None

Table 3-2 provides a comparison of the masses of different parts of the actual warhead and its numerical model. The differences are thought to be due to certain unknown dimensions of the warhead. As it is seen the liner mass is modeled accurately. Large difference for the casing mass is due to the booster gap at the back of the casing. In the original charge design, polycarbonate booster holder is mounted in that space. However, this is modeled as a part of the aluminum casing, following the work of Bolstad and Mandell [3]. Since the calculated jet tip velocity and jet velocity distribution are compared with the results of Bolstad and Mandell, the same modeling approach is used in the current study.

Table 3-2 Comparison of the actual and modeled masses of shaped charge parts modeled in simulations

Part	**Calculated Mass (grams)**	**Reported Mass (grams)**
Liner	279	277
Casing	579	517
Explosive	909	875

Figure 3-1 shows the whole computational model and its dimensions. Details of the initial configuration of the shaped charge can be seen in Figure 3-2. Flow-out boundary condition is applied to all computational borders except the symmetry axis. This allows the expanding detonation products and the casing to leave the computational domain without interacting with its boundaries.

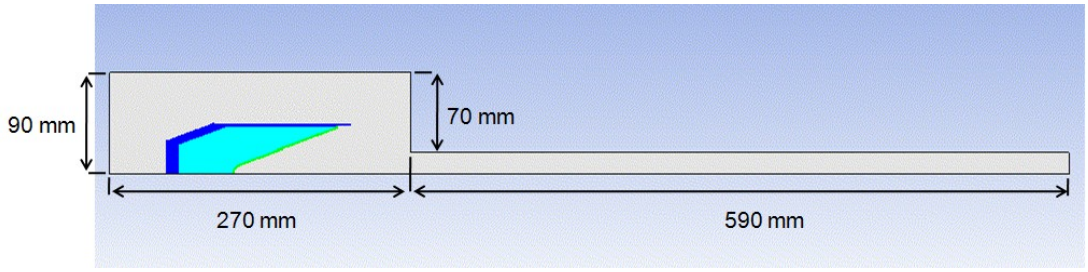

Figure 3-1 Dimensions of the computational model used in the jet formation simulations with the AUTODYN-Euler solver

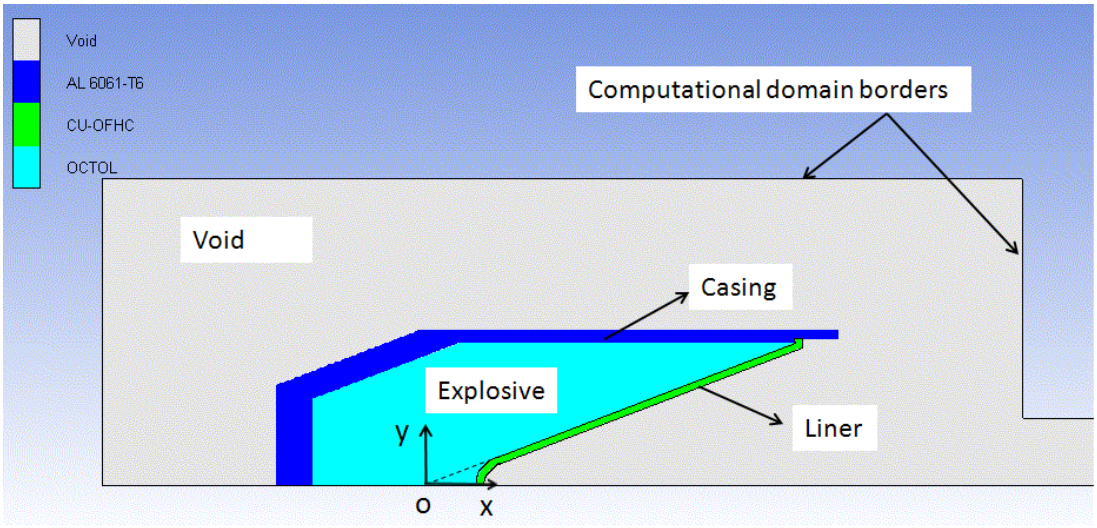

Figure 3-2 Details of the initial configuration of the shaped charge used in the jet formation simulations with AUTODYN-Euler solver

In the simulation model, fixed gauge points are located the positions shown in Figure 3-3 to measure the local variables such velocity, density, pressure and temperature. At each gauge point local variables are written to the history file of the simulation at a user defined time increment. This is used to analyze, the variation of local variables with respect to time. Also the variation of jet variables in the axial direction can be investigated by comparing the data of gauge points at different axial locations.

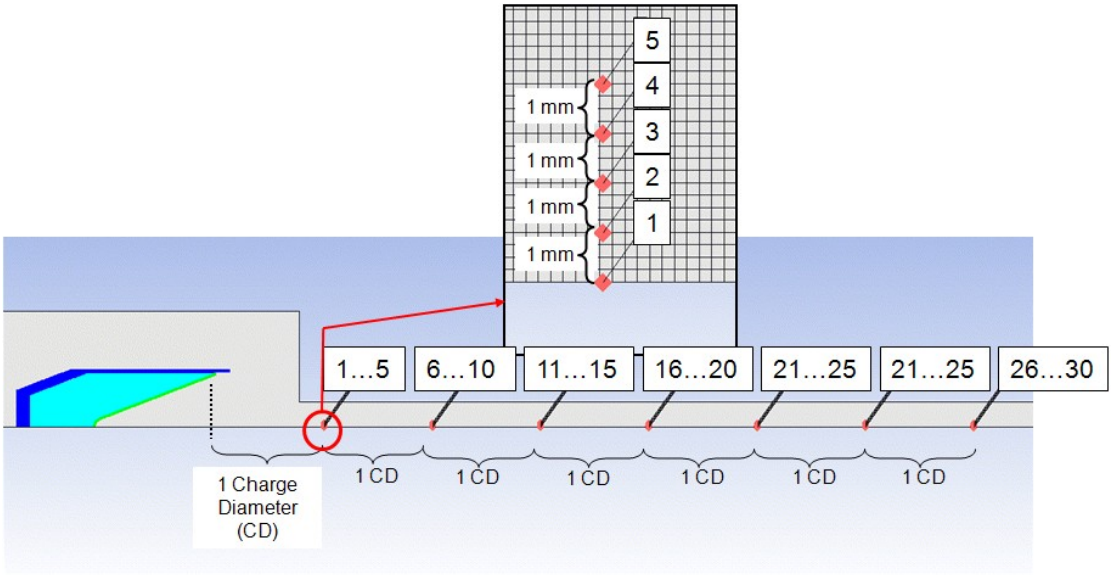

Figure 3-3 Location of gauge points in AUTODYN-Euler jet formation simulations

Cell size and distribution of a typical mesh used in the jet formation studies is shown in Figure 3-4. The regions of charge, jet formation and elongation zone are meshed with uniform, 1 mm size, square cells. To reduce the total amount of cells, larger cells are used in the rear and the upper radial regions of the charge, since these regions have less significance on the physics of the problem.

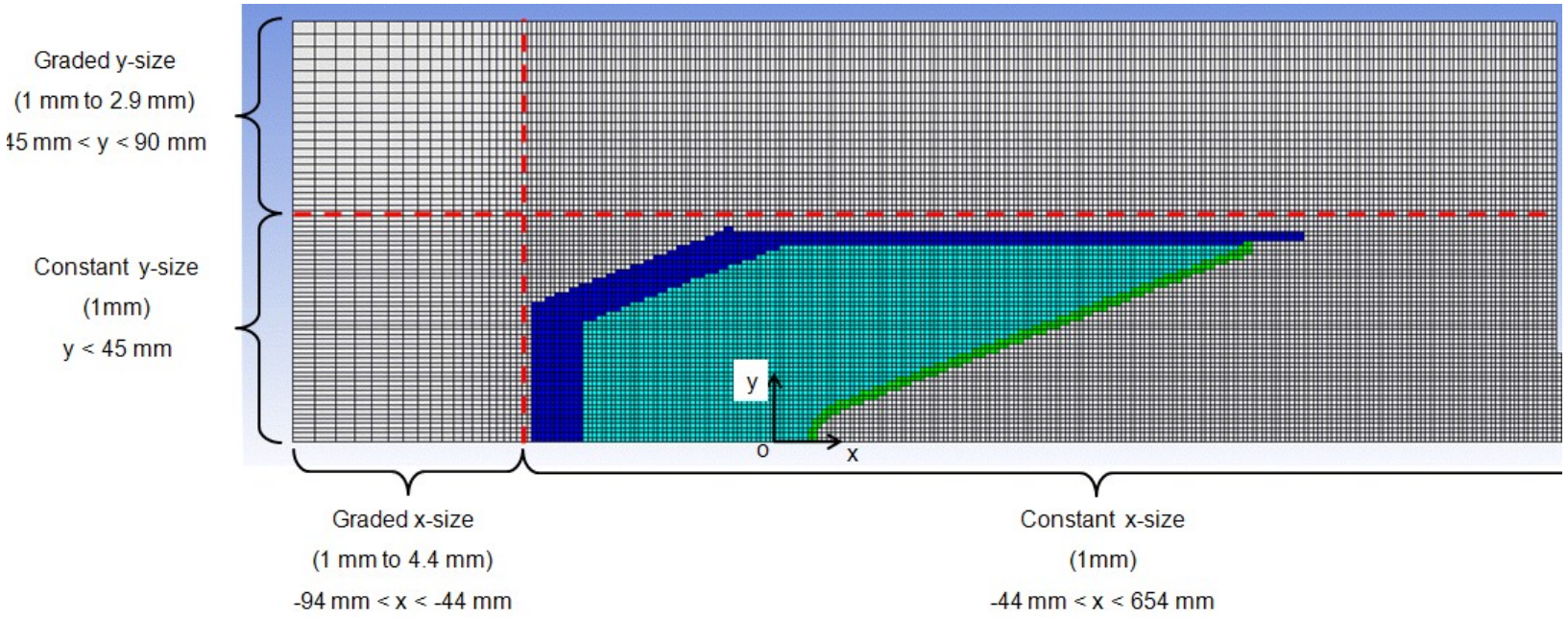

Figure 3-4 Mesh distribution of the computational model, using 1 mm square cells for the jet formation region

3.1.1 Mesh sensitivity study

It is a known fact that the number and shape of the elements in a mesh affects the simulation results. As a general behavior, simulations with smaller cells provide more accurate results. However, since the computational resources necessary to perform a simulation directly depends on the mesh size, in order to utilize available resources more effectively on time basis, it is good to study this dependency for the particular problem.

In the mesh sensitivity study four different meshes are used. In all these meshes uniform and square cells are used in the jet formation region. The size of these cells are selected to be 1, 0.5, 0.25 and 0.125 mm. Total number of cells in each mesh and the memory requirement of the simulations are given in Table 3-3.

Table 3-3 Computational resource requirement for different cell sizes

	0.125 mm	**0.25 mm**	**0.5 mm**	**1 mm**
Total cell number	1,284,061	458,841	338,589	115,021
Memory requirement (MB)	1,100*	630	225	130

* Jet elongation part of the computational domain is reduced to 2 CD standoff distance; whereas it is 7 for the remaining simulations.

Velocity profiles of the jet on the central axis for four different meshes are given in Figure 3-5 and 3-6, at t=20 μs and t=70 μs, respectively. The figures also provide a comparison with the numerical simulation results of Bolstad and Mandell [3]. In these figures, jet length is measured along the x-axis in the simulations with the

origin being the rearmost point of the slug. The same method is also applied for the upcoming jet velocity comparison figures. Because of the velocity differences, jet length is different for different meshes. Note that, the velocity profile at 70 μs can not be obtained for the 0.125 mm cell case because the memory requirement exceeds the limits of the available hardware. It is seen from the Figure 3-5 and 3-6 that the velocity of the tip region increases as the mesh becomes finer. However, except the tip formation region, the velocity profiles for all meshes are very similar. Also the differences in the jet tip formation region between different meshes get smaller as the mesh becomes finer. Note that, the stepwise behavior of the velocity profiles, especially for 1 mm mesh, is due to the constant number of 1000 data points used in generating the profile plot. If the cell size is larger than the spacing between the data points of the profile plot, the average data at the cell is attributed to the relevant data points, which creates this stepwise behavior.

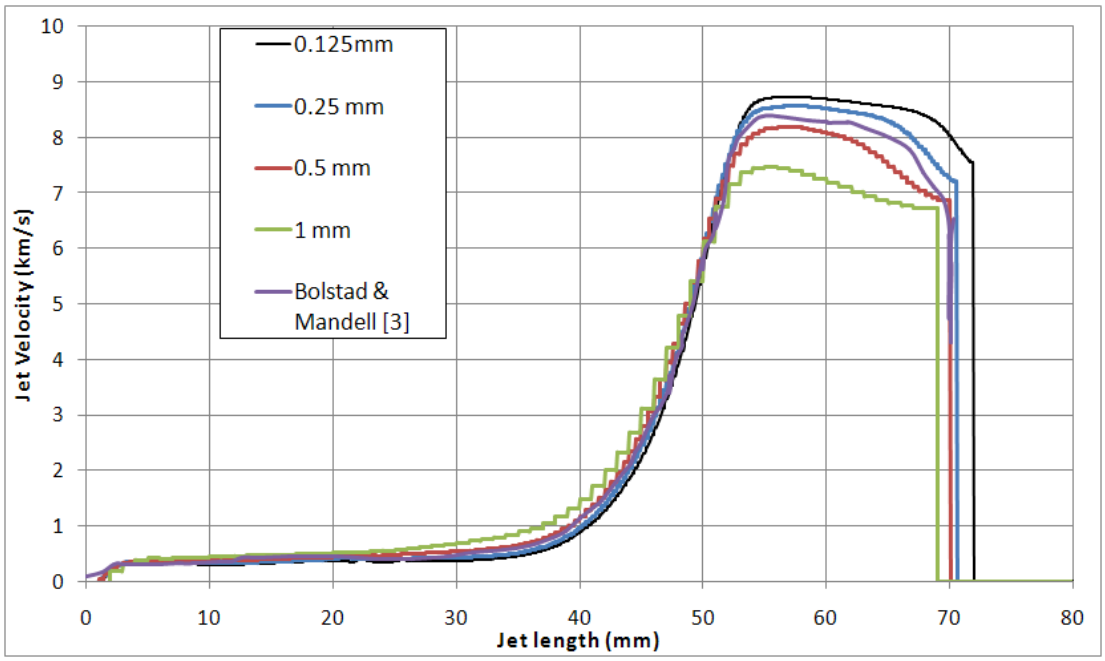

Figure 3-5 Centerline velocity profiles of 4 different meshes at 20 μs, in comparison with the reference data

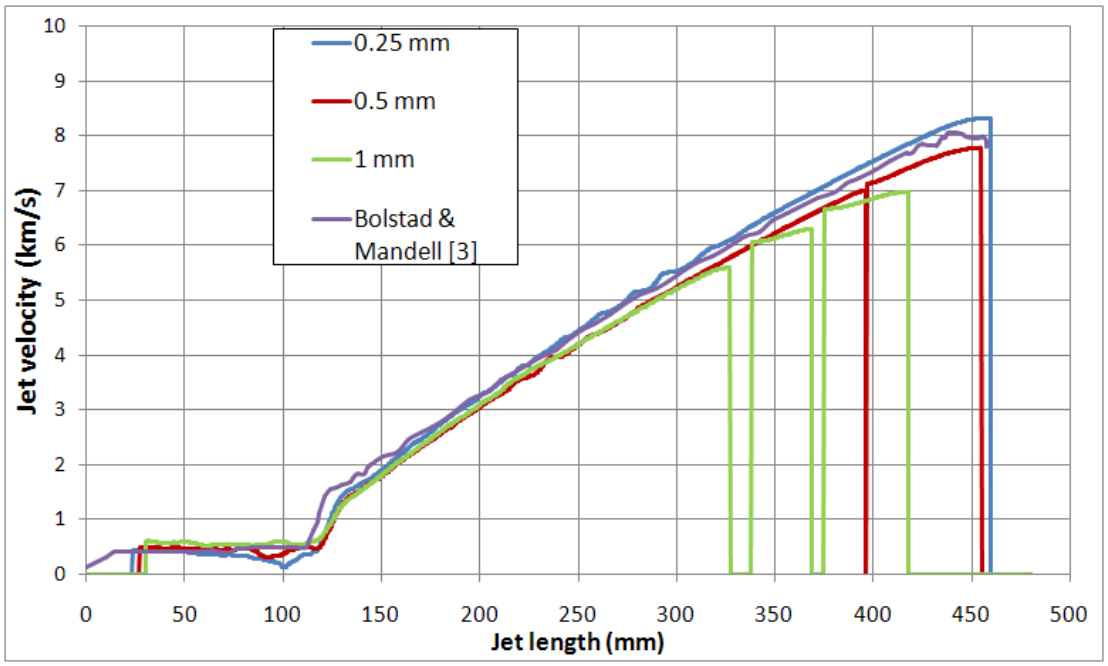

Figure 3-6 Centerline velocity profiles of 4 different meshes at 70 µs, in comparison with the reference data

Change of the jet tip velocity with cell size is given in Figure 3-7. The comparison is performed at 50 µs, which approximately corresponds to the beginning time of the penetration simulations, discussed in section-5. Bolstad and Mandell state that the jet tip velocity in their simulations approaches to 8300 m/s, which is close to the experimental data they use [3]. However, in the current AUTODYN simulations, this limiting value of the jet tip velocity is found to be 8800 m/s.

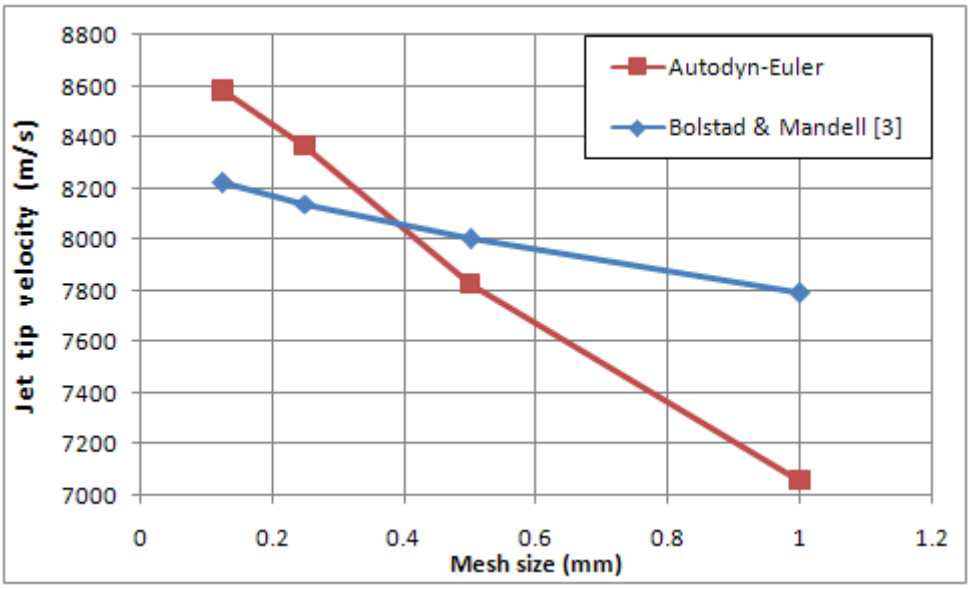

Figure 3-7 Change of the jet tip velocity with cell size at 50 μs, in comparison with reference data

The pressure calculated in the jet collapse zone at t=20 μs for different meshes are given in Figure 3-8. Bolstad and Mandell report the pressure in the jet collapse zone to be about 0.7 Mbar [3]. It is seen that the simulation with 0.25 mm cell size provides this pressure value almost exactly. Also it is observed that the calculated pressure in the simulations in the collapse zone increases as the cell size tends to zero.

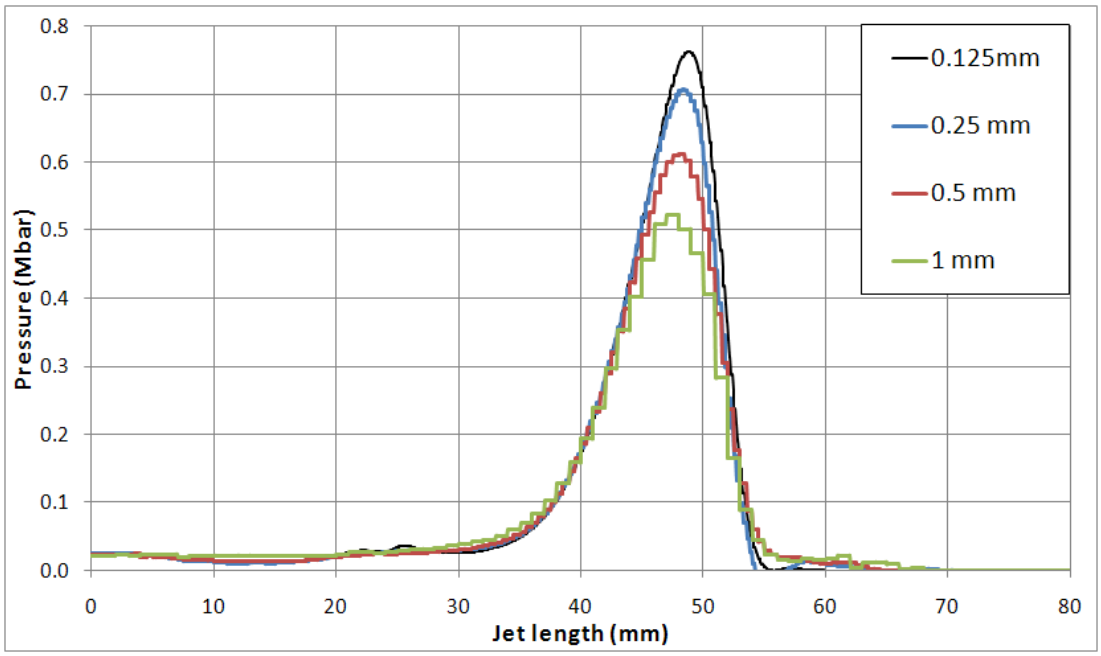

Figure 3-8 Pressure profiles of the stagnation zone for 4 different meshes at 20 μs

It can be concluded from the simulation results that, 0.25 mm cell size gives results in acceptable accuracy when compared with the available experimental data reported by Bolstad and Mandell [3].

3.1.2 Effect of using cells with a non-unity aspect ratio

In the jet formation simulations, once the jet is formed, it elongates continuously due to the velocity difference between its tip and tail regions. In the jet elongation region, the velocity of the jet is mainly in the *x*-direction. An *x*-graded mesh can be used in the jet elongation region to decrease the total amount of cells in that region without affecting the jet velocity distribution considerably. For the simulations of this section three new computational grids containing cells with aspect ratios of up to 2, 4 and 8 are used and the results are compared with the uniform grid of 0.25 mm cells. As seen in the region where the graded mesh starts is chosen to be 50 mm away from cone base, allowing the jet to be formed in 0.25 mm cells.

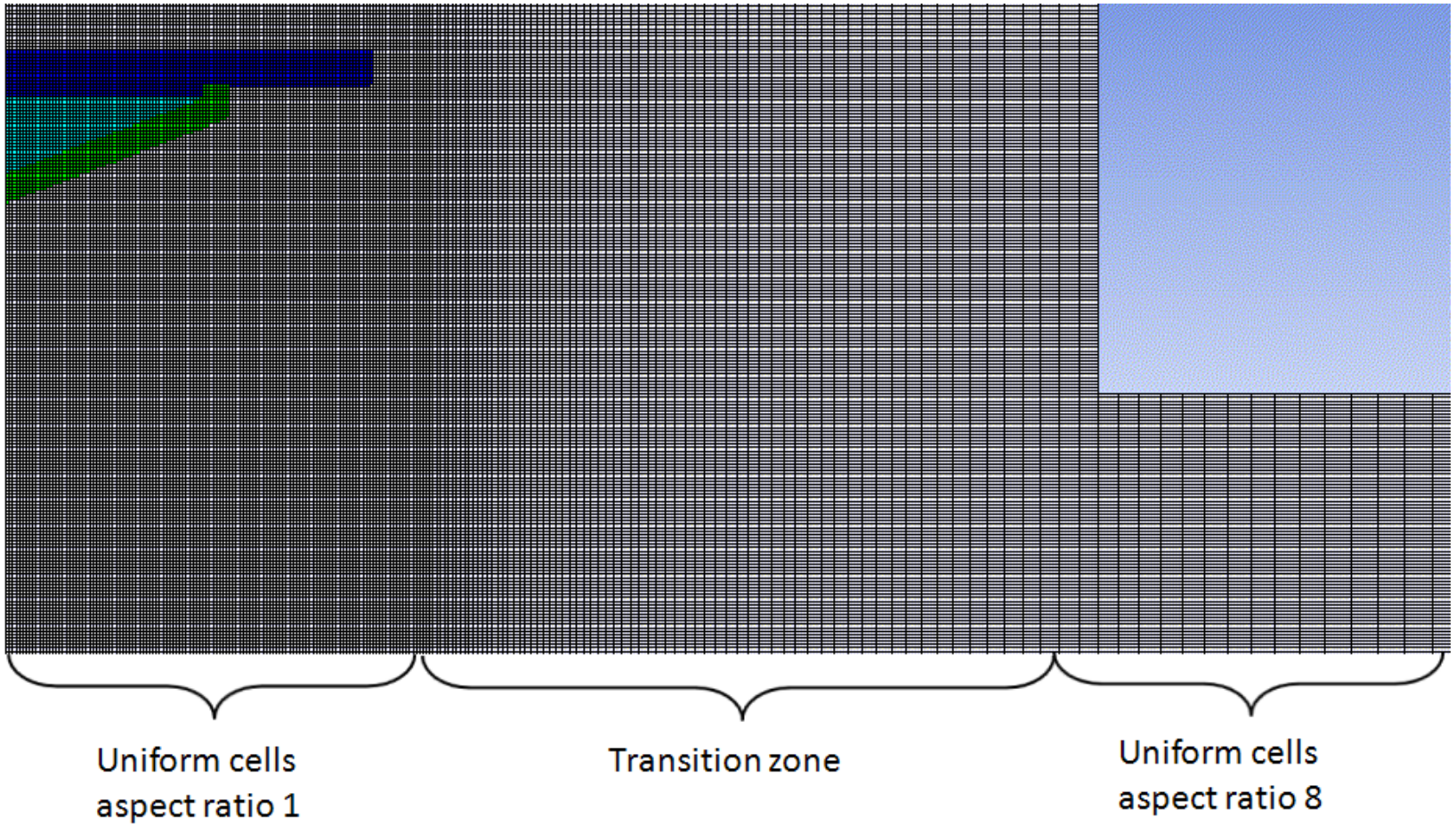

Figure 3-9 A section of the jet formation simulation model having cells ranging from aspect ratio 1 to 8

In the transition region between uniform and non-uniform cells, a factor of 1.025 is used to increase the axial dimension of each cell with respect to the cell behind it.

In Figure 3-10, the jet velocity distribution at t=70 μs, obtained using meshes of different aspect ratio cells are given. In Table 3-4 the tip velocities obtained in these simulations are compared with the available experimental data. As seen the use of elongated and therefore less number of cells in the jet elongation region has a negligibly small effect on the jet velocity distribution and the jet tip velocity.

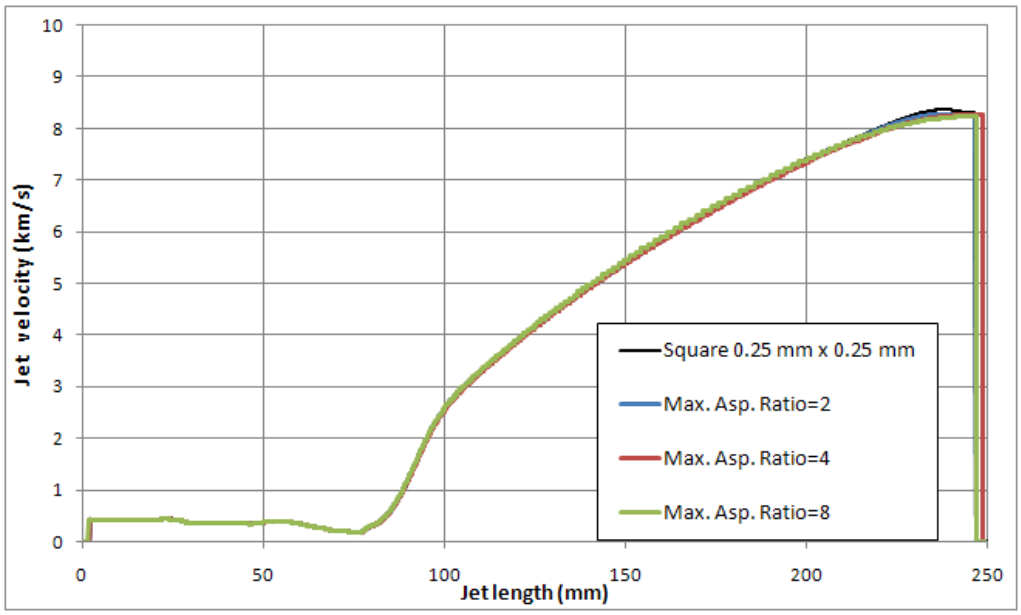

Figure 3-10 Jet velocity profiles for meshes of 4 different aspect ratios at 70 μs

Table 3-4 Jet tip velocities obtained using meshes with cells of different aspect ratios

Aspect ratio	Tip velocity (m/s)	Experimental value [3] (m/s)	% Difference wrt exp. (m/s)
1	8366	8300	0.8
2	8281	8300	0.2
4	8267	8300	0.4
8	8233	8300	0.8

In Figure 3-11, the change of tip velocity with increasing standoff distance is given for cells with different aspect ratios. With increasing standoff distance, the tip velocity differences between simulations with cells of different aspect ratios increase (see Figure 3-11). Since no experimental data is available for the decrease of jet velocity with respect to the standoff distance, it is wiser to use cells with unity aspect ratio for long standoff distances.

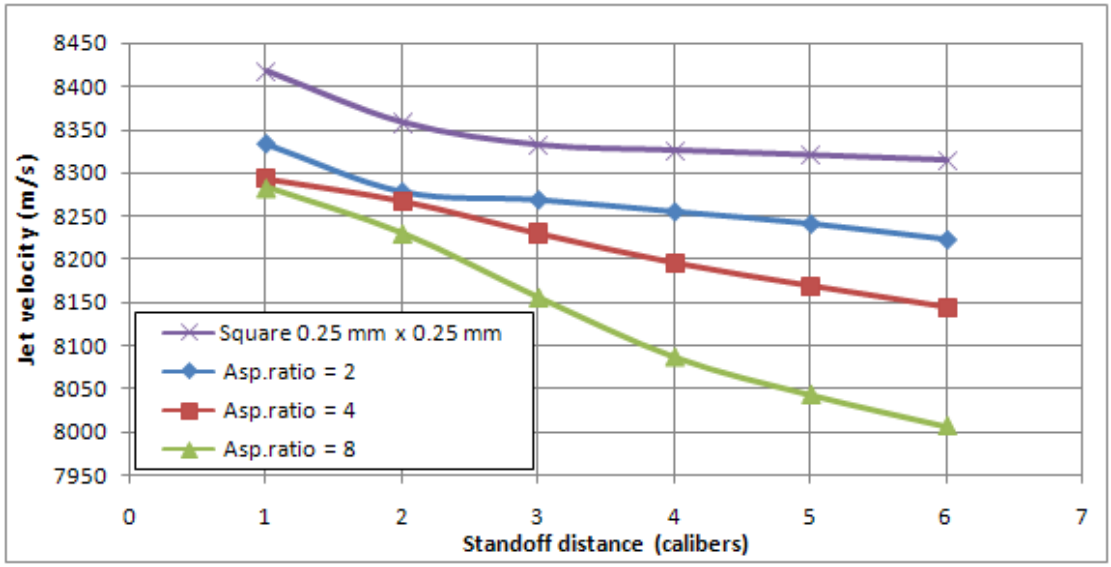

Figure 3-11 Change of jet tip velocity with standoff distance for meshes with cells of different aspect ratios

In Table 3-5 the total cell number and memory requirement for simulations using uniform cells and cells with aspect ratios up to 2, 4, and 8 are provided. It is observed that the total number of cells can be reduced to nearly half by using cells of aspect ratio up to 8, compared to unity aspect ratio cells. As a result memory requirement during the simulations reduces by half. Also it is shown that jet velocity distribution is almost the same for cells of aspect ratios up to 8. Note that, even by using cells of aspect ratio 2, memory requirement during the simulations is reduced by almost 25 %, with no significant change in jet velocity. Although not measured for each case, it is obvious that the decrease in total number of cells means a decrease in computation time. It can be concluded that, memory requirement and computation time can be

reduced by using cells having aspect ratios greater than unity, without losing considerable level of accuracy in jet velocity results.

Table 3-5 Total cell number and memory requirement of meshes with cells of different aspect ratios

	Aspect ratio=1	**Aspect ratio=2**	**Aspect ratio=4**	**Aspect ratio=8**
Total cell number	458841	338589	282397	257353
Memory requirement (MB)	630	490	390	341

3.1.3 Effect of forming jet in void instead of air

Simulating jet formation in void instead of air is a commonly used simplification. If the jet formation can be simulated in void, one less material is included in the model, which reduces the number of calculations that needs to be performed. Using one less material can also reduce the number of mixed material cells, in which more complicated calculations and material transport algorithms have to be processed. One drawback of forming jet in void rather than air is that, air drag as a result of the flight of jet in air can not be modeled. The affect of this simplification will be investigated in this section.

A fixed cell size of 0.25 mm is used for the simulations of this section. Velocity distribution of the jet on the axis of symmetry at t = 50 μs is compared for simulations with air and void as the surrounding medium. The resultant tip velocity of the jet is 8281 m/s and 8327 m/s for the simulations without and with air, respectively. This corresponds to a tip velocity difference of 0.54 % with respect to

the result with air. Both simulation results are close to the experimental jet tip velocity of 8300 m/s [3].

The reduction of the jet tip velocity for the simulation performed in air can be attained to the air drag, but also it can be a result of multi-material transport algorithms. To further investigate this possibility, data from 1 to 6 CD standoff gauge points are compared as shown in Figure 3-12. In this figure change of jet tip velocity for the simulations performed in air and void are compared at different standoff distances. As seen, there is no significant difference of jet tip velocity in the range of 1 to 3 CD standoff distance. However, starting from 3 CD standoff distance, jet tip velocity in air reduces approximately linearly, whereas it stays almost constant for the jet traveling in void. Through a linear regression calculation, it is found that the jet tip velocity in air decays with a linear rate of 36.45 m/s per CD standoff distance.

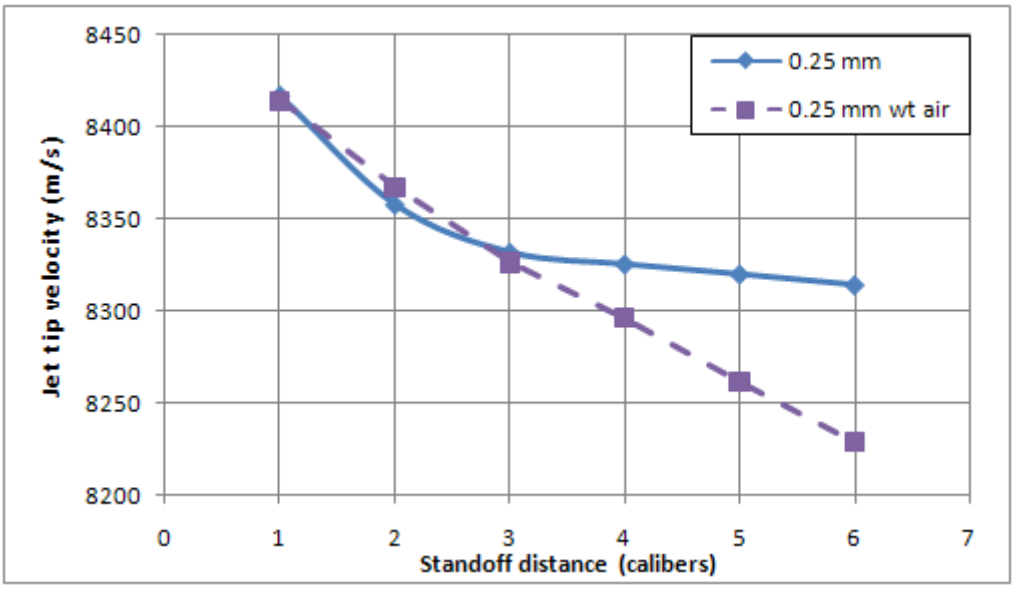

Figure 3-12 Change of jet tip velocity with standoff distance for the simulations with and without air

For the simulation with void, a possible reason for the sharp decrease in tip velocity before 2 CD standoff is the formation of the jet tip. The slow decrease of the tip velocity after 2 CD standoff can be explained by the hydrodynamic forces acting on the jet. Since the tip of the jet is moving faster than its tail, the tail can be considered as pulling the tip back and the tip is pulling the tail forward. As a consequence of these hydrodynamic forces the jet will break-up, and broken jet particles will attain a constant speed, eventually. On the other hand, the jet traveling in air is also interacting with air in addition to these effects.

It can be concluded that up to 3 CD standoff, forming jet in void instead of air makes no significant difference in terms of the jet tip velocity. However for longer standoff distances the effect of air is not negligible anymore and the jet must be formed in air to take the air drag effect into account.

3.2 Analytical Model to Simulate Jet Formation

For the shaped charge warhead design process, generally hydrocodes like DYNA 2D & 3D, AUTODYN and LS-DYNA are used. Hydrocodes are advantageous in the sense that they solve all the governing equations of the physical process. Recent hydrocodes are capable of solving jet formation and penetration processes using Lagrange and Euler solvers, as well as hybrid solvers like ALE and SPH. Also they may have their own material libraries and constants for equation of state and constitutive equations. Hydrocodes are also adaptable to different types of problems (e.g. waveshaping, ring initiation, bi-conic liners) and they can be used with complex geometries. However, they require long computational times. Also experienced users are necessary for both geometric modeling of complex problem domains and physical modeling of the problem. In design processes with large numbers of design alternatives, very large number of simulations must be performed for the optimization of the final design. Quite often, it is desirable to have a simplified

procedure for addressing parametric design studies quickly and economically. Analytical codes can be employed for this purpose.

Analytical codes use experimental and theoretical formulations to model the jet formation process. These codes generally require very small amount of computational power and time. Also they are very suitable for optimization processes since they can be coupled with optimization codes. Last but not the least, numerical hydrocode software are not suitable for investigating response of the solution to a single parameter. For example; one may not be able to investigate the collapse angle in a jet formation solution with an Euler solver. For collapse angle to be calculated, collapse paths of each liner element should be tracked. But this can not be achieved with Euler solver since it does not keep track of material movement. However calculations are not on element basis but on material flow. However, analytical codes allow users to investigate and participate in every step of the solution.

The analytical code developed in this study uses the PER metal acceleration theory. Collapse angle is calculated using the formulas that include the unsteady effects. Acceleration of the liner element by the impinging detonation wave is calculated with exponential acceleration term. When detonation wave sweeps across a liner element, several shock reverberations are required for the acceleration to be completed. Material near the apex of the liner cone can enter the collapse zone long before the liner is accelerated fully and hence does not reach its ultimate velocity. This leads to the "inverse velocity gradient effect" where the successive collapsing jet elements collapse and build-up a jet tip. For the calculation of the jet tip velocity, collapse of jet elements are controlled and velocities of individual liner elements are updated at each time step. The collapse point of each liner element is calculated so that element size, radius, strain rate and break-up time can be calculated. Several break-up theories by different researchers are used to calculate the break-up time. Calculation of break-up time in a jet formation study is important in the sense that it allows the understanding of the penetration behavior of jet with respect to standoff distance. The flowchart of the written analytical code is given in Figure 3-13.

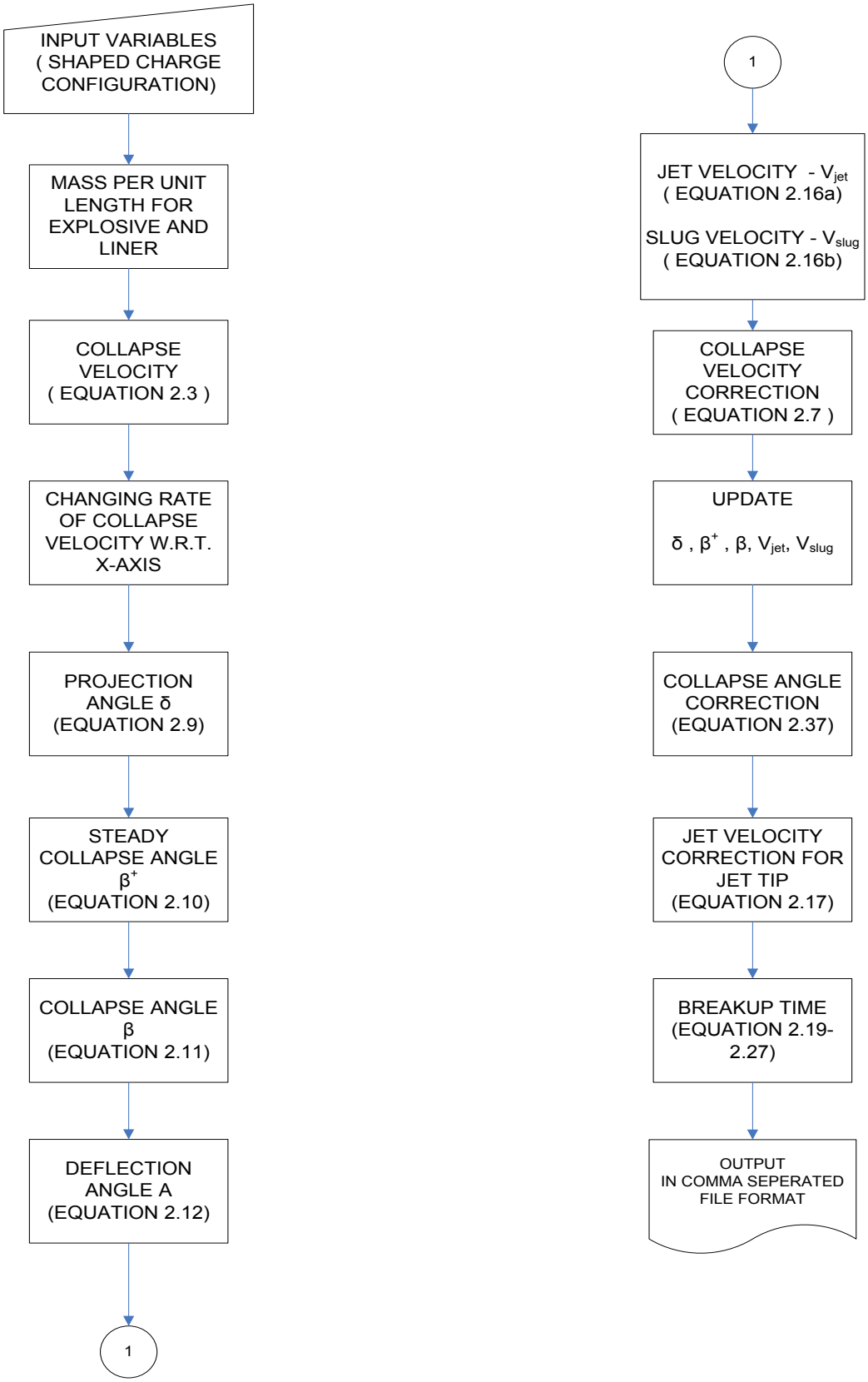

Figure 3-13 Flowchart of the analytical jet formation calculations

In Table 3-6 input parameters of the liner and explosive used in the analytical calculations are given.

Table 3-6 Input parameters for the analytical jet formation calculations

Input Parameter	Value	
Liner		
Diameter	82	mm
Thickness	2.05	mm
Cone angle	42	degrees
Density	8.9	g/cm^3
Explosive		
Detonation velocity	8480	m/s
Density	1.65	g/cm^3
Gurney velocity	2800	m/s

3.2.1 Liner Acceleration

For the calculation of the collapse velocity V_0, several models by different researchers are available. All these models use an empirically or theoretically determined relation between collapse velocity V_0 and liner-to-charge mass ratio μ. Some of the models use detonation velocity as an input and some use the Gurney velocity $\sqrt{2E}$. However, there exist a unique constant between Gurney velocity and detonation velocity D for a specific explosive, which is generally between 0.3 and 0.4. So it can be concluded that collapse velocity V_0 depends on μ and D. In Figure 3-14 comparison of collapse velocity models are given, calculated using μ and D (or $\sqrt{2E}$, when necessary) of the current problem

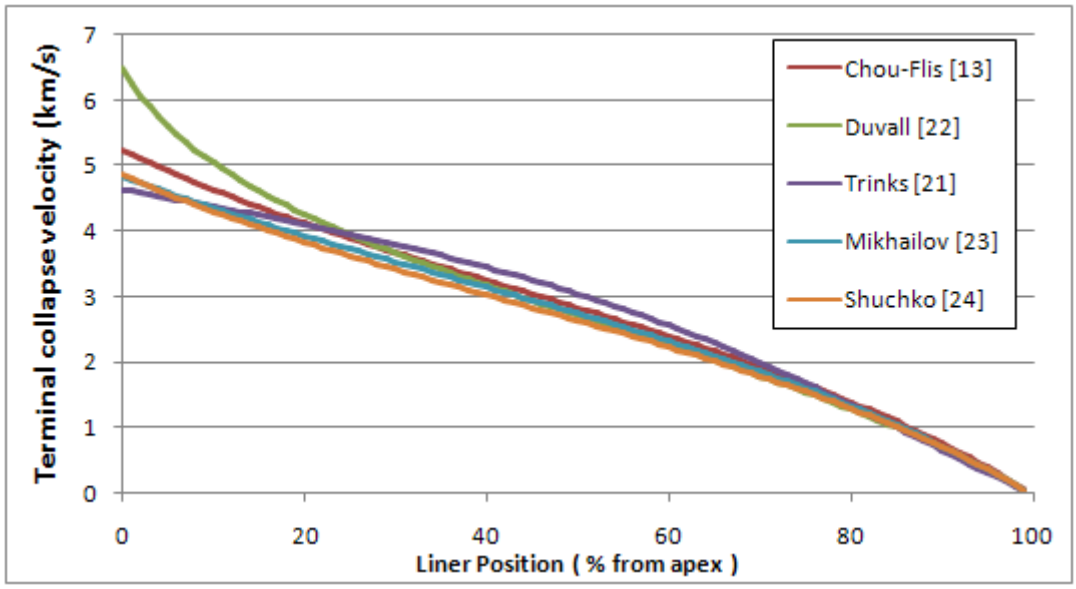

Figure 3-14 Comparison of terminal collapse velocities calculated by different models

Note that the collapse velocities given in Figure 3-14 are not the velocities at the moment liner elements reach the symmetry axis. These collapse velocities are calculated under the assumption of all liner elements have sufficient flight distance before reaching the axis, and therefore reach their maximum achievable velocity, known as the terminal collapse velocity. Velocities of the liner elements that can not reach their terminal collapse velocity before collapsing on the symmetry axis can only be calculated using an appropriate acceleration model. Since collapse velocity V_0 is used as an input to the calculation of the deflection angle δ, collapse angle β and the terminal velocity, it affects the whole solution directly.

Also note that, none of the V_0 calculation models take the casing into account. However it is known that amount of confinement due to casing affects the metal acceleration process. Indeed, confinement ratio can be neglected for the regions where μ is small, namely the charge to metal mass ratio is high, like in the apex region of the cone. However for the regions where the explosive thickness gets smaller, confinement effect is promoted, like in the base region of the cone. It is

known that confined explosives have a greater ability to accelerate metals. The confinement effect is discussed in more detail further in the text.

When detonation wave sweeps across the jet element, it can not reach its maximum velocity instantaneously. The acceleration can either be taken as constant, or an exponential acceleration can be used. The exponential acceleration is defined by Equation 2.7. According to Equation 2.8 the time constant that appears in Equation 2-7 depends on the Chapman-Jouget pressure of the explosive, liner mass per unit area and the collapse velocity. In this equation, P_{cj} and liner mass per unit area are constants for a constant thickness liner. It can be concluded that the time constant is a linear function of collapse velocity. Also it can be said that the time constant is a function of explosive type, since P_{cj} is different for different types of explosives. However, the constants C_1 and C_2 are problem dependent and must be determined by either finite element simulations or experiments. In this study, these constants are determined by AUTODYN-Jetting simulations. In the jetting option of AUTODYN liner is modeled as shell elements. The explosive and remaining parts of the problem are modeled using the Euler solver. After the explosive is detonated and hydrodynamic calculations are made, the shell liner elements are accelerated by using solver coupling. To measure the acceleration of individual liner elements, 20 gauge points are located on the liner, as shown in Figure 3-15. These gauge points are of moving type so that they move together with the liner material. Using these gauge points selected variables can be recorded at selected time increments. By recording velocity of the gauge points at small time steps, the acceleration of the liner elements can be tracked.

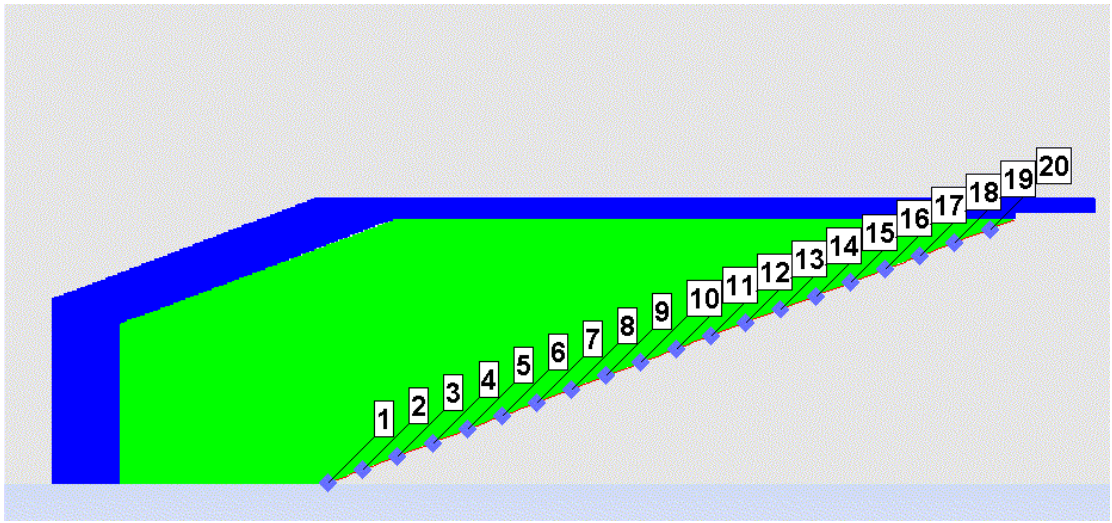

Figure 3-15 Location of moving type gauge points used in AUTODYN-Jetting simulations

Applying curve fitting to Equation 2.8 using the data from 20 gauge points, acceleration time constant τ for each gauge point can be calculated. Also using the terminal velocity V_0 obtained from AUTODYN-Jetting calculations, constants C_1 and C_2 can be determined. Till this point, only the individual time constants for each gauge points are known. Knowing all time constants for each gauge point, constants of Equation 2.8 can be calculated. In Table 3-7 time constants calculated for each gauge point are given. Note that the last two gauge points are excluded since they are not included in the jetting calculations, as advised in the AUTODYN-Jetting manual because of the limited explosive presence at the base of the cone. Also the first two data points are excluded since AUTODYN-Jetting calculations do not calculate jetting data for these points, because they are too close to the axis. The change of velocity with respect to time for gauge point 5 is given in Figure 3-16.

Table 3-7 Time constants calculated for each gauge point

Gauge No.	$\tau\ (s)$	$V_0\ (m/s)$		Gauge No.	$\tau\ (s)$	$V_0\ (m/s)$
3	502.28	1568.8		11	392.42	2716.4
4	623.17	1838.9		12	402.26	2651.0
5	611.53	2050.6		13	426.92	2562.6
6	539.58	2225.3		14	460.77	2447.2
7	495.13	2381.1		15	515.24	2297.5
8	459.77	2505.7		16	570.40	2132.8
9	432.36	2633.1		17	641.87	1934.6
10	403.75	2703.2		18	676.52	1706.3

Applying curve fitting to Equation 2.8 using the data given in Table 3-7 constants C_1 and C_2 are found as $-539.8 * 10^6$ and 1180, respectively. Using these values, Equation 2.8 for the particular problem of interest becomes

$$\tau = -539.8 * 10^6 \frac{MV_0}{P_{cj}} + 1180 \tag{3.1}$$

Substituting the known values for P_{cj} (34.2x10^9 Pa) and M (18.245 kg/m^2) this equation simplifies to

$$\tau = -0.288V_0 + 1180 \tag{3.2}$$

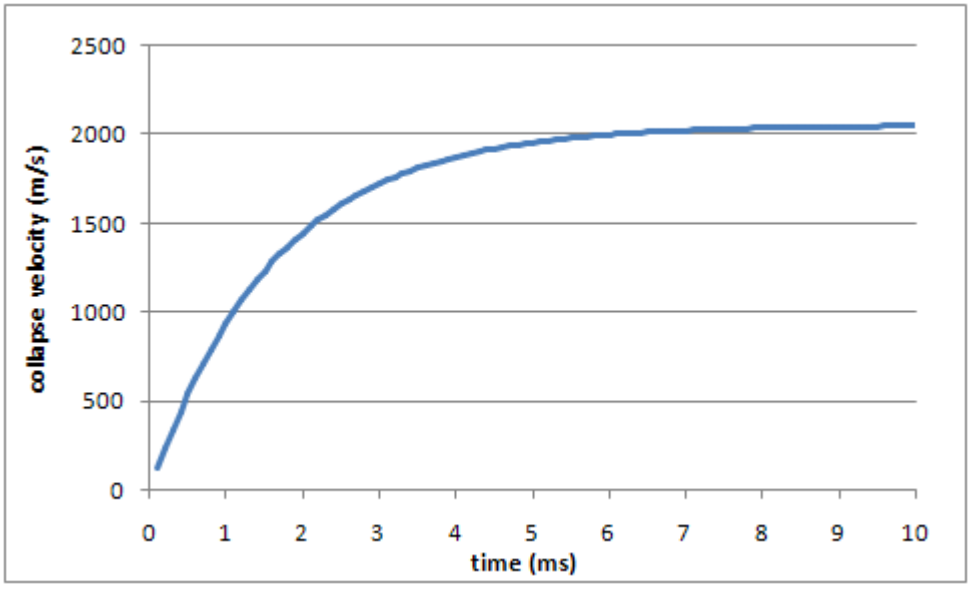

Figure 3-16 The change of collapse velocity with respect to time, for gauge number 5

The root of Equation 3.2 can be calculated as V_0=4097 m/s by equating τ to zero. This means for V_0 values larger than 4097 m/s there is no appropriate solution for τ. However, maximum collapse velocity is calculated approximately as 4800 m/s by the analytical model, which will be discussed further in the text. The reason why calculated maximum velocity by analytical model is out of the solution range of Equation 3.2 is that the collapse velocities calculated by AUTODYN-Jetting model are lower than those calculated by the analytical model. Eventually, and unfortunately, Equation 3.2 can not be used directly in the analytical model, rather is serves as a first estimation for time constant τ.

Since it is not possible to use Equation 3.2 in analytic jet formation calculations, a single time constant should be considered. Time constant values given in Table 3-7 are used to calculate an average time constant. The calculated average time constant is 510 s in this case.

In Figure 3-17, terminal collapse velocity and collapse velocity of the liner elements are given. Collapse velocities obtained by the analytical model, AUTODYN jetting calculations and data given by Walters and Zukas are compared in Figure 3-18.

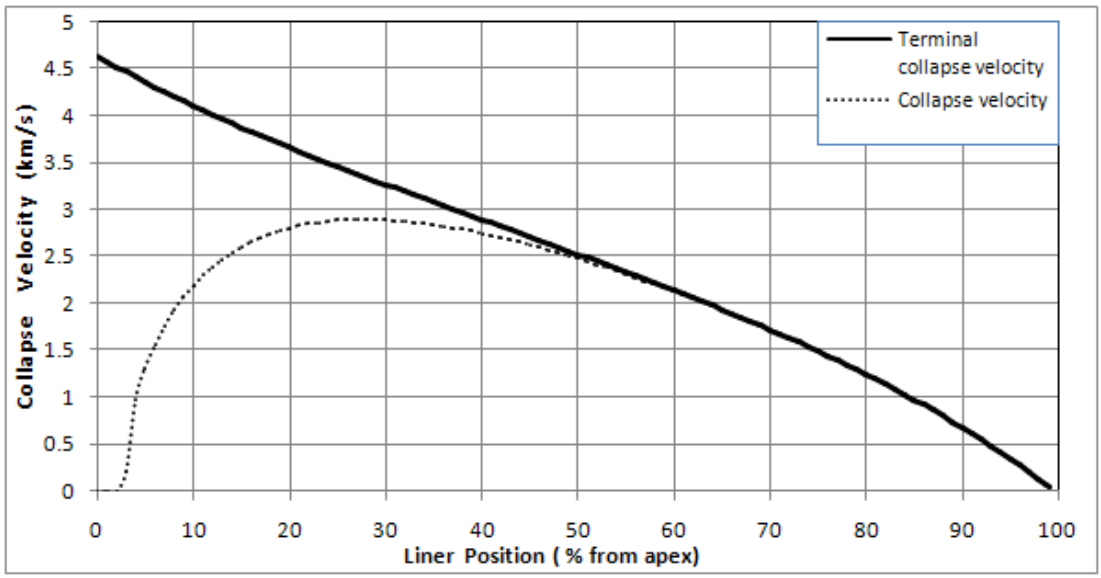

Figure 3-17 Change of collapse velocities with respect to liner position, with and without terminal velocity correction

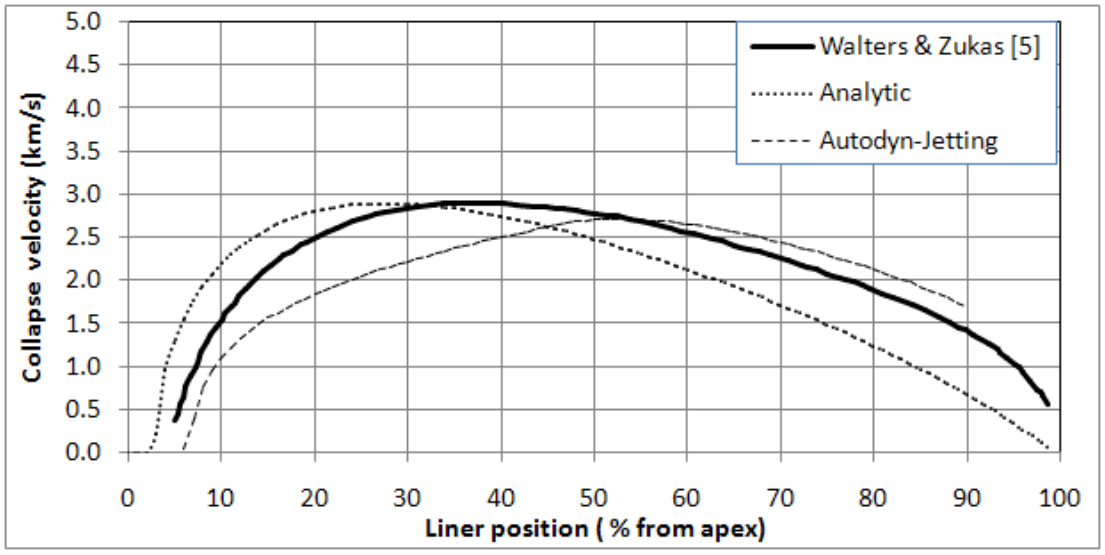

Figure 3-18 Comparison of collapse velocity profiles for different calculation models

Note that the data given by Walters and Zukas are for a BRL-82 charge of liner thickness 1.9 mm, whereas our BRL-82 has a liner thickness of 2.05 mm. It is seen that analytical calculations predict almost the same maximum collapse velocity with the data given by Walters and Zukas. However, the calculated collapse velocity seems to be shifted towards cone apex. The first possible reason of this shift is expected to be the different liner thicknesses used in the reference and in this study. The use of a thinner liner thickness in the reference is expected to provide higher terminal collapse velocities. Maximum point of the collapse velocity is expected to shift towards the base, since liner elements require more distance to reach higher terminal collapse velocities.

The second possible reason is the use of a curved cone apex with a radius of 17.5 mm instead of a pointed apex (see Figure 1-3). It is not clear if Walters and Zukas also used such a model or not. In the analytical study the liner is assumed to be a cone without apex radius. The effect of apex radius on the calculations can not be estimated without further work.

The accuracy of the analytical collapse velocity calculation depends on the selected collapse velocity and acceleration models. The parameters affecting the collapse velocity must be investigated in two separate regions. The first region is the upper part of the cone, from apex to cone middle height, which will be referred as the apex zone. The second zone is the lower part of the cone, from middle height to base, which will be referred as base zone.

In apex zone of a warhead with cylindrical casing, the explosive to metal ratio is high and casing effects can be neglected. In the apex zone time constant has the greatest influence on the collapse velocity. As pointed out before, an average value of time constant is calculated to be used in the analytical jet formation calculations. Collapse velocities calculated using this average time constant and two other values are given in Figure 3-19. As seen in this figure, calculated average time constant of $\tau = 510\ s$ provides almost the same maximum collapse velocity as given by Walters and Zukas [5].

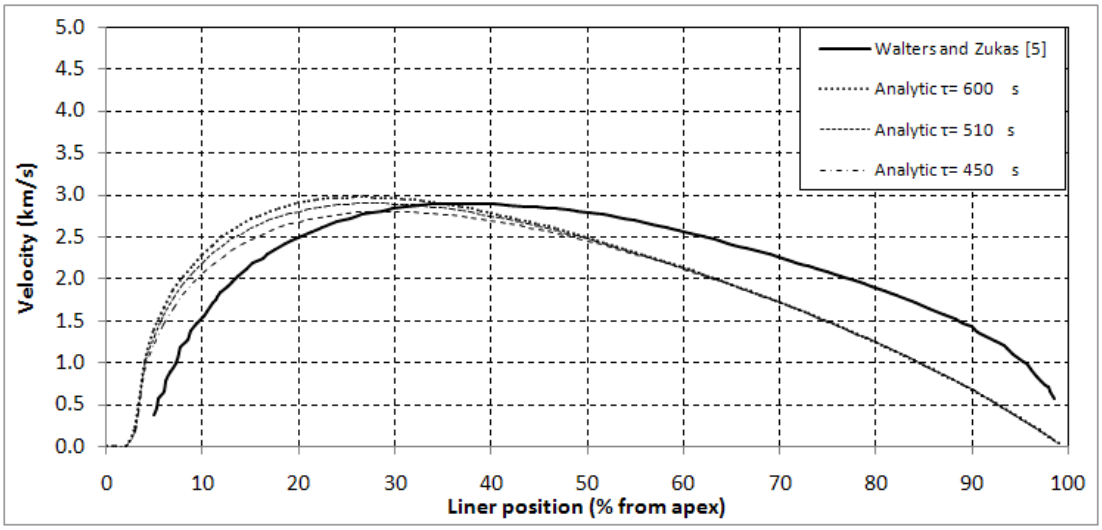

Figure 3-19 Comparison of collapse velocity profiles for different average time constant

In the base zone, as seen in Figure 3-18, both calculations of AUTODYN-Jetting and data given by Walters and Zukas yield a higher collapse velocity than the one calculated by the analytical model. It is stated earlier that, none of the metal acceleration models takes the confinement effects into account. In Figure 3-20 AUTODYN-Jetting results of the simulations with and without casing are presented. It is seen that, in the base zone the confinement has an effect on collapse velocity. Without confinement, collapse velocities are lower in the base region. As the confinement to charge mass ratio increases towards the base, the effect of confinement increases. This can be accepted as a possible reason of the differences between analytical model solutions with the data of Walters and Zukas, in the base region of the cone.

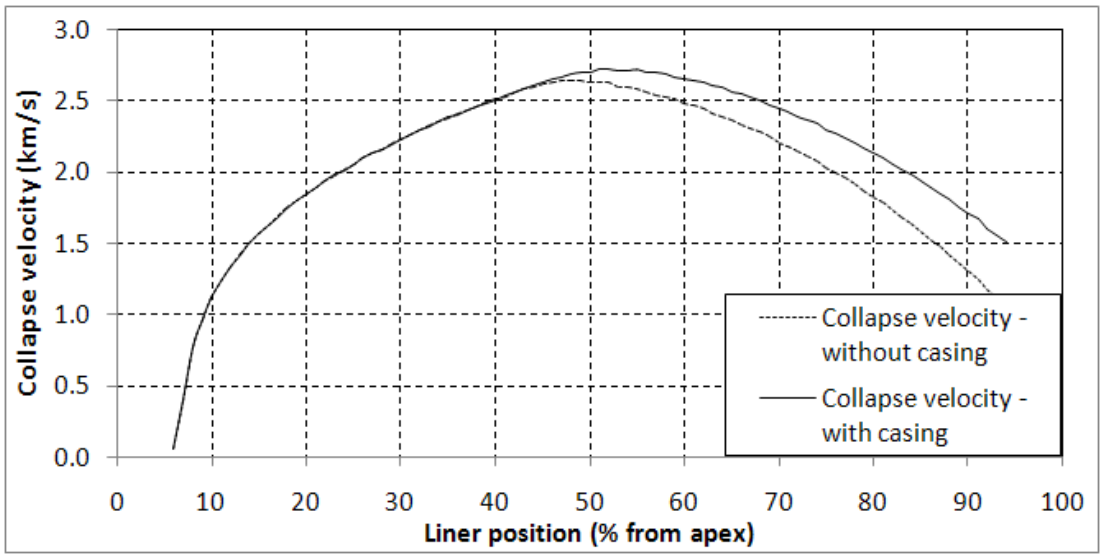

Figure 3-20 Comparison of collapse velocity profiles with and without casing obtained by AUTODYN-Jetting simulations

For a better agreement with other results, analytical calculations can make use of a correction factor to simulate the effect of casing. To account for confinement effects in the base zone, an equivalent explosive thickness can be calculated to increase calculated collapse velocity as a function of charge to metal ratio. Another possibility is to use a collapse velocity model that directly takes the confinement effects into account. Although researchers mention about such models, their numerical constants are not provided and therefore these models can not be used in the current study.

3.2.2 Collapse angle

After the acceleration calculation of the jet is complete, deflection angle A and collapse angle β are calculated by Equations 2.11 and 2.12, respectively. Deflection angle affects the collapse position of a liner element on the symmetry axis, whereas collapse angle affects the jet velocity and mass. Note that as the collapse angle β increases, jet velocity decreases but the amount of liner material entering jet

formation increases. The comparison of the collapse angle β and the steady state collapse angle β^+ is given in Figure 3-21.

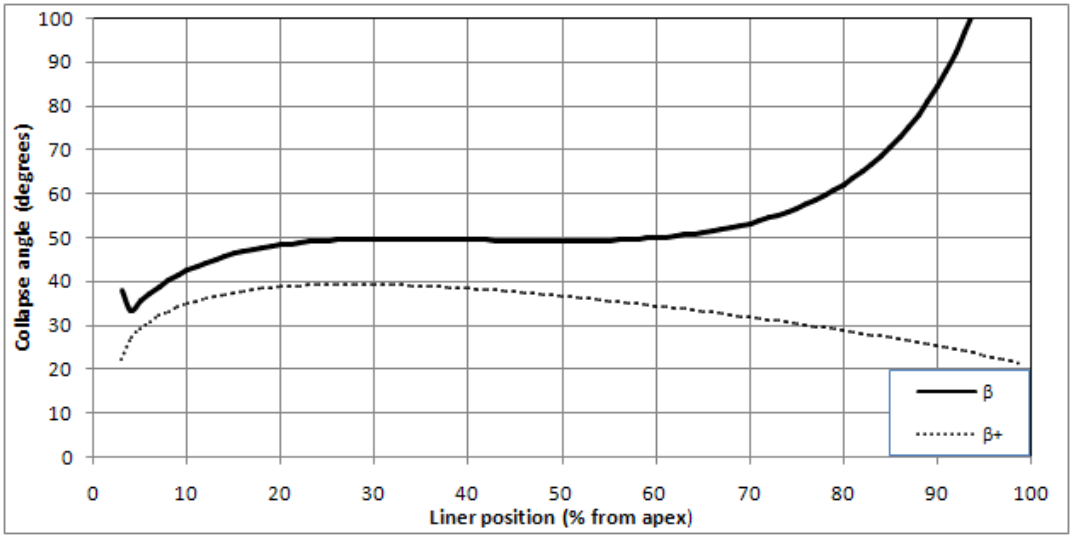

Figure 3-21 Comparison of steady-state (β) and corrected (β^+) collapse angles

Figure 3-22 provides a comparison of the collapse angle β calculated analytically with AUTODYN-Jetting results and the data given by Walters and Zukas [5]. Analytical calculations predict the general behavior of collapse angle well, however there is a disagreement with the results of Walters and Zukas especially in the middle sections of the cone. Possible reason is the difference between the analytically calculated collapse velocity and data by Walters and Zukas (see Figure 3-18). The disagreement between AUTODYN-Jetting results and data by Walters is larger, in comparison with analytical results. One of the reasons is again the difference between collapse velocities. However, it since the details of the AUTODYN-Jetting calculations are not known, the main reason of disagreement in collapse angle can not be known. Another possibility of disagreement of both analytical and AUTODYN-Jetting calculations is the liner thickness difference between charges used the current work and by Walters and Zukas. However, this difference can not be cleared out without further study using different liner thicknesses.

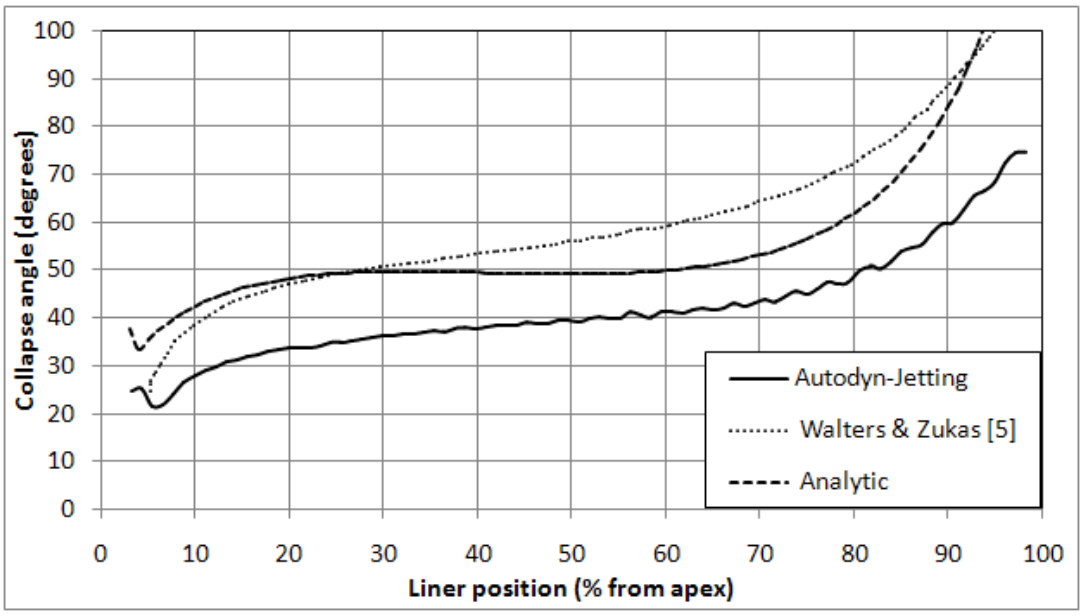

Figure 3-22 Comparison of collapse angle calculated by different models

3.2.3 Jet Velocity

In the previous sections, collapse velocity V_0, deflection angle A and collapse angle β are calculated. Knowing these variables, it is possible to calculate jet velocity using Equation 2.16a. Jet velocity calculated by the analytical model is given in Figure 3-23.

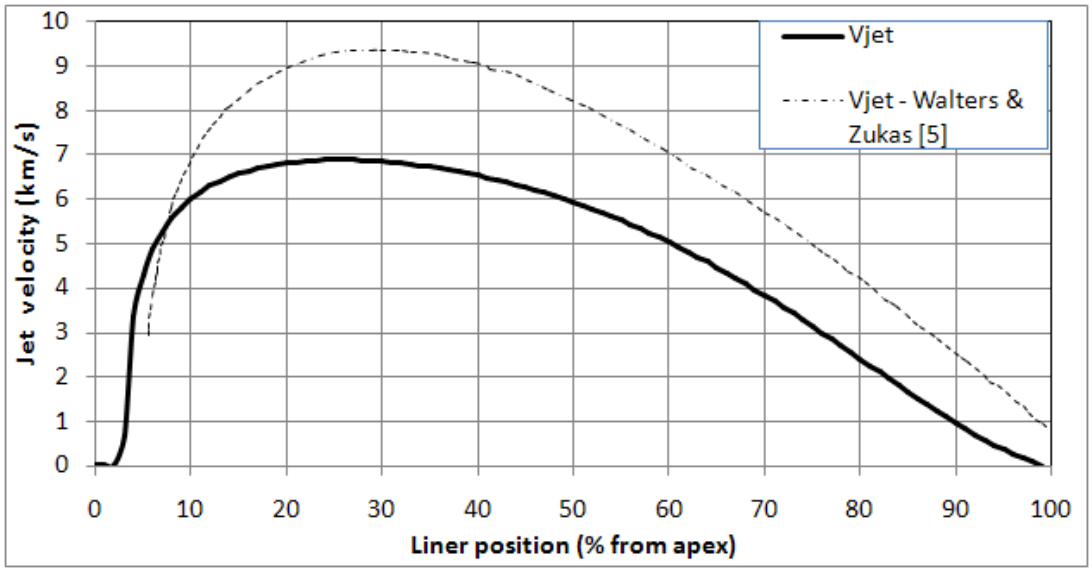

Figure 3-23 Change of jet velocities along liner position

Maximum jet velocity calculated by the analytical model is 22 % lower than the experimental value given by Walters and Zukas [5]. A possible explanation of this difference is given by Chanteret, which is based on an alternative collapse angle calculation [14]. In classical PER theory, collapse angle is calculated by Equations 2.11 and 2.12, as stated before. In his paper, Chanteret stated that collapse angle can alternatively be calculated by the geometrical relation between collapse velocity, flow velocity and the stagnation point velocity (see Figure 2-3) as follows,

$$\tan(\beta) = \frac{\cos(\alpha + \delta)}{\frac{V_{cl}}{V_0} - \sin(\alpha + \delta)} \tag{3.3}$$

According to this relationship, collapse angle can be revised and new jet velocities can be calculated using Equation 2.16a. New jet velocity results can be seen in Figure 3-24.

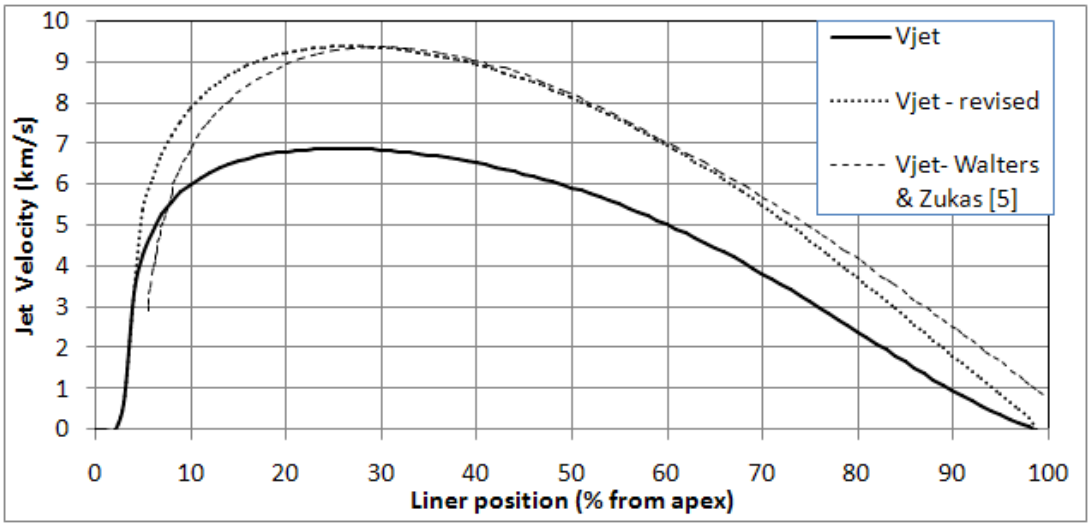

Figure 3-24 Comparison of jet velocity with and without the revision of collapse angle

As seen in Figure 3-24, jet elements originating from the apex region of the cone have lower velocities, up to 20 % height of the cone. The main reason of this is that, liner elements near the apex collide on the axis before reaching their final collapse velocity, as mentioned earlier. Since the jet elements collapsing earlier have lower velocities compared to elements collapsing later an inverse velocity gradient is generated. This results in collision and coalescence of the jet elements in the inverse velocity zone. Coalescence of the jet elements cause pile-up of mass in the tip region, which is already called as jet tip. Jet tip has a larger radius and mass than the following jet elements. The coalescence of the slower jet elements in the front with the faster particles behind results in degradation of velocity of the faster particles and a lower maximum jet tip velocity. However since the elements close to the cone apex have smaller masses because of the small cone radius compared to base of the cone, the resultant jet velocity is close to the maximum velocity in the collapse calculations.

The tip velocity can be calculated using Equation 2.17 which is simply a calculation using momentum balance. Perfectly plastic collision is assumed between jet elements

in the jet tip formation. The jet velocity corrected for jet tip formation is given in Figure 3-25. Figure 3-26 shows the comparison of final jet velocity determined using analytical and AUTODYN-Jetting calculations and data given by Walters and Zukas [5]. Also, in Table 3-8 tip velocities and the ratio of height of the last liner element joined in jet tip is given.

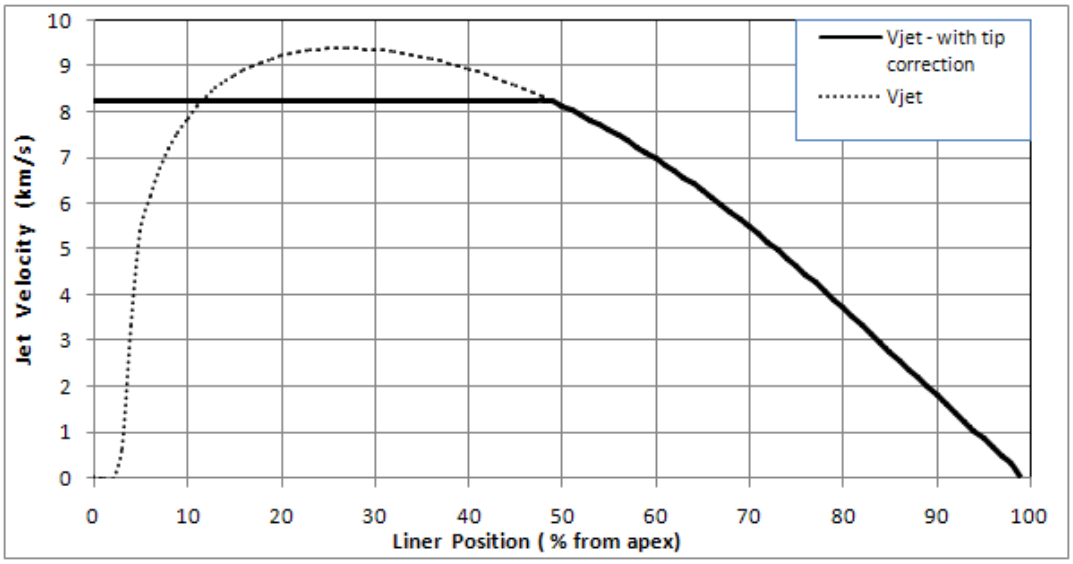

Figure 3-25 Jet velocity profile along liner, with and without tip correction

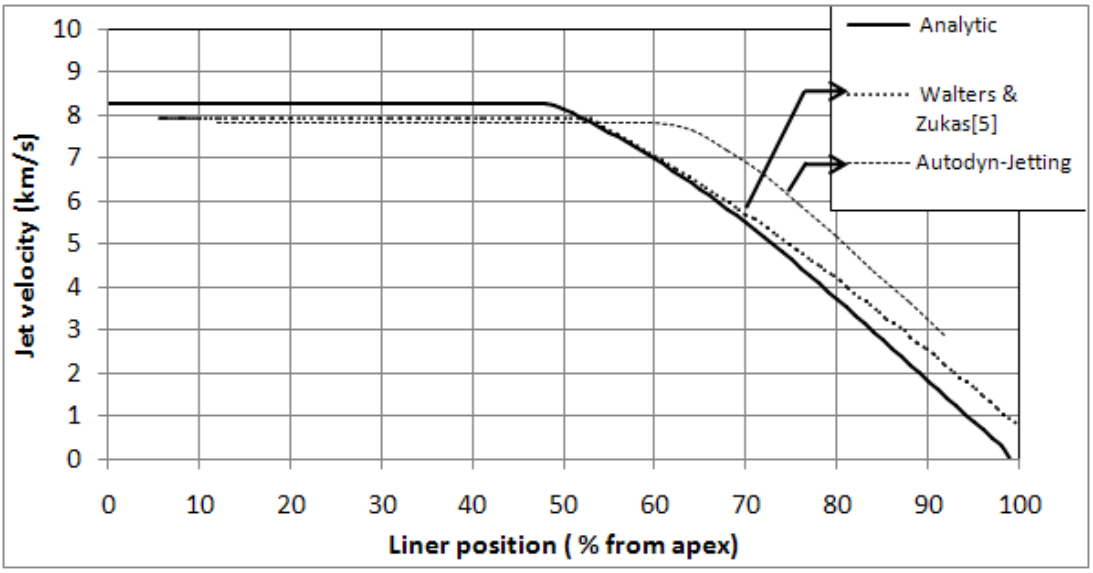

Figure 3-26 Comparison of jet velocities by different calculation models

Table 3-8 Comparison of tip velocity and tip position

	Tip velocity (m/s)	Tip position (% from apex)
Analytic	8261	48
AUTODYN-Jetting	7810	68
Walters and Zukas [5]	7930	51
Bolstad & Mandell [3]	8300	-

Figure 3-27 gives the comparison of cumulative jet mass with respect to velocity. As seen from the figure, cumulative jet mass for analytical calculations is lower than both AUTODYN-Jetting results and the data of Walters and Zukas. The reason is that, after Chanteret's correction, the calculated collapse angle is lower in analytical calculations. Lower collapse angle results in lower jet mass. Also it is seen that AUTODYN-Jetting simulation results in highest jet mass of all three results. The reason for this is not known, since the algorithm behind the simulations is not known clearly.

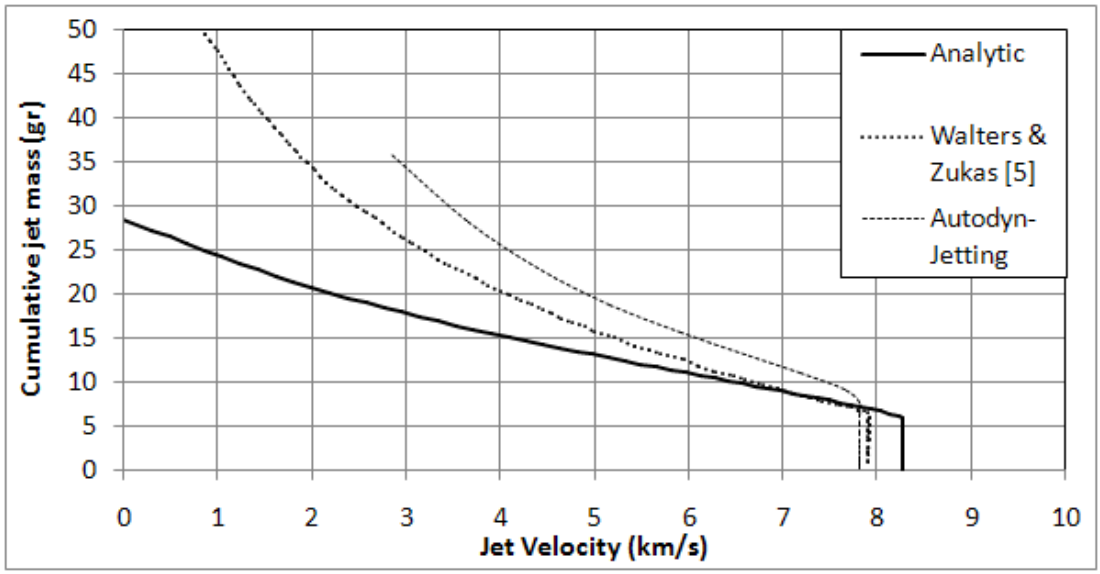

Figure 3-27 Comparison of calculated cumulative jet mass with available data

In Figure 3-28 analytically calculated jet radius is compared with the AUTODYN-Euler jet formation simulations. Distance is measured from the rearmost point of the slug. Region of the jet, having velocity over 3000 m/s is shown, as it is used in the penetration calculations and discussed further in the text. It is seen that, analytical calculations are predicting jet radius lower than AUTODYN Euler solutions. This is expected because lower jet mass obtained by the analytical calculations result in smaller jet radius.

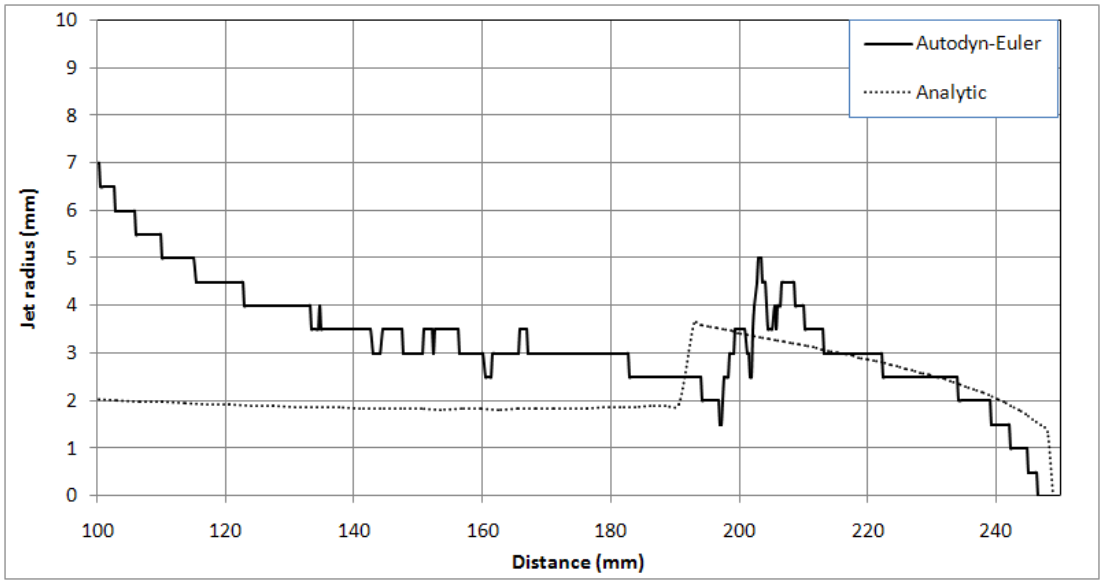

Figure 3-28 Jet radius calculated by AUTODYN-Euler simulation and analytic model

3.3 Discussion on Jet Formation Analysis

In this chapter, numerical simulation and analytical calculation methods for the jet formation are discussed. Parameters that affect the numerical jet formation simulations using AUTODYN-Euler solver are investigated. Also, jetting option in

AUTODYN-Euler solver is used as an alternative. Results of the analytical jet formation calculations are compared with the numerical simulations and the available data in the literature.

In the first set of studies, mesh sensitivity of the jet formation problem in the numerical simulations are investigated. It is shown that, as the cell size tends to zero, jet tip velocity approaches to 8800 m/s, compared to the experimentally measured value of 8300 m/s [3]. It can be concluded that, cell size of 0.25 mm is sufficient to simulate shaped charge jet formation, since it shows a good agreement with the experimental data. Also, it is practical to be computed on a workstation of single core 3.2 GHz CPU and 1 GB RAM with a computational time of approximately 20 hours. Simulation with mesh size of 0.125 mm requires 1.1 GB of RAM during computation; so an eight core 3.2 GHz CPU server with 16 GB RAM is used. Total computational time is 4 days in this case. Note that, mesh size must be considered in accordance with the smallest dimension involved in the problem. In a shaped charge analysis, liner thickness is considered to be the most critical smallest dimension. It this case, the ratio of the liner thickness to the mesh size is almost 8 for 0.25 mm mesh size, meaning 8 elements are present along the thickness of the liner.

In the next step, the possibility of improvement for computational resource and computational time requirement is investigated. Simulations are performed using cells of aspect ratios up to 2, 4, and 8. It is shown that, jet tip velocity is decreasing with increasing aspect ratio. However, the amount of decrease in the jet tip velocity is limited so that it leads to acceptable simulation errors for most practical purposes. The difference in jet tip velocity is increasing with increasing aspect ratio and standoff in comparison with simulations using cells of unity aspect ratio. The variables are cell centered in AUTODYN-Euler simulations and if the centerline velocity distribution will be used in further calculations, data resolution is reduced with increasing cell size since velocity is considered to be constant along each cell.

To speed up calculations and ease the modeling process, the same jet formation model is simulated with both air and void as the surrounding medium. It is shown that, simulation without air has a very limited effect on jet velocity for short standoff

distances, which can be disregarded for most practical purposes. Also both simulation time and memory requirement is higher for simulations with air, since all cells with material have a data to be stored and processed. In the simulation with air, it is calculated that jet tip velocity is decreasing with a linear rate of 36.45 m/s per CD standoff distance; that may be attained to air drag. However, it is thought that this observation needs further investigation and experimental study.

An analytical code is developed to analyze shaped charge jet formation process. In the analytical code, PER theory is used for liner acceleration. The unknown constants for the exponential acceleration formula (Equation 2.8) are calculated using the results of AUTODYN-Jetting simulations. Substitution of calculated constants in Equation 2.8 results in Equation 3.2. Although a good fit of data from simulations is obtained, the maximum velocity calculated by analytical models is out of the solution range of Equation 3.2. The reason is that, the collapse velocities calculated by AUTODYN-Jetting model is lower than that calculated by analytical model. As a result; a single constant time constant is used for all liner elements, rather than variable time constant. This value is taken to be the average of time constants calculated for all elements in AUTODYN-Jetting simulations. Using this average time constant, terminal collapse velocities show a good agreement with the data given in Walters and Zukas [5]. A more detailed numerical simulation study is needed to further investigate the acceleration behavior of the shaped charge liner. In this study, planar type of explosive-liner problem geometries may be used; since Equation 2.8 is not limited to cone type of geometries. By this way, liner elements will be allowed to reach their final velocities, without collapsing to the symmetry axis.

The effect of changing time constant on collapse velocity is also investigated. It is shown that with decreasing time constant, maximum collapse velocity throughout liner elements decrease. Also maximum collapse velocity point shifts towards the base of the cone. The reason is that, as time constant decreases, liner elements require more time to reach their terminal collapse velocities.

It is observed that, although maximum collapse velocity shows a good agreement with the data given in Walters and Zukas, maximum velocity point is different and collapse velocities are lower in the base region of the cone. The possible reason is that, liner acceleration models do not take the effect of casing into account. Also the results of AUTODYN-Jetting simulations with and without casing show that collapse velocity in the base region of the cone is higher in the case with casing. An equivalent explosive thickness can be calculated to take the casing effect into account. A more detailed numerical simulation study is also needed, as it is suggested for liner acceleration behavior. Different confinement thicknesses may be used in the same study to investigate effect of confinement on liner collapse velocity. Also collapse velocity models that make use of casing effect may be used.

After the collapse velocity is calculated, deflection angle and collapse angle are calculated. The results of AUTODYN-Jetting calculations for collapse angle are lower, compared to data given by Walters and Zukas [5]. Analytical jet formation model predicts almost the same behavior for collapse angle however the differences are on the order of 10 degrees in the upper middle region of the cone. One possible reason is the use of planar detonation wave assumption. This means initiation point is not taken into account, and angle of incidence is the same for all liner elements. If generalized PER theory is used, which takes initiation point into account, a better agreement with the available experimental results can be achieved for collapse angle. Note that Chou-Flis liner collapse velocity formula (Equation 2.3) is used in analytical calculations. If another collapse velocity formula is used, a different collapse angle distribution may be obtained along the cone height. The reason is that, both collapse velocity and the derivative of the collapse velocity is used in the calculation of collapse angle.

The jet velocity is calculated, knowing collapse velocity, deflection and collapse angles. However, the jet velocity is lower compared to experimental data given by Bolstad and Mandell and Walters and Zukas [3, 5]. After applying Chanteret's correction for collapse angle [14], the jet velocity calculated by analytical model shows a good agreement with Walters and Zukas [5].

After jet velocity profile is calculated throughout the cone, jet tip correction is applied, as a treatment to the inverse velocity gradient in the jet. After the jet tip correction tip velocity of the jet is found to be 8261 m/s. The tip velocity is stated to be 8300 m/s by Bolstad and Mandell and 7930 m/s by Walters and Zukas [3, 5]. Jet tip correction is also applied to the results of AUTODYN-Jetting calculations and the tip velocity is found to be 7810 m/s. In the analytical jet formation calculations, a single constant velocity is calculated for the jet tip, assuming perfectly plastic collision between jet elements. Also jet tip is assumed to be fully formed before jet reaches the target. If the collisions of the jet elements are calculated depending on time, a velocity distribution can be achieved in the jet tip. As a result there remains no need for assuming a single constant jet tip velocity.

Cumulative jet mass with respect to jet velocity calculated by analytic jet formation model is compared with the results of AUTODYN-Jetting calculations and data given by Walters and Zukas [5]. The cumulative jet mass is lower in case of analytical jet formation model. The reason is that, after Chanteret's correction, the calculated collapse angle is lower in analytical calculations. Lower collapse angle results in lower jet mass. This is also observed when jet radius calculated by analytical jet formation model is compared with the AUTODYN-Euler simulations. It is shown that, jet radius calculated by analytical jet formation model is lower than that calculated in AUTODYN-Euler simulations throughout the jet. As a result of a lower jet radius, a lower penetration crater radius is expected, discussed further in the text. However the radius profile of jet tip shows a good agreement with the simulations.

CHAPTER 4

ANALYSIS OF BREAKUP TIME

As a general behavior, leading portions of the shaped charge jets are faster than lagging sections so that a velocity gradient exists on the jet. After liner collapse and jet formation, jet continuously elongates because of this velocity gradient and eventually breaks up. As the jet breaks up, individual jet particles tend to tumble and spread from the jet flight direction. Since leading jet particles create a penetration hole on the target, lagging jet particles should travel through this penetration hole to reach the base of the hole to create additional penetration. As the jet particles divert from the flight axis, some of them begin to interact with the penetration hole perimeters which reduces their penetration capability. Because of this reason, breakup time is an important parameter to define penetration performance of a shaped charge jet. A shaped charge jet with a larger breakup time is expected to have a greater penetration performance since the jet is allowed to elongate more. Optimum standoff distance for the penetration is also directly related to the breakup time.

As discussed in Section 2.2 there exist several models to calculate breakup time of shaped charge jets. But the jetting analysis should be carried out before performing the breakup analysis. As discussed in the previous chapter, in this thesis three different methods are used to calculate the jetting parameters. One of them is the analytical code that makes use of the formulas described in Section 2.2. The second method uses the Euler solver of the famous hydrocode AUTODYN. After

performing the jetting calculation, velocity and density data from AUTODYN Euler solution can be extracted to be used in breakup time and penetration calculations. By processing the extracted data, the geometrical shape of the jet can also be obtained. In the third method, "Jetting" option in AUTODYN-Euler solver is activated to obtain the jetting parameters.

The calculations performed with these three methods are compared with the experimental data given by Walters and Summers [15]. In this reference experimental breakup times of standard BRL-82 charge are given in three different ways, which are stated to be acquired by Flash x-ray photographs. The first one is called cumulative breakup time, which is calculated by dividing cumulative length of the jet by the velocity difference on the jet. The cumulative length can be found by summing up the length of all jet particles characterized in the experiment. The velocity difference is the difference between the fastest and the slowest characterized jet particle. Cumulative calculation begins and proceeds from tip to tail, from the first to the n^{th} particle.

In the second way, which is called individual breakup time, the measurements are performed similar to the first one; however breakup time of the individual jet particles are calculated instead of using a cumulative summation. The calculations use velocity differences between particles and lengths of the particles. However, it is stated that, separated particles move very close to each other after separation and this cause a scatter in the data. In the first two ways, the breakup time is calculated with respect to a virtual origin, the point which all particles is assumed to emanate at time zero.

In the third way, which is called separation time, breakup time is calculated by using the distance and velocity difference between particles. If the velocity difference is known between two particles, using the distance between them the time passed after the separation can be found. Separation time is not measured from the time at which jet element is formed (namely the virtual origin), rather it is measured with respect to

a different reference time. This reference time is taken to be the initiation of detonation [15].

4.1 Semi-empirical breakup formulas

As described in Section 2.2, V_{pl} breakup model includes calculation of plastic velocity V_{pl} by different methods to calculate the breakup time. This model is applied to both analytical calculation and AUTODYN-Jetting solutions. Using Equation 2.23 V_{pl} is calculated as 88.1 m/s, using liner thickness of 2.05 mm and charge diameter of 82 mm. After finding V_{pl}, breakup time can be calculated by using Equation 2.22.

Pfeffer model, relates breakup time with initial strain, initial strain rate and shock velocity in the jet. It assumes that the breakup time is independent of jet strength [15].

Carleone-Chou model relates the breakup time with initial strain rate, initial radius of jet and plastic wave speed C_p. This model is based on the experimental data for charges of size from 60 mm to 178 mm [5].

Chou described breakup time with simplified formulas using curve fitting to experimental data [13]. In his formulas, breakup time is not only related to the initial strain rate, initial radius and plastic velocity, but also to the radius of the jet and plastic velocity at any time after the virtual origin. The formulas are fitted to experimental data with the constant *k*, which has a suggested value of 5 (see Equation 2.27). Chou breakup time model is the only one that can be used with the jet data extracted from AUTODYN-Euler solutions because jet data is obtained at a time after the jet is formed. However, in other breakup models, jet data is needed at the moment of jet formation for each element.

Note that, information of individual breakup time for each jet element is enough to calculate penetration behavior of a jet, since penetration is also calculated on element basis, as discussed in the further chapters. Figure 4-1, 4-2, 4-3 and 4-4 show the individual breakup times calculated by V_{pl}, Pfeffer, Carleone-Chou and Chou models, in comparison with the data by Walters and Summers [15].

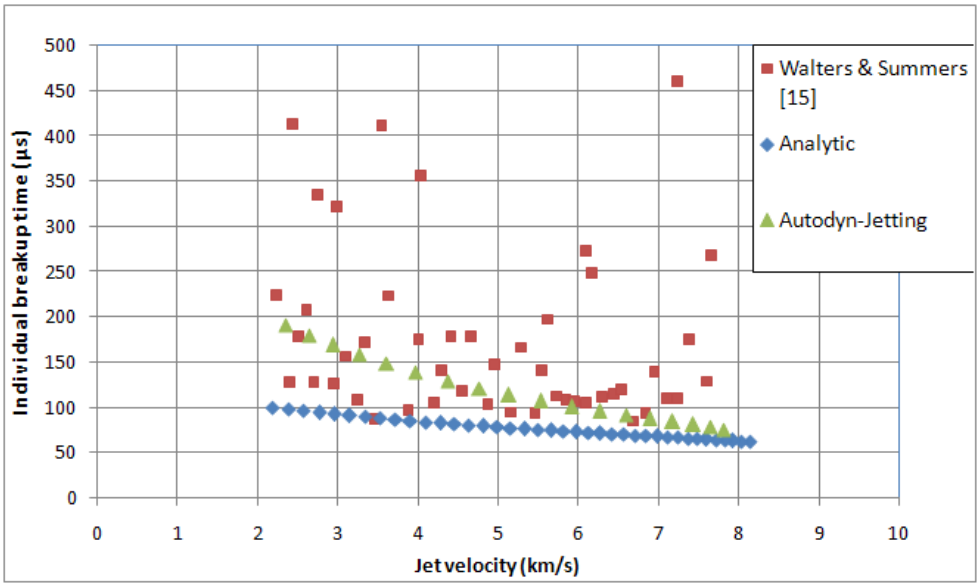

Figure 4-1 Comparison of the individual breakup times calculated using V_{pl} model

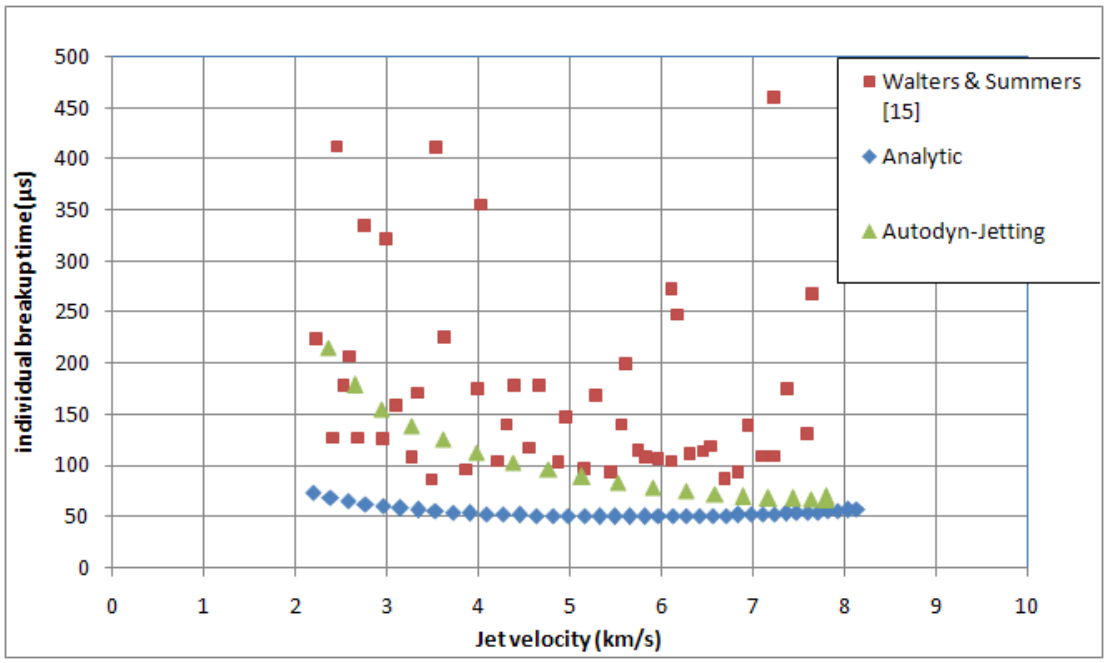

Figure 4-2 Comparison of the individual breakup times calculated using Pfeffer model

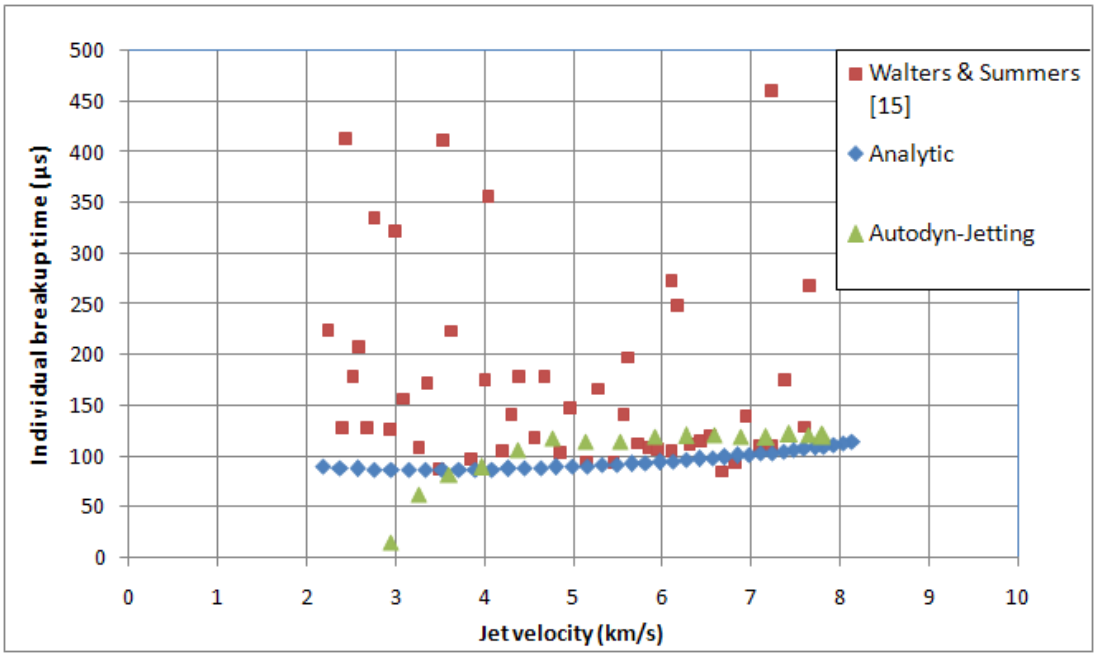

Figure 4-3 Comparison of the individual breakup times calculated using Carleone-Chou model

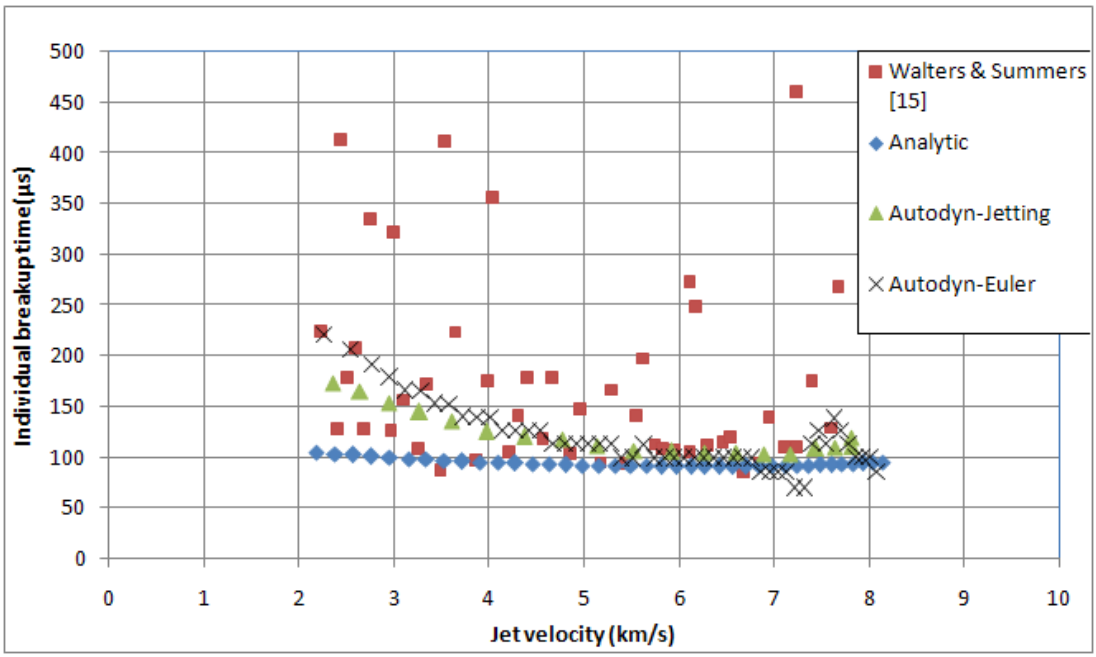

Figure 4-4 Comparison of the individual breakup times calculated using Chou model

As seen in Figure 4-1, 4-2, 4-3 and 4-4, all analytical breakup calculations that use analytical jetting model results as input (shown with blue diamonds) under breakup behavior compared to Walters and Summers [15]. Chou breakup model is the most accurate model. V_{pl} model predicts the breakup times for higher jet velocities better, whereas Carleone-Chou model provides a better prediction for lower jet velocities.

Breakup calculations that use AUTODYN-Jetting simulation results as input (shown with green triangles) show a good agreement with the experimental data given by Walters and Summers [15], except Carleone-Chou model. V_{pl}, Pfeffer and Chou models predict experimental data nicely for the lower jet velocity regions, and provide under predicted results for higher jet velocity regions. Carleone-Chou model properly predicts the individual breakup for jet velocities above 5 km/s however; it gives a reversed behavior at the rear portion of the jet with slower velocities. Main reason of this behavior is the strain values decreasing from tip to tail predicted by the AUTODYN-Jetting calculations; whereas the opposite behavior is expected. Note that, Chou breakup model shows an exceptional agreement with the experimental

data of Walters and Summers for jet velocities below 5 km/s. It also predicts higher velocity regions with an acceptable level of error.

Chou breakup time calculations, using AUTODYN-Euler simulation results as an input, shows a good agreement with the available experimental data, as seen in Figure 4-4. It under predicts experimental trend for higher velocity regions, and results in an under prediction in lower velocity regions. However, predictions are always in the close neighborhood of the experimental trend.

As seen in Figure 4-5, 4-6, 4-7 and 4-8, all breakup calculations using analytical jetting model results as input under predicts the breakup behavior compared to Walters and Summers, similar to the case of individual breakup times. Again, Chou model seem to provide the most accurate predictions for the separation times. Results of Carleone-Chou model show a good agreement especially for the higher velocity regions. However, the difference between calculations and available experimental data increases towards lower jet velocity regions. V_{pl} model seems to have a constant under prediction. Pfeffer model, on the other hand, does not agree with the available experimental data.

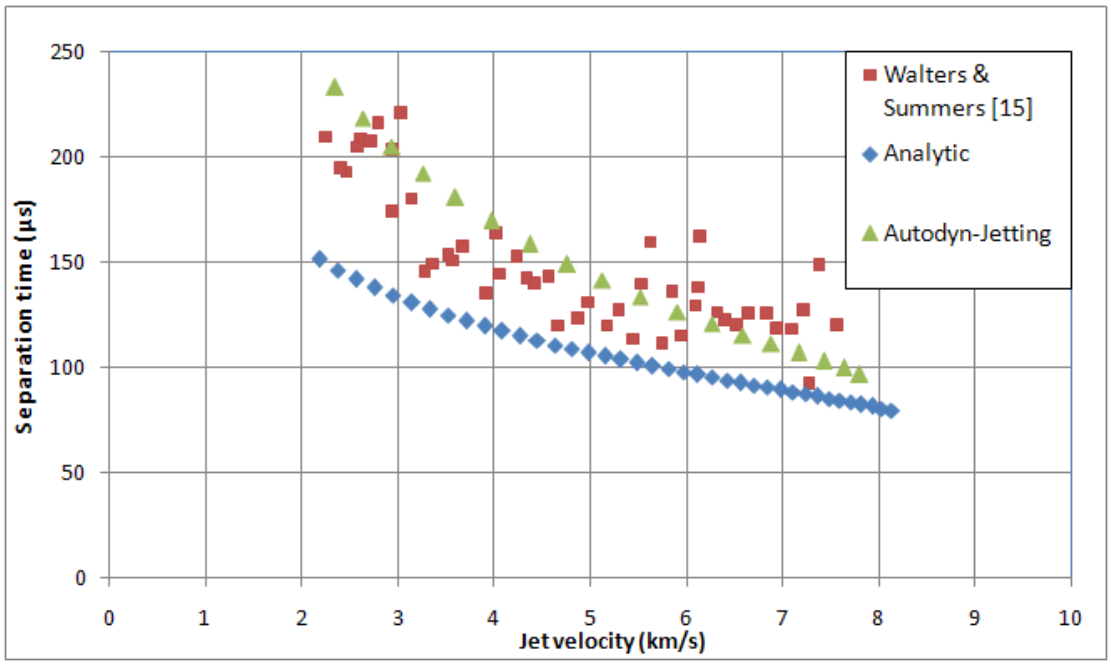

Figure 4-5 Comparison of the separation times calculated using V_{pl} model

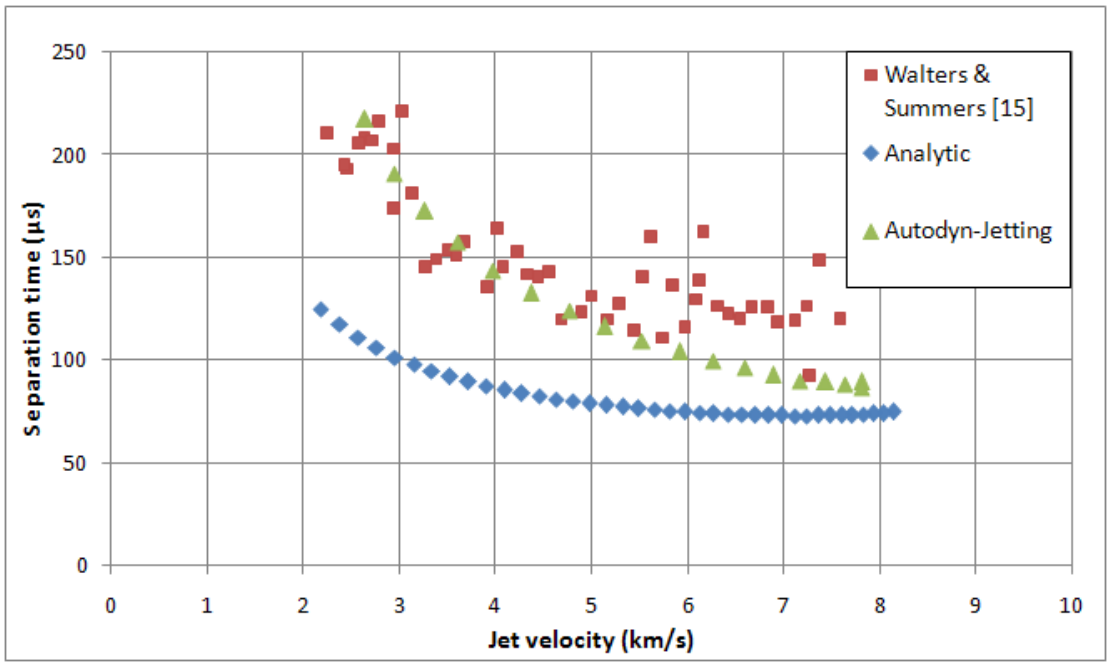

Figure 4-6 Comparison of the separation times calculated using Pfeffer model

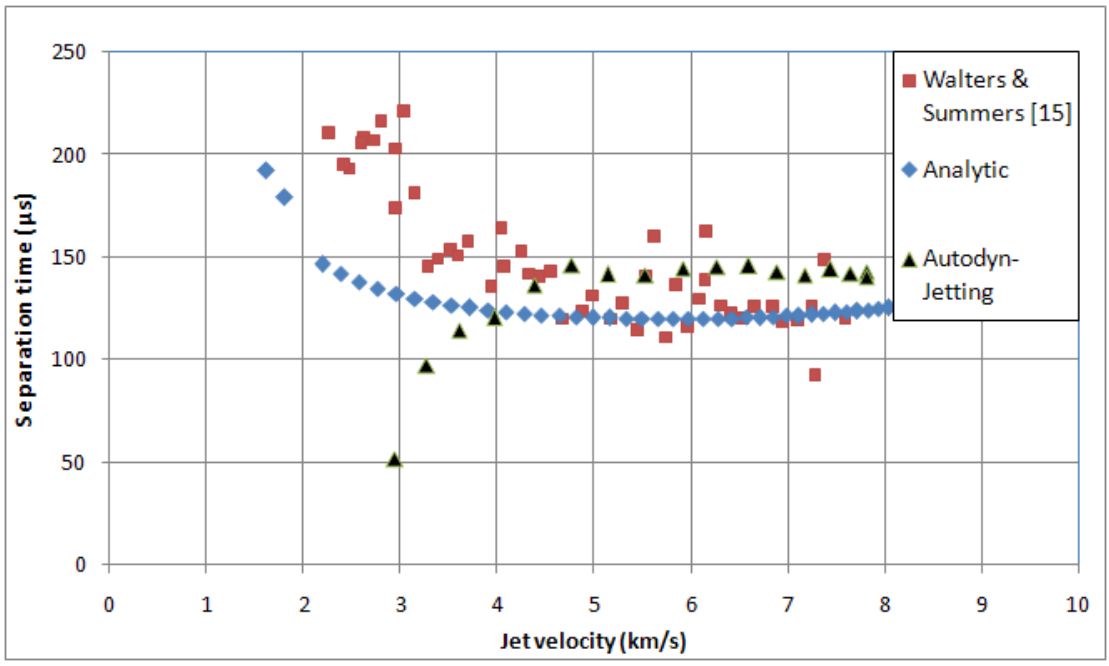

Figure 4-7 Comparison of the separation times calculated using Carleone-Chou model

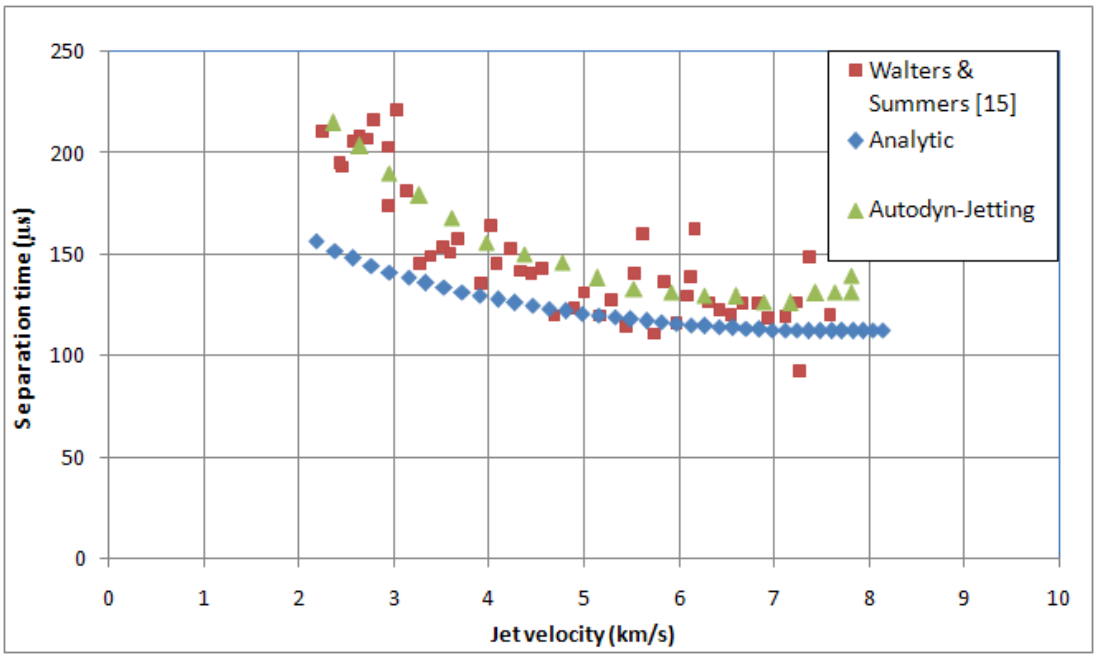

Figure 4-8 Comparison of the separation times calculated using Chou model

Separation time calculations, that use AUTODYN-Jetting simulation results as input, show a good agreement with the experimental data. Once again, Chou model seem to be the most accurate one. V_{pl} model also shows a good agreement with the experimental data. Pfeffer model provide proper predictions for jet velocities higher than 5 km/s, although it results in an under prediction in higher velocity regions. Results of Carleone-Chou model does not agree with the available experimental data, because of the unexpected behavior of strain rate calculated for the jet, as discussed before.

Note that, separation times for AUTODYN-Euler simulations can not be calculated. The reason is that, for separation time to be calculated, the detonation wave arrival time measured from the explosive initiation time need to be known for each liner element. In the Euler solver, calculations are not performed on element basis, so that even if the detonation arrival for an element is known, this element can not be tracked further in the simulation.

It is known that, V_{pl} breakup model can be used to calculate breakup time, if V_{pl} value is determined experimentally. To investigate the effect of it on breakup time, calculations are repeated for different values of V_{pl}. Figure 4-9 shows the dependency of individual breakup time on V_{pl}, as given by Equation 2-2. Figure 4-10 is a similar one for the separation time. According to these figures, lower V_{pl} values seem to agree better with the available experimental data for both individual breakup and separation times. It seems that a V_{pl} value of 60 m/s could predict experimental values best. Here it is worth to remember that the V_{pl} value is calculated as 88.1 m/s using Equation 2-23. Knowing that V_{pl} has an attributed physical meaning of velocity difference between successive jet segments, higher V_{pl} values lead to less jet segments but lower breakup times according to Figure 4-10. Conversely, lower V_{pl} values lead to more jet segments, but a higher breakup time.

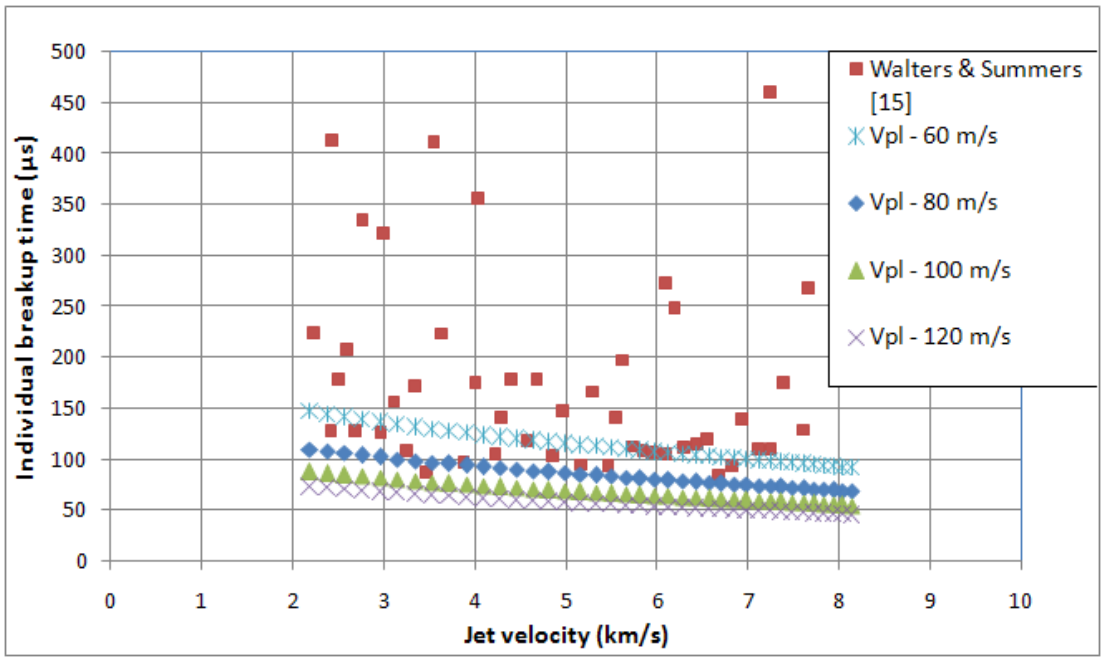

Figure 4-9 Change of individual breakup time with V_{pl}

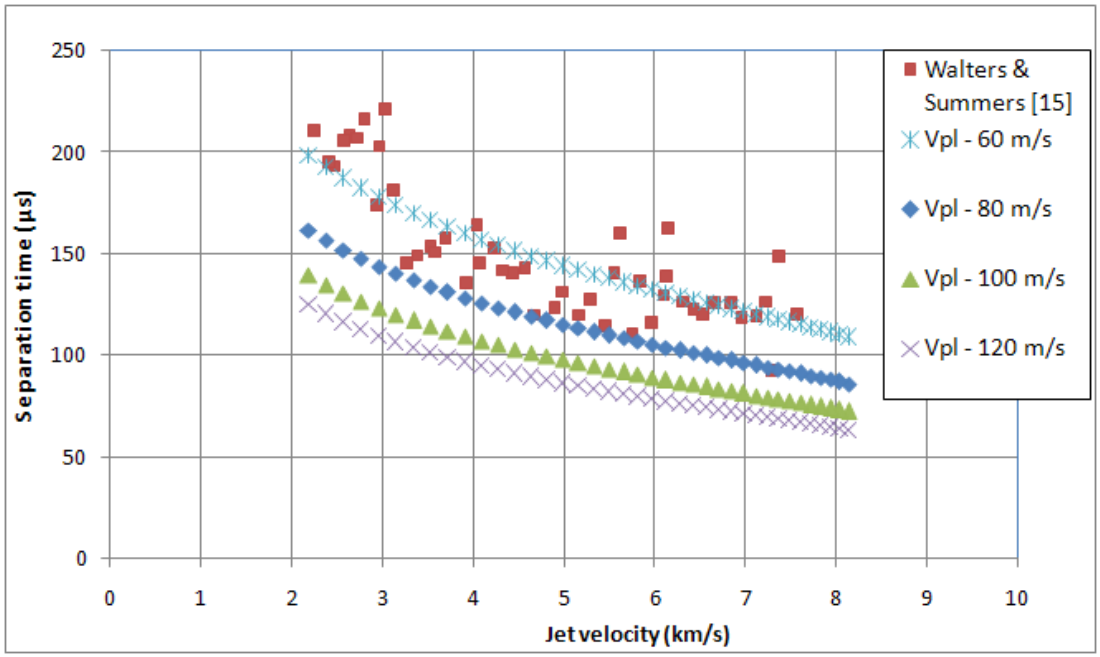

Figure 4-10 Change separation times with V_{pl}

4.2 Failure Model

Up to this point, semi-empirical breakup formulas are discussed, each relating strain, strain rate and jet radius in a different way with breakup time. These semi-empirical formulas generally use constants determined experimentally. Walters and Summers discussed the use of failure strain and stress in breakup calculations, to remove the necessity for the semi-empirical constants [15]. If initial strain and strain rate are known, the time at which a jet element reaches to a determined failure strain can be determined. By the same way, if a constitutive relation is used to describe stress-strain behavior of jet material, it is possible to calculate the time at which a prescribed failure stress is reached.

Walters and Summers used Flash x-ray experimental results of various liner designs to determine the strain to failure of jet segments [15]. It is stated that copper is used as the liner material. The results were based on the experimental jet length L and calculated initial jet length l_0. They stated that the average final true strain of the jet has a constant value of 2.3, calculated as,

$$\varepsilon_F = \ln\left(\frac{L}{l_0}\right) \approx 2.3 \tag{4.1}$$

This amount of elongation corresponds to a necking ratio of 0.32, which is the ratio of the jet radius at the failure to the initial radius. During their studies, the cumulative breakup time is measured as 147.8 μs and calculated as 153 μs, using final true strain value of 2.3 as a failure criterion in breakup calculations.

In Figure 4-11, individual breakup times calculated by the analytical model, using failure strain limits of 1.5, 2.3 and, 3 are given. The closest prediction is obtained by the strain value of 2.3. However it is observed that, increasing behavior of breakup time with decreasing jet velocity is sharper than that observed in the experiments.

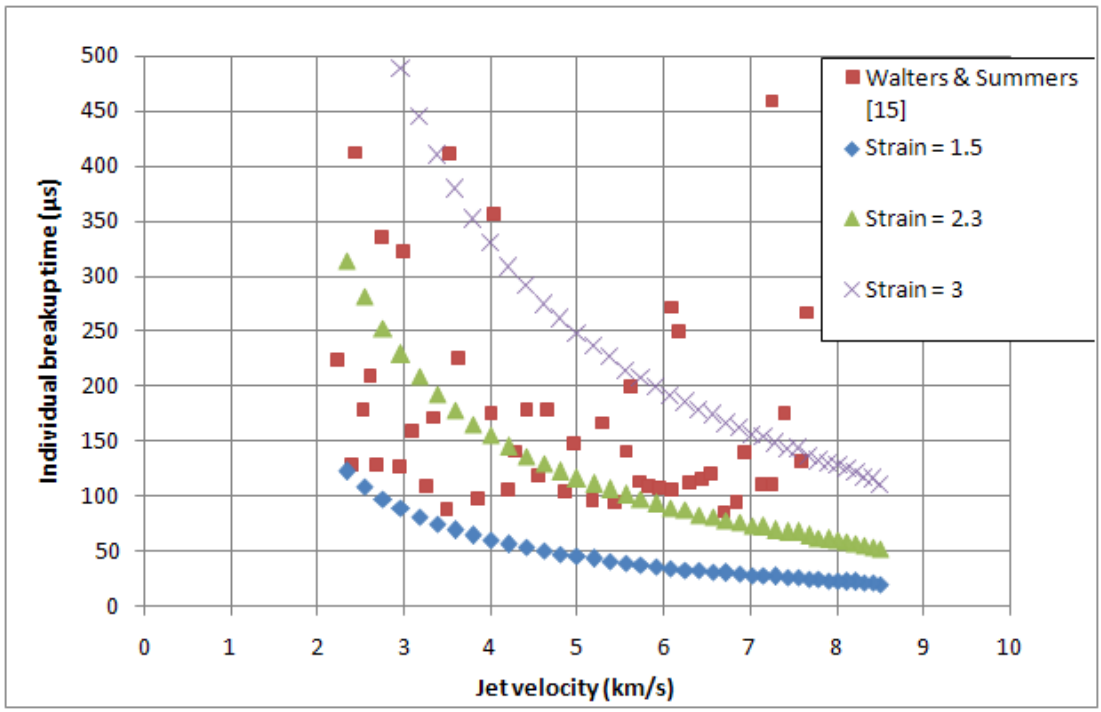

Figure 4-11 Change of individual breakup times calculated with strain limit

Walters and Summers also stated that failure stress of 300 MPa can alternatively be used to describe the breakup criteria for the jet [15]. For this purpose a constitutive model can be used to describe stress-strain behavior of the jet. They used the following Johnson-Cook (JC) and Zerilli-Armstong (ZA) constitutive models, which are given by Equations 4.2 and 4.3 respectively. Tables 4-1 and 4-2 provide the constants used in these models.

$$Y = (A + B\varepsilon^{n})(1 + C ln\dot{\varepsilon})(1 - {T_H}^{m}) \tag{4.2}$$

where,

$$T_H = \frac{T - T_{room}}{T_{melt} - T_{room}}$$

$$\sigma = C_0 + k\lambda^{-1/2} + C_2\varepsilon^{1/2}\exp(-\mathrm{C_3T} + \mathrm{C_4T}ln\dot{\varepsilon}) \quad (4.3)$$

Table 4-1 Constants for the Johnson-Cook constitutive model [15]

A	90	MPa
B	292	MPa
C	0.025	
m	1.09	
n	0.31	
T_{melt}	1396	K
T_{room}	293	K

Table 4-2 Constants for the Zerilli-Armstrong constitutive model [15]

k	5	$\mathrm{MPa(mm)}^{1/2}$
λ	0.075	mm
C_0	0.025	MPa
C_2	1.09	MPa
$\mathrm{C_3}$	0.31	K^{-1}
$\mathrm{C_4}$	0.000115	K^{-1}

Since constitutive models for the jet material depend on temperature also, the effect of temperature on the breakup time is investigated for a fixed breakup failure stress. In Figure 4-12, the comparison of breakup times are given, calculated by JC constitutive model using 450, 600 and 750 K of average jet temperature, for a failure stress of 300 MPa. It is seen in Figure 4-12 that breakup time is highly affected by the jet temperature. Also, average jet temperature assumption of 750 K leads to the closest prediction. In Figure 4-13, comparison of breakup times are given, calculated by JC constitutive model using 300, 350 and 400 MPa of failure stress, for an

average jet temperature of 600 K, to investigate the effect of failure stress on breakup time.

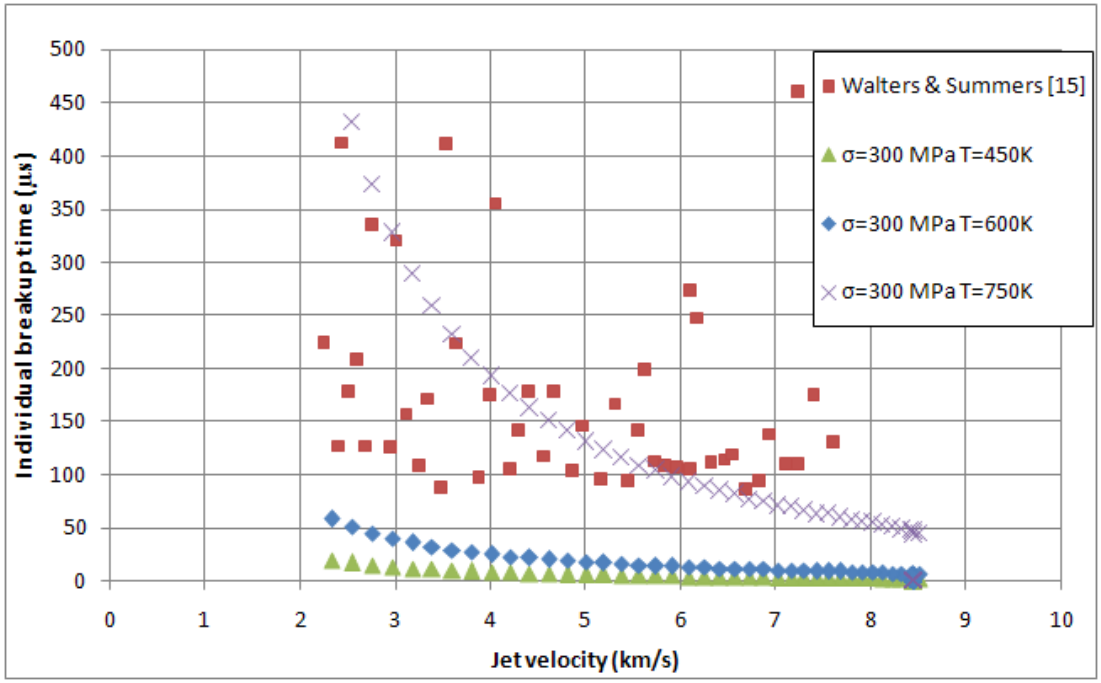

Figure 4-12 Change of individual breakup times with temperature using JC model for σ= 300 MPa

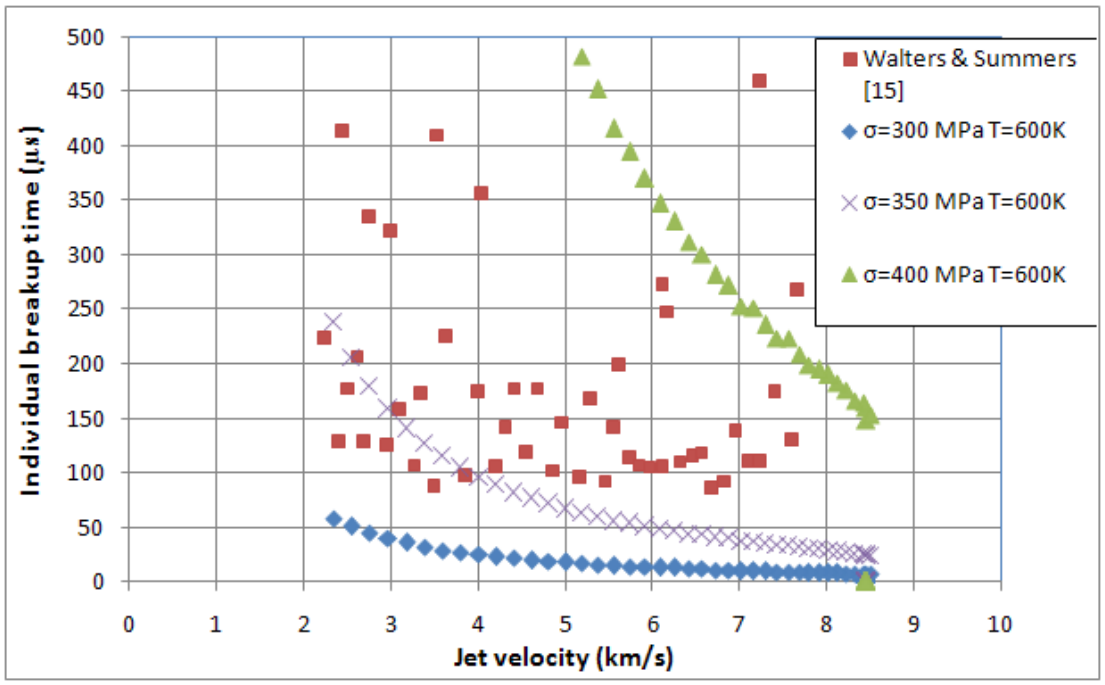

Figure 4-13 Change of individual breakup times with failure stress limit using JC model for T= 600 K

As seen in Figure 4-12, for a failure stress of 300 MPa, average jet temperature should be around 750 K for a good agreement with the experimental data [15]. Also, as seen in Figure 4-13, failure stress should be around 350 MPa for an average jet temperature of 600 K.

For comparison purposes, same calculations for individual breakup time are repeated using Zerilli-Armstrong constitutive model In Figure 4-14, the comparison of breakup times are given, calculated by ZA constitutive model using 450, 600 and 750 K of average jet temperature. As seen in the figure, similar to the calculations with JC model, breakup time is highly affected by the jet temperature. Also, most of the experimental points of individual breakup time is lying between the T=600 K and T=750 K curves, but very close to T=600 K curve. In Figure 4-15, comparison of breakup times are given, calculated by ZA constitutive model using 300, 350 and 400 MPa of failure stress, for an average jet temperature of 600 K.

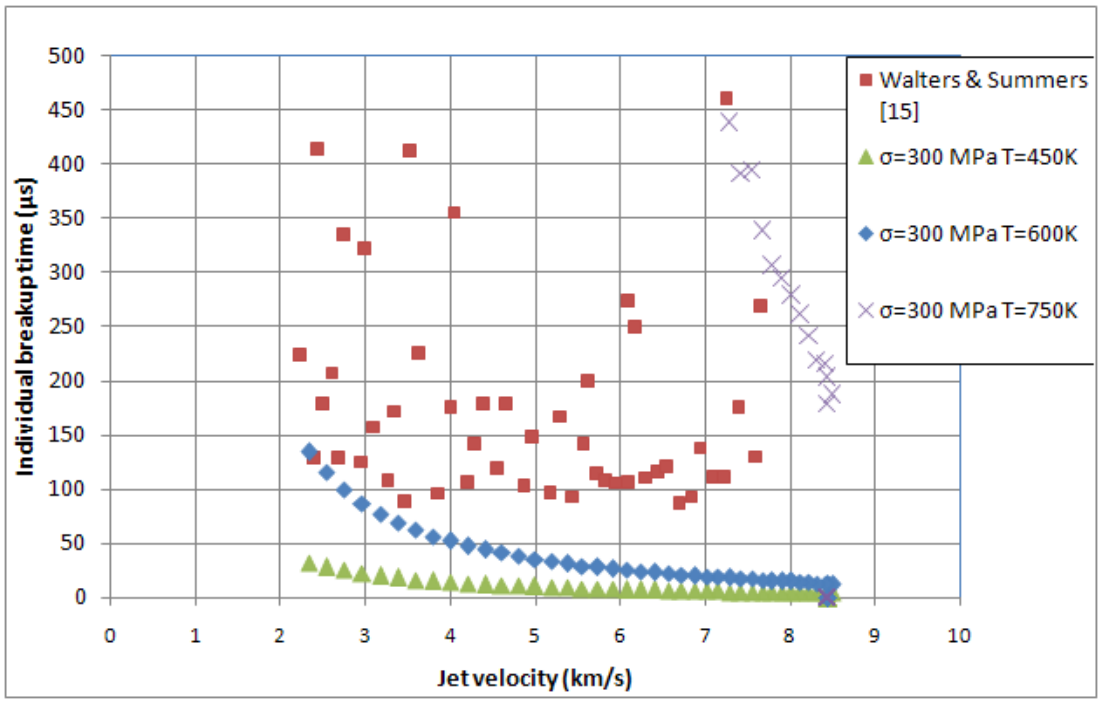

Figure 4-14 Change of individual breakup times with temperature using ZA model for σ= 300 MPa

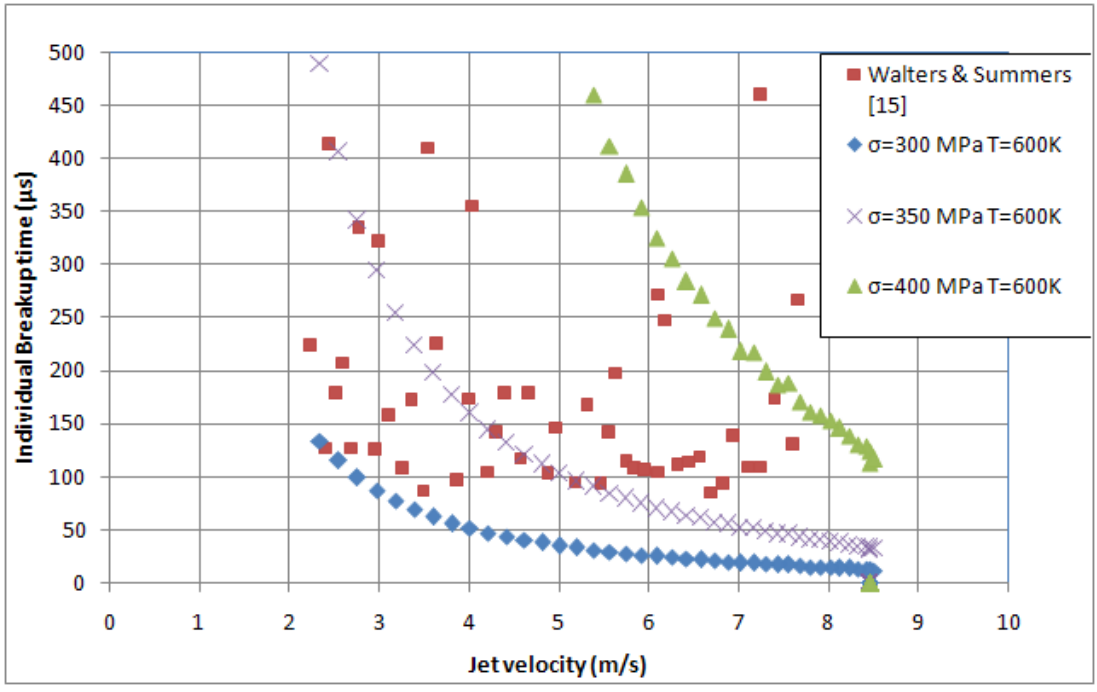

Figure 4-15 Change of individual breakup times with failure stress limit using ZA model for T= 600 K

As seen in Figure 4-14, using ZA constitutive model for a failure stress of 300 MPa, average jet temperature should be around 600 K for a good agreement with the experimental data [15]. However, this temperature seems to be closer to the 750 K using JC model. The reason of this difference is that, in ZA and JC constitutive models, the dependence of stress on temperature is different. As seen in Figure 4-15, using ZA constitutive model, failure stress should be around 350 MPa for an average jet temperature of 600 K, similar to the results in JC model.

4.3 Discussions on Breakup Models

In this chapter four breakup models based on semi-empirical formulas and a breakup model using failure stress-strain as a breakup criterion are investigated. In this part, the results of these calculations will be discussed.

Using V_{pl} model (Hirsch's formulae), both individual breakup and separation times are determined lower than the available experimental data. AUTODYN-Jetting results are close to the experimental data for individual breakup time, however it slightly over predicts the separation time values. V_{pl} model is a simple model and it is relatively easy to apply to any analytical and semi-analytical model like the AUTODYN-Jetting model, and it predicts breakup values with an accuracy that can be used in practical applications. Also, V_{pl} has a physical meaning of velocity difference between successive jet segments. If the value of V_{pl} is measured by a suitable experimental technique, the use of V_{pl} model may lead to considerably well results for jet breakup time. However, since breakup time is independent of initial strain rate in V_{pl} model, its application may be limited in some particular cases like wave shaping. When considering a charge with and without wave shaping, in case of a wave shaping application the only variable in Equation 2-22 is the collapse angle,

since charge diameter and liner thickness are the same. Accuracy of the V_{pl} model may further need to be investigated for wave shaping applications.

Results of analytical model show that, the breakup time calculated by Pfeffer model is almost half of the available experimental data. One possible reason is that the jet radius data is smaller, and strain rate is larger than expected. Results of the AUTODYN-Jetting simulations coupled with the Pfeffer model agree well with the experimental data, although it predicts slightly lower values for the tip region.

Analytical model calculations predict breakup times lower than the experimental values as a general behavior. The agreement with experimental values is good in the tip region, but differences are getting larger from tip to tail of the jet. The AUTODYN-Jetting model results show a good agreement with the experimental data in the region from tip to 5 km/s level. After that point, it shows an unexpected behavior of decreasing breakup times with the decreasing jet velocity. The possible reason is that the strain rate calculated for the tail region of the jet may not be so accurate, as Carleone-Chou model is observed to have a strong dependence on strain rate. However there is no data available in the literature for strain rate to be compared with AUTODYN-Jetting calculations.

Analytic model and AUTODYN-Euler model shows a good agreement with the available experimental data, using Chou breakup model. Analytical model predictions of breakup time are slightly lower than the experimental data, as the general behavior in the other models.

In comparison with semi-empirical formulas, using failure strain and stress is a relatively easy way to calculate breakup time, since there are no experimental constants to be determined or calibrated. The breakup strain criteria stated by Walters and Summers seems to be easiest way of calculating individual breakup time among all breakup models. Because initial strain rate and strain values are already available by analytical model for the jet formation process. Also, breakup strain limit of 2.3 seems to agree well with the experimental results for individual breakup time given by Walters and Summers [15].

Calculations with the analytical model show that a strain limit of 2.3 shows a good agreement with available experimental data. By using failure stress criteria in breakup calculations, the combination that agrees best with experimental data is found to be 350 MPa of failure stress with 600 K average jet temperature. It is observed that the accuracy of breakup time calculations depends on the accuracy of the use of a single average temperature. Because the stress calculated by constitutive models, have a great dependence on temperature. Also, there exists a temperature distribution on the jet, in both axial and radial direction. As a result it is hard to define an average temperature that fits for the breakup calculations for the whole jet. It may be logical to use a temperature distribution in further breakup studies, to increase accuracy of the calculations. The centerline temperature distribution may be used as a first assumption.

Walters and Summers also stated the strong dependence of jet breakup time on jet temperature when using failure stress criteria [15]. They used an average jet temperature of 450 K, however they also stated that calculations show that the jet temperature must be higher than 450 K to fit breakup time with experimental data especially for the tip region of the jet.

In the calculations made by using five different models of breakup time, it is observed that breakup times calculated by analytical model consistently under predicts experimental values as it predicts the general behavior of breakup time. One possible reason is that, the jet radius is calculated lower than the results of AUTODYN-Euler simulations, as discussed in Section 2.1.7. Another possible reason is, in the reference where the experimental data are given, the jet tip velocity is given to be 7.7 km/s whereas it is calculated as 8.3 km/s in this study. Consistent under prediction of breakup times with analytic models may be related to the higher jet velocity, knowing that increasing jet velocity difference between tip and tail decreases breakup time.

CHAPTER 5

ANALYSIS OF PENETRATION

5.1 Numerical Simulation of Penetration

AUTODYN has the capability of solving penetration problems with its Lagrange, Euler, ALE and SPH solvers. Lagrange solvers are generally preferred in simulating penetration problems, for their capability of better solving stress-strain behavior of material through the use of constitutive models and EOS. However, high velocity penetration problems are susceptible to severe mesh distortion when solved with Lagrange solvers. For this reason, erosion criterion needs to be used to have successful Lagrangian simulations. Erosion criterion is previously discussed in Section 2.4.1.

To simulate the penetration performance of the BRL-82 charge, both the jet and the target is modeled with Lagrangian elements. The results of jet formation simulations, performed with the Euler solver (discussed in Chapter 3) are used to determine the properties of the jet. Penetration simulations are performed for a fixed 2 CD standoff distance. The jet material distribution obtained by the Euler solution at 2 CD standoff distance is mapped onto the Lagrange solver using the "part fill" option of AUTODYN. The quality of this Euler-to-Lagrange mapping is limited to the mesh resolution of the Lagrangian jet part.

Dimensions of the 2D axisymmetric penetration model used with the Lagrange solver is given in Figure 5-1. Both the jet and the target parts are modeled using 0.5 mm rectangular elements, as seen in Figure 5-2. However, for the target, mesh is graded in radial the direction after a height of 15 mm to reduce the total element number. 15 mm is a large enough number compared to the much smaller jet radius. In the region that may possibly be in severe plastic deformation during penetration, the mesh is graded smoothly to keep the element shape almost rectangular.

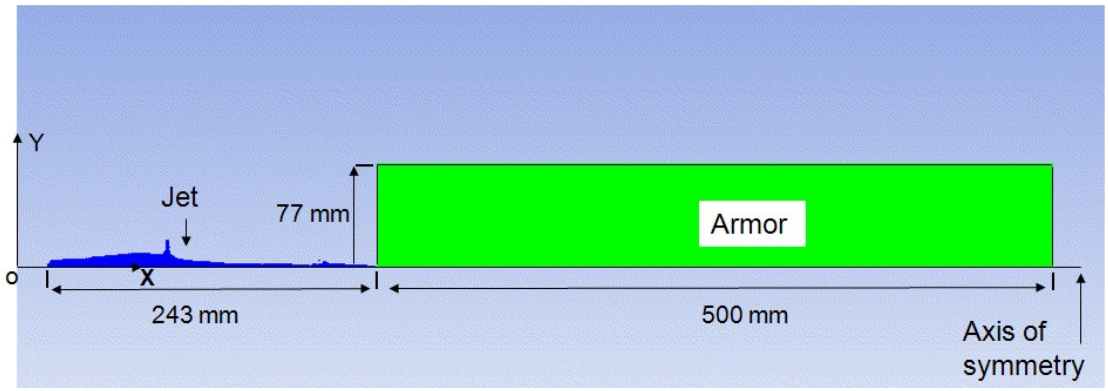

Figure 5-1 Dimensions of the penetration simulation model in AUTODYN-Lagrange solver

Hancock provides penetration data for BRL-82 charge for several standoff distances [19]. It is given that the penetration performance of the charge is 16 inches (~400 mm) against RHA steel at a 2 CD standoff distance. Test results for short standoff distances are important in a way that, jet breakup effects are not so pronounced. By this way, very reproducible test results can be obtained. At larger standoff distances, spread and tumbling of jet particles after jet breakup are more effective, so that charge to charge variations result in a larger spread of test results.

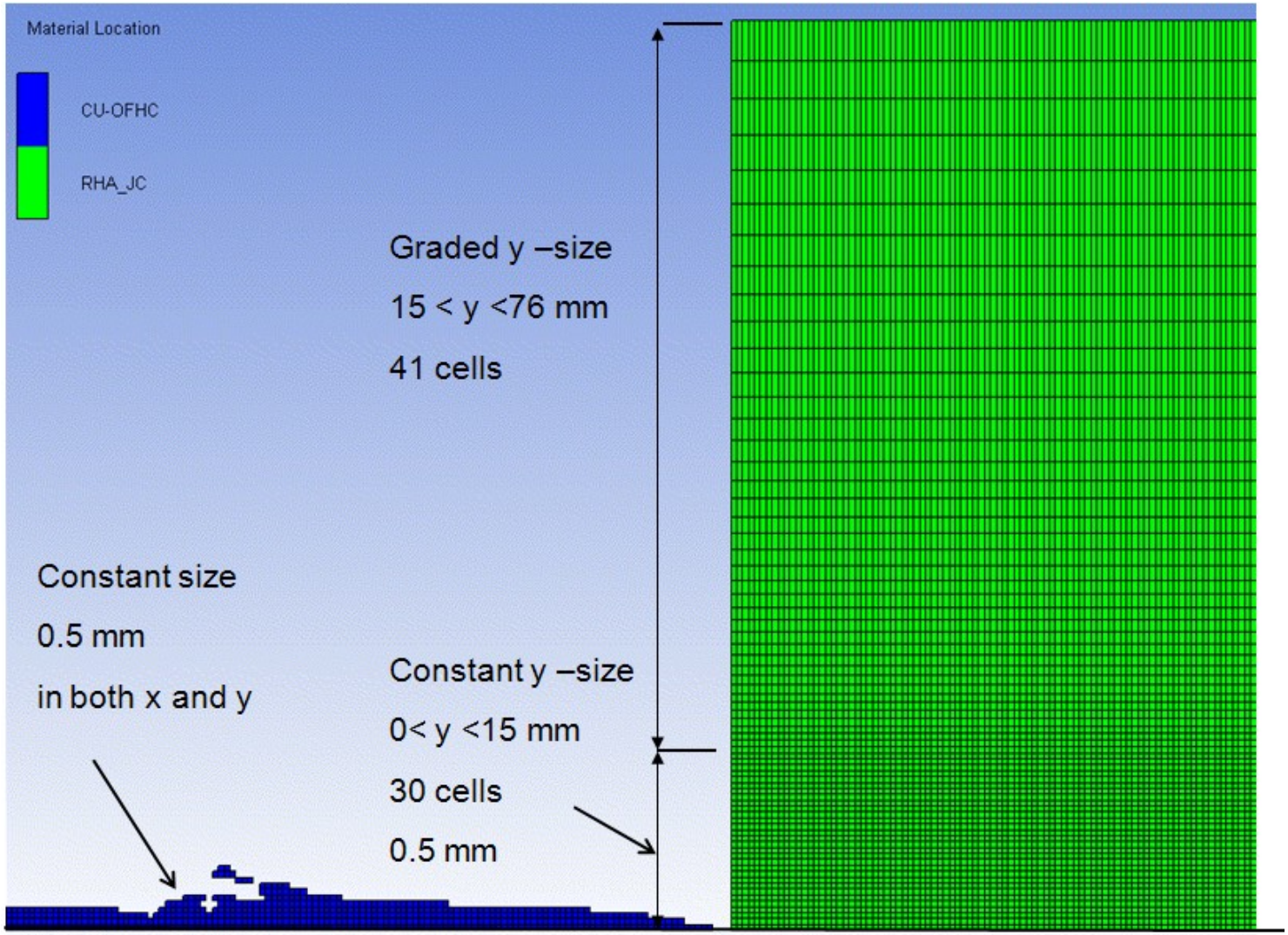

Figure 5-2 Mesh distribution of the penetration simulation model used in Autodyn-Lagrange solver

To compare the results of simulations with experimental data, target is modeled as RHA steel, and the jet is modeled as Cu-OFHC, similar to the study of Hancock [19]. Material parameters are taken from the AUTODYN material library. As discussed in section 4.2, failure strain for the jet material is set to be 2.3.

In the penetration simulations, not only the jet but also the slug region is mapped into the Lagrange model, so that the full range of jet velocities can be obtained. Penetration model is axisymmetric, like the jet formation model, meaning that off-axis velocities of the jet particles can not be simulated. Therefore after the jet breakup all the particles remain on the flight axis, enabling all jet particles to reach the bottom of the penetration crater bottom. In Figure 5-3 jet penetration into target in a typical AUTODYN-Lagrange penetration simulation is shown. In real conditions, due to charge to charge variations and heterogeneities, jet particles may have off-axis velocities and are also subjected to tumbling and spread. As a result, some of the jet particles that move away from the flight axis may hit to the crater walls before reaching the crater bottom, which results in degradation of penetration capability. Velocity of the last particle that reaches crater bottom to deepen penetration is called penetration cut-off velocity. That means, jet particles having velocities lower than penetration cutoff velocity can be no longer deepen penetration. So, penetration cutoff velocity can be used as the limit velocity in the penetration calculations and simulations.

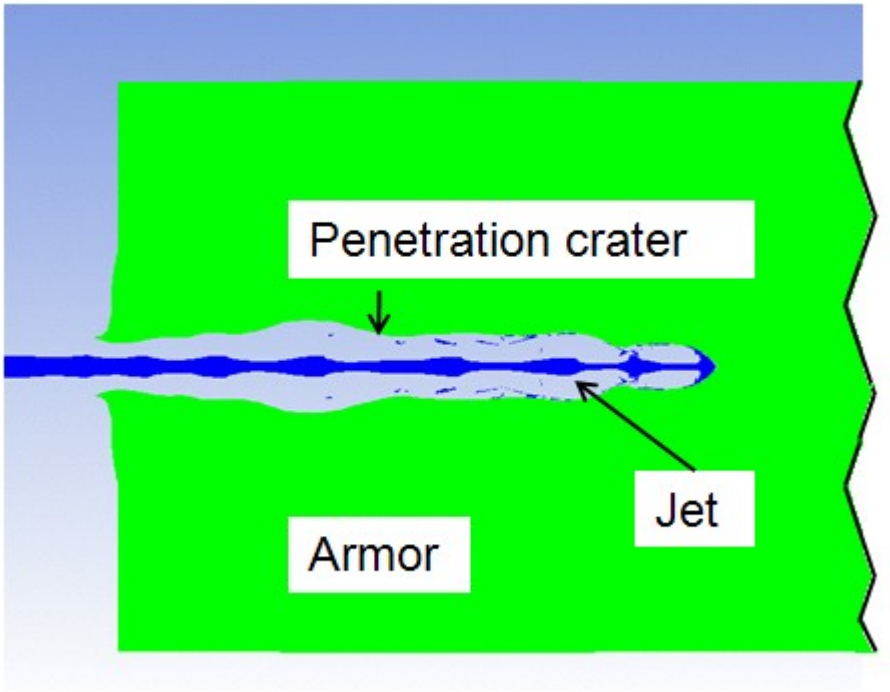

Figure 5-3 Jet penetration into armor in a typical AUTODYN-Lagrange penetration simulation

If a jet particle has an off-axis velocity, the displacement from the axis increases with time after breakup. As a result, the breakup effects become more and more pronounced with increasing standoff distance; so the cutoff velocity is increasing with the increasing standoff distance. In Table 5-2, cutoff velocities of the BRL-82 charge is tabulated as it given in Hancock [19]. Note that, penetration cutoff velocity should not be confused with the hydrodynamic cutoff velocity; defining a velocity limit to hydrodynamic penetration between a certain pair of materials.

Table 5-1 Penetration cutoff velocity for different standoff distances [19]

Standoff distance (CD)	2	5	8	12	15	20	25
V_{cutoff} (km/s)	3.04	3.61	4.01	4.31	4.77	5.69	6.55

Six consecutive simulations are performed to investigate the effect of erosion strain on penetration performance, with the erosion strains of 2, 3, 4, 5 and 6. The penetration depth, crater hole radius and penetration velocities during the penetration are measured in these simulations. Penetration crater profiles of these six simulations are given in Figure 5-4. Penetration depths achieved for different erosion strains are given in Table 5-2. In Figure 5-5 the final penetration depth of the simulation using erosion strain of 4 is shown.

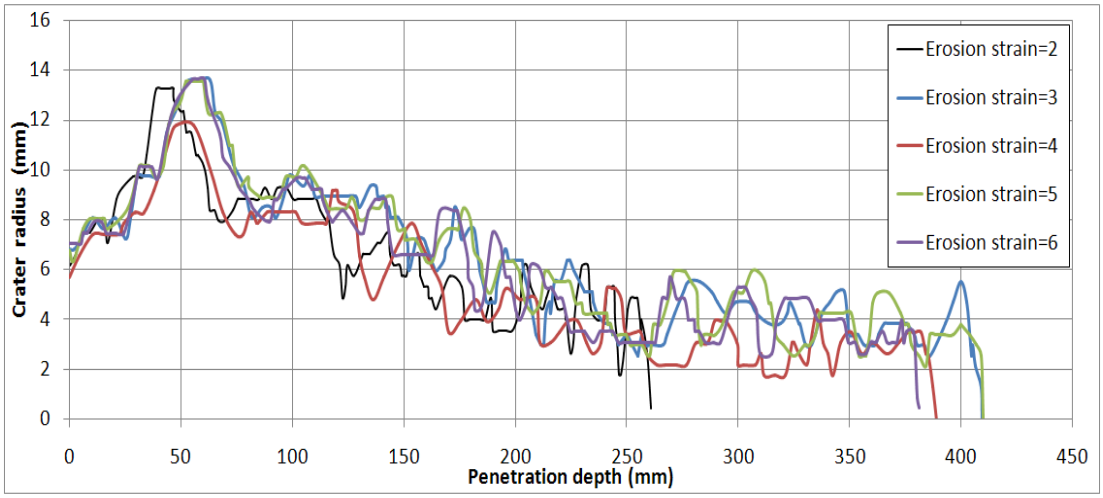

Figure 5-4 Penetration crater profile obtain by AUTODYN simulations for different erosion strains

Table 5-2 Penetration depths for different erosion strains

Erosion strain limit	Penetration (mm)
2	261
3	410
4	390
5	410
6	381

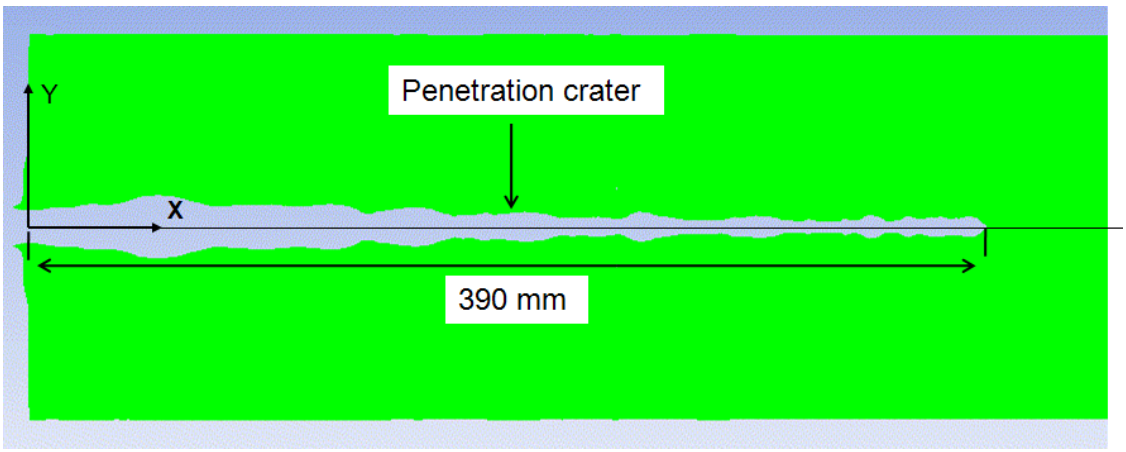

Figure 5-5 Final crater depth for the penetration simulation using erosion strain of four

According to Table 5-2, there is no obvious link between the for penetration depth and the erosion strain. It must be noted that, although incremental strain limit of 2.3 is used as a failure criterion, erosion limit is also serving as an additional failure criterion. As an elements fails, it can not carry tensile stresses anymore. However, a failed element does not erode away if instantaneous strain is less than 2.3. If an element in a necking region of the jet fails, it prevents unrealistic elongation of neighboring elements of the jet since it can not carry tensile forces. As the failed element reaches the crater bottom, it may add to penetration depth under the effect of compressive forces.

Another reason of the unexpected behavior for penetration depth is that, the maximum penetration is measured after the last particle having velocity larger than the cutoff velocity completes penetration. Since this criterion is controlled by the user, the results may have a simulation to simulation variation because the penetration depth is checked from output files written at certain time intervals. For a jet particle a having a velocity range of 2550-2450 m/s, penetration cutoff velocity can be reached at a time between two output files.

Penetration velocities obtained by the simulations are given in Figure 5-6. Note that penetration data is not limited to penetration cutoff velocity, instead, all the data till

the end of simulation is used. This is the reason, why maximum penetration values seem to be different than those given in Table 5-2.

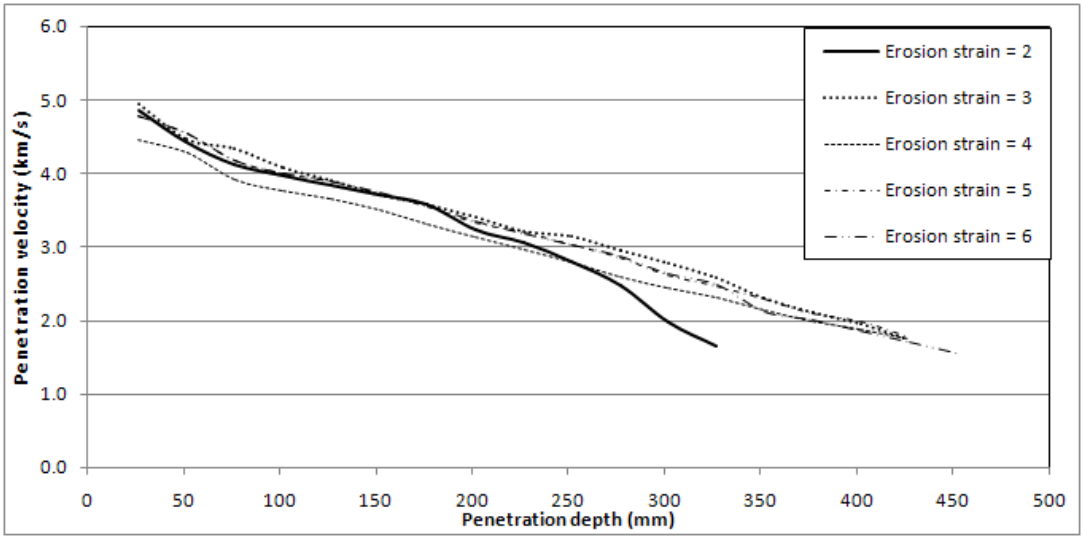

Figure 5-6 Penetration velocities calculated in AUTODYN simulations of different erosion strains

As seen in Figure 5-6, erosion strains of 2 and 3 results in slightly lower penetration velocities. For simulations using erosion strain over and including 4 results in almost the same penetration velocity. It can be concluded that, the erosion strain limit should be selected to be at least 4.

5.2 Analytical Simulation of Penetration

Two different methods of analytical penetration calculation are used. In the first method, named as the Hybrid penetration model, jet data necessary for penetration calculations are acquired from the AUTODYN-Euler jet formation solution. Necessary data is extracted from the AUTODYN simulations using the profile

plotting method with a radial resolution of 0.25 mm. By this way, jet formation and jet elongation calculations are performed accurately with the AUTODYN-Euler solver and the accuracy of penetration results depends mainly on the analytical penetration calculation model. In this method, because of the available data, only Chou model of breakup can be applied.

In the second method, named as full-analytical penetration model, jet data necessary for penetration calculations are also calculated by an analytical jet formation model, as discussed in Section 3.2. In the analytical jet formation model, it is possible to perform jet breakup calculations using different breakup models. In this full-analytical method, jet data is not so accurate as in the AUTODYN-Euler solver, so the error involved in the jet formation calculations are cumulatively added with the errors in the penetration calculations. In Figure 5-7 the flowchart of the analytical penetration calculations are given.

In Table 5-3, results of hybrid penetration method are given, calculated by different analytical penetration models, and compared with the results obtained using AUTODYN-Lagrange solver and the experimental data. It is seen in Table 5-3 that Tate-Alekseevski and Pack-Evans models result in close agreement with the available penetration data. Hydrodynamic theory is over predicting penetration performance as expected, because resistance of target to penetration is neglected. It is seen that the result of Matuska model do not agree with the experimental data. Note that, penetration cut-off velocity of 3 km/s is used in the analytical calculations, similar to AUTODYN simulations.

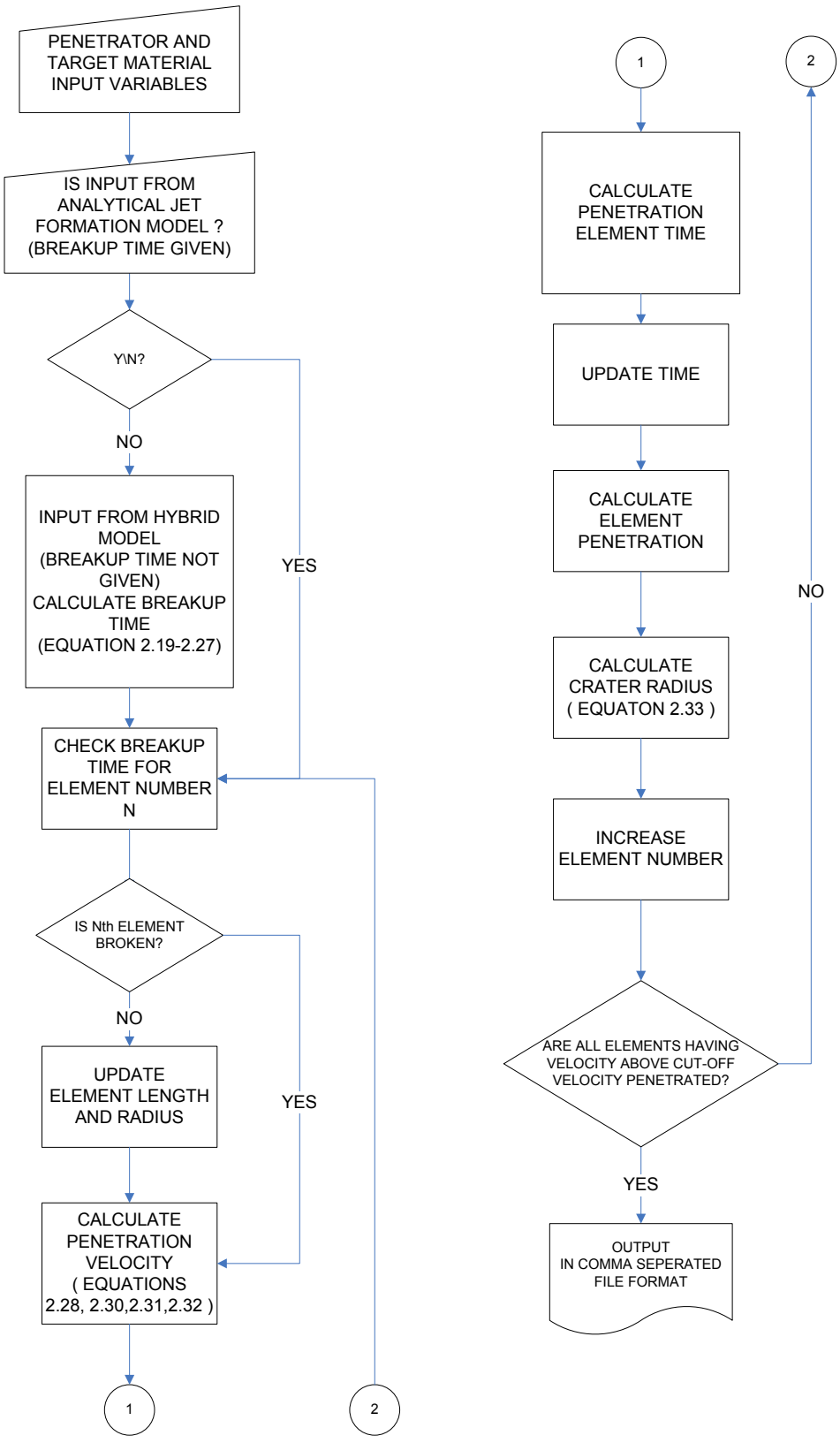

Figure 5-7 Flowchart of analytical penetration calculations

Table 5-3 Penetration depth results for hybrid penetration method

	Penetration (mm)	**Difference w.r.t. experiment(%)**
Hydrodynamic Penetration Formula	490.6	22.3
Tate - Alekseevski	426.9	6.4
Pack - Evans	380.6	5.2
Matuska	569.6	41.9
Experimental [19]	401.3	N/A

Results of analytical penetration calculations with both hybrid and full-analytic methods have a strong dependence on breakup time. The breakup time calculations are discussed in Chapter 4 for both AUTODYN-Euler solver and analytical jet formation model. The leading regions of the jet, where the jet velocity is higher and breakup time is shorter, may penetrate the target before jet breakup occurs. Every penetrating jet element adds to cumulative penetration on the flight direction so that, for the lagging regions of the jet, flight distance is getting longer. Consider a target, at two CD standoff distance. For the first penetrating jet element, flight distance is 2 CD distance. However, for the last penetrating jet element, total flight distance is 2 CD plus total penetration depth. In the analytical calculations, jet elements are assumed to elongate from their formation till breakup time, because of the velocity difference. It is known that, as a jet element elongates, penetration depth increases and crater radius decreases, because of the increased jet length and the decreased jet radius. For these reasons, breakup time, especially for rear jet regions, strongly influences the penetration depth results for analytical calculations.

The penetration depth results of full-analytical method using different analytical penetration models and different breakup models are given in Table 5-4.

Table 5-4 Penetration depths calculated by full-analytical penetration method using different penetration and breakup models

Breakup model	**Penetration model (mm)**			
	Hydrodynamic	**Tate-Alekseevski**	**Pack-Evans**	**Matuska**
Vpl	439.6	402.2	367.1	497.5
Pfeffer	352.5	325.4	298.5	395.8
Carleone-Chou	450.6	415.8	376.9	514.2
Chou	461.2	420.4	381.6	525
Strain=2.3	548.1	485.7	435.3	627.6
Stress -JC	400	366.2	341.8	445.7
Stress -ZA	564.2	491.8	435.3	614.7

Note that, the general behavior of penetration models are similar since the penetration depth models and breakup models do not affect each other. For example, Matuska model always results in deeper penetration depth, followed by the Hydrodynamic, Tate-Alekseevski and Pack-Evans penetration models. For this reason, only the results of the Tate-Alekseevski model is discussed, as it yields better agreement with the available penetration data, and requires less parameters.

Coming to the breakup models, as seen in Table 5-4, V_{pl}, Chou-Carleone and Chou breakup models result in a good agreement with available experimental data. Penetration depth is considerably under predicted by the Pfeffer breakup time model. The possible reason is that, Pfeffer model under predicts breakup time, which results in insufficient elongation of the jet. Shorter jet segments lead to less penetration. Breakup models using stress and strain as failure criteria do not seem to predict available experimental data accurately, with the current stress and strain limits.

Radius of the penetration crater is also calculated analytically. After penetration calculations are complete, crater radius is calculated using penetration velocity and other required target and penetrator data. In Figure 5-8, penetration radius with respect to penetration depth is given for AUTODYN simulations, hybrid and full-analytical penetration model. Since Chou breakup time model is the only available

breakup model for the hybrid penetration model, it is also used in the full-analytical penetration model to achieve comparable results.

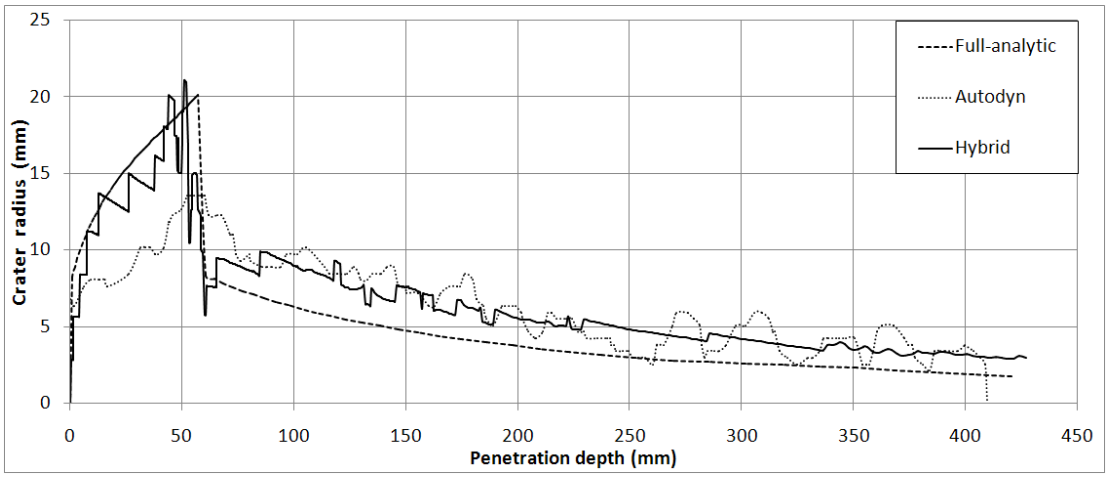

Figure 5-8 Crater radius with respect to penetration depth

As seen in Figure 5-8, Hybrid penetration model predicts both penetration depth and penetration radius successfully, except the entrance region of the hole. However, predictions of the full-analytical model for crater radius are lower compared to AUTODYN-simulations, due to the lower prediction of jet radius throughout its length. As discussed in Section 3.2.3, AUTODYN-Euler simulations result in a wavy profile for the jet. In the analytic jet formation models jet has a smoother radius profile, which results in a smoother crater radius profile.

5.3 Discussion of Penetration Analysis

Penetration performance of the BRL-82 charge at 2 CD standoff distance is simulated by the Lagrange solver of AUTODYN. However, high velocity penetration problems are susceptible to severe mesh distortion using Lagrange

solvers. For this reason, erosion criterion is used to assure the simulation to keep solving problem as the mesh starts to distort. The effect of erosion strain on penetration results are investigated by several simulations using different erosion strains.

Six consecutive simulations are performed to investigate the effect of erosion strain on penetration performance, with the erosion strains of 2,3,4,5 and 6. Penetration depth, crater hole radius and penetration velocities are calculated in the simulations. According to penetration depth and penetration velocity results, erosion strains over and including 4 are acceptable for penetration simulations using Lagrange solver. This observation is also in agreement with the information given in AUTODYN Theory Manual [30]. However, no obvious link is observed between penetration depth and erosion strain.

Four different penetration theories are used along with the hybrid penetration calculation method, which combines jet formation by AUTODYN with analytical penetration calculations. Matuska model of penetration does not agree with the available experimental data with the parameter given in Chou [13]. Pack and Evans model results in slight under prediction of penetration depth. Hydrodynamic model of penetration over predicts penetration depth as expected, since it does not take account of material strength. Tate-Alekseevski model, which also known as modified hydrodynamic penetration model, gives a reasonable prediction of penetration depth. This penetration model is thought to be best model since it requires less parameters to be determined and results in successful predictions.

Penetration depth calculated by analytical models has a strong dependence on breakup time calculations. To investigate the effect of breakup time 6 different breakup models are used along 4 different penetration models with full-analytical penetration method. Again, Tate-Alekseevski model of penetration results in the most reasonable predictions compared to available experimental data. It is shown that accuracy of the breakup time calculation has a great effect on the penetration prediction. Also note that, accuracy of the breakup time especially for the rear regions of the jet has a great importance since the lagging jet segments have more

time to elongate before breakup time, which affects the length of jet segments directly.

Radius of the penetration crater is also calculated by analytical penetration model. Both hybrid and full-analytical methods result in a reasonable prediction for the radius profile of the penetration crater. However, full-analytic model predictions for radius are generally lower than the results of both AUTODYN simulations and hybrid model calculations. Hybrid model prediction for crater radius profile shows an excellent agreement with the results of AUTODYN simulations, except at the entrance region of the hole which is penetrated by the jet tip. The disagreement in the results for hole entrance region is thought to be due to the edge effects in that region since the formula for crater growth does not account for edge effects. In that region, perimeters of the plastic zone reach the boundaries of the target so that semi-infinite target assumption is no longer valid.

CHAPTER 6

CONCLUSION

Shaped charges are explosive devices with great penetration performance. The primary military application of shaped charges is to defeat armor. For this purpose, shaped charge warheads are used in rockets, missiles and tank ammunitions. In the civilian applications, shaped charges are used for oil drilling, mining and demolition.

In the literature there are numerous analytical studies for the calculation of jet formation, breakup and penetration of shaped charges. Also in recent years, due to the increase of the use of the commercial hydrocodes, there are studies on numerical simulation of shaped charge of warheads. However, it is known that weapon technology is considered as highly confidential for national security purposes. Since the primary application of the shaped charge is anti-armor warheads, some critical aspects of analytical formulas and numerical simulations are never given in the open literature. As a result, national level of knowledge is important in shaped charge technology.

It is known that there are numerous studies performed on shaped charge devices and armor systems in Middle East Technical University BİLTİR SAV-SİS center. To the best knowledge of this author there exits one master's thesis and one doctorate dissertation available in open sources, performed at Turkish universities. One of them is focused on analytical analysis of shaped charge jet formation and penetration

performance [10] and the other is focused on numerical simulation of the jet formation [11].

Recent numerical simulation software that are used in shaped charge design can simulate jet formation, breakup and penetration accurately. However, numerical simulation is a time consuming task, requiring considerable amount of computational resources. It requires experienced users for accurate modeling of the problem. It does not allow users to get involved in details of the calculations. Also, generally government permission of supplier countries is needed to purchase these software. As an alternative, analytical calculation methods can be used for quick prediction of shaped charge performance. However, the use of pure analytical tools, without considerable amount of experimental work and diagnostic techniques, may result in inaccurate performance prediction. Also, use of analytical tools may be limited to simple geometries, as there is a lack of theoretical formulas to apply for complex geometries. It is concluded that, both numerical and analytical tools are essential is shaped warhead design.

For this purpose, in this thesis work; both numerical simulation and analytical calculation methods are used. The aim is to compare available alternative methods for shaped charge performance prediction and suggest ways to use numerical and analytical tools together. BRL 82 charge is used for all the analyses.

AUTODYN-Euler solver is used for the numerical simulation of jet formation AUTODYN. The simulation model is two-dimensional and axi-symmetric. To investigate sensitivity of the problem to the mesh size, successive simulations are performed by decreasing mesh size. It is calculated that as mesh size approaches to zero, jet tip velocity approaches to 8800 m/s. However, it is observed that mesh size smaller than 0.25 mm is impractical to be run on standard workstations, for both computational resources requirement and computation time. For the cell size of 0.25 mm, simulations results in a good agreement with the available experimental jet tip velocity data given by Bolstad and Mandell [3].

To speed-up the solution of the jet formation process , simulations are performed both with and without air. Computational resource requirement is considerably higher for the case with air. It is shown that for short standoff distances such as three calibers or less, there is only a small difference of jet tip velocity which is acceptable for most practical applications. However, for the standoff distances longer than 3 calibers, jet tip velocity difference between simulations with and without air increases. In the simulation with air, it is calculated that jet tip velocity is decaying with a linear rate, which may be attained to air drag. However, it is thought that this observation needs further investigation.

To decrease computational resource requirement by decreasing total amount of cells used, elongated cell are used in the jet elongation region of the numerical model. According to the results of simulations, it is concluded that simulation time can be reduced by using elongated cells for practical standoff distances. However, the data resolution is lost in the jet elongation direction when elongated cells are used and care must be taken if the jet formation data is used further in other simulation or calculation steps.

Jet formation simulations using AUTODYN-Euler solver results in accurate prediction of jet tip velocity and velocity distribution. However, jet formation variables such as collapse velocity, collapse and deflection angles can not be measured directly. For this purpose, jetting option in AUTODYN-Euler solver is invoked. With jetting option, jet tip is predicted accurately; however, collapse velocity and collapse angle has a slight disagreement with the available data in Walters and Zukas [5]. The main reason is predicted to be the shift of maximum collapse velocity point towards the base of the cone. With the jetting of AUTODYN-Euler solver option, only the collapse of the liner is simulated numerically and jet properties are calculated analytically. As a result, faster simulations can be performed with a slight loss of accuracy in the predictions. Eventually, jetting option can be used to compare large number of alternative designs, to narrow down the alternatives.

Analytical jet formation predictions are compared with the results of numerical simulations and available data in the literature. The constants for the exponential acceleration formula are calculated using data acquired form the AUTODYN-Euler simulations using jetting option. Maximum collapse velocity is predicted accurately, however, maximum collapse velocity point is shifted towards the apex of the cone. The jet tip velocity and velocity distribution is in a good agreement with the both numerical simulations and available data in the literature.

Five different jet breakup models are used to investigate the capability of the analytical breakup formulas in predicting breakup time. The breakup calculations using jet data form the AUTODYN-Euler simulation, AUTODYN-Jetting calculations and analytical calculations are compared with the data given by Walters [15]. It can be concluded that, V_{pl} and Chou models of breakup results in most accurate prediction of breakup time. Although Carleone-Chou breakup model has a broader range of application because it is related to strain and strain rates, its accuracy in prediction of breakup also depends on the accuracy on strain and strain rate calculations [5]. Results of Preffer breakup model does not agree with the available data, with the current constants use in the calculations. By using a suitable strain limit as a failure criteria for the jet, breakup time can be accurately calculated. However, when stress is used as a failure criteria, a suitable constitutive equation must be used to relate strain to the stress on the jet since strain is availably calculated in the analytical jet formation calculations. However, dependency of the stress on temperature in the constitutive equations results in considerable variation of breakup time with the average temperature assumption of the jet.

Penetration calculations are performed in three different ways. In all methods jet breakup is calculated analytically. In the first method, jet data obtained by the AUTODYN-Euler simulation is transferred in to the AUTODYN-Lagrange solver by which penetration simulation is performed. The result of simulations shows a good agreement with the available data in the literature.

In the second method, the jet data obtained by the AUTODYN-Euler simulation is used to perform analytical penetration calculations. By this way, results of accurate AUTODYN-Euler solutions are coupled with quick analytical penetration calculations. The results are in good agreement with both numerical simulation results and data available in the literature.

In the third method jet data is taken from the analytical jet formation calculations. In this method accuracy of the penetration calculations have a great dependency on the accuracy of both jet formation and breakup calculations. It is concluded that, penetration performance of the shaped charge jet can be calculated with an acceptable level of error for practical purposes.

Crater radius is also calculated for three penetration methods. The results are in a good agreement, except for the entrance region of the penetration hole.

In this thesis work different ways of modeling and simulating shaped charge performance are discussed in with the focus of anti-tank shaped charge design. It can be concluded that; both numerical and analytical models must be used together for an effective warhead design. Use of analytical calculation methods in shaped charge design is essential for their capability of providing quick estimations and for letting the user to get involved in the details of the calculation. With an accurate analytical calculation method, it may be possible to employ optimization procedures on shaped charge design variables.

By using numerical simulation software, it is possible to accurately predict shaped charge performance for jet formation, breakup and penetration. Commercial numerical software generally have their own libraries of material formulations and constants. Also it is easier to handle complex geometries with numerical simulation software. Eventually, numerical software is also essential in shaped charge design for their accuracy and flexibility.

It is also possible to create a connection between numerical simulations and analytical calculations by suitable means. In the present work, output of jet formation analysis by AUTODYN-Euler (with and without jetting option) is used as an input for the analytic breakup and penetration calculations. This method is called as hybrid penetration calculation method. Analytic jet formation analysis is more complex than breakup and penetration analysis; in number of equations used to formulate the problem and number of constants to be determined in the equations. By the suggested hybrid penetration calculation method, jet formation can be handled by accurate AUTODYN-Euler solver; after which breakup and penetration calculations can be handled by a fast analytical method with an acceptable level of error.

Accuracy of both analytical and numerical methods can be evaluated and possibly improved by performing experiments and measuring the necessary information. Experimental jet tip velocity and velocity distribution can serve a great feedback for the jet formation and breakup analysis. Also by measuring penetration velocity in the target, accuracy of penetration calculations can be evaluated and improved by improving material model constants used in numerical simulations and material resistance terms used in analytical calculations.

6.1 Further work

In the jet formation calculations, detonation wave is assumed to be planar, which is perpendicular to the explosive casing and central axis of the charge. This kind of a detonation wave can be achieved by suitable initiation techniques and devices; however it is not practical for the real life applications. Generalized PER theory can be used to account for a different initiation of explosive. By this way it may also be possible to employ analytical calculations for wave shaper applications.

In case of liner acceleration, the formulas that are used in the current work do not take the presence of casing (confinement effect) into account. For a better estimation

of collapse velocity, especially for the base region of the cone, an equivalent explosive thickness approach may be employed. Alternatively, collapse velocity formulas that use casing mass as a variable can be used.

In current work, breakup of the jet is studies only with analytical methods. It may be possible to simulate jet breakup with numerical simulations, with comparisons against analytical calculations and experimental results.

For the breakup calculations using stress limit as a failure criterion, an average temperature for the whole jet is assumed. However, jet temperature is changing along both axial and radial directions. A constant temperature for each axial element may be taken as an average of temperature distribution in radial direction. By this way, it is possible to use a variable temperature along jet length. Temperature data can be obtained from numerical jet formation simulations.

For the numerical simulation of penetration, AUTODYN-Lagrange solver is used. Other solvers of AUTODYN (Euler, ALE and SPH) can also be used in penetration calculations. Target and penetrator can be either modeled by the same or different solvers.

REFERENCES

1. Joseph Carleone, Tactical Missile Warheads, American Institute of Aeronautics and Astronautics Inc, 1993

2. Walters, William, A Brief History of Shaped Charges, 24th International Symposium on Ballistics, New Orleans USA, 2008

3. Bolstad, J., Mandell, D., Calculation of Shaped Charge Jet Using MESA-2D and MESA-3D Hydrodynamic Computer Codes, Los Alamos National Laboratory, New Mexico, 1992

4. Murphy, M.J., Shaped Charge Penetration in Concrete : A Unified Approach, University of California, Davis, 1983

5. Walters, W. , Zukas, J.A, Fundamentals of Shaped Charge Jets, John Wiley and Sons, 1989

6. Birkhoff, G. , MacDougall, D.P., Pugh, E.M., Taylor, Sir G., Explosives with Lined Cavities", Journal of Applied Physics, 19, 563-582, 1948

7. Complete Guide : Do-it-all Anti-armour?, Armada International Journal, 2006

8. Ogorkiewicz, R., Technology Options for Increasing against the Contemporary Treat-Treat Weapons, Fundamentals of Armoured Protection-Cranfield University UK, 2007

9. Ogorkiewicz, R., Technology Options for Increasing against the Contemporary Treat-Armor, Fundamentals of Armoured Protection-Cranfield University UK, 2007

10. Özel, S. , Formation and Penetration of the Shaped Charge Jets, Ms. Thesis, Mechanical Engineering Department, Middle East Technical University, 2000

11. Aksoy, G.İ. , Çukur İmla Teknolojisinde Metal Çökmesinin İncelenmesi, PhD. Thesis, Mechanical Engineering Department, Atatürk University

12. Baker, E., Modeling and Optimization of Shaped Charge Liner Collapse and Jet Formation, PhD. Thesis, Washington State University, 1992

13. Chou, P.C., Flis W.J, Recent Developments in Shaped Charge Technology, Propellants, Explosives, Pyrotechnics, 11, 99-114, 1993

14. Chanteret, J.P., Considerations About the Analytical Modeling of the Shaped Charges, Propellants, Explosives, Pyrotechnics, 18, 337-344, 1993

15. Walters, W. , Summers, R.L., A Review of Jet Breakup Models, Propellants, Explosives, Pyrotechnics, 18, 241-246, 1993

16. Pappu, S., Hydrocode and Microstrustural Analysis of Explosively Formed Penetrators, PhD Dissertation, University of Texas at El Paso , 2000

17. Rosenberg, Z., Dekel, E., On the Role of Material Properties in the Terminal Ballistics of Long Rods, International Journal of Impact Engineering, 30, 835-851, 2004

18. Rosenberg, Z., Dekel, E., The Penetration of Rigid Long Rods-revisited, International Journal of Impact Engineering, 36, 551-564, 2009

19. Hancock, S.L, Extension of the UMIN Model for Cutoff of High Precision Jets, International Journal of Impact Engineering, 26, 289-298, 2001

20. Held, Manfred, Kozhushko, A.A. , Radial Crater Growing Process in Different Materials with Shaped Charge Jets, Propellants, Explosives, Pyrotechnics, 24, 339-342, 1999

21. Kleinhanss, H.R., Experimentelle Untersuchungen zum Kollapsprozess bei Hohlladungen, Proceedings of the Third International Symposium on Military Application, English Translation, Army Foreign Science and Technology Center, Report no FSTC-HT-23-794-73, March 1973

22. Duvall, G.E., Erkman, J.O., Technical Report No.1, Stanford Research Institute, 1958

23. Mikhailov, A.N., Dremlin, A.N., Flight Speed of Plate Propelled by Products From Sliding Detonation, Fizika Gorenia I Vzryva, 10, 877-884, 1974

24. Shushko, L.A., Shekter, B.I., Krys'kov, S.L., Bending of a Metal Strip by a Sliding Detonation Wave, Fizika Gorenia I Vzryva, 11, 264-274, 1975

25. Randers-Pehrson, G. , An Improved Equation of Calculating Fragment Projection Angle, Proceedings of 2nd Symposium on Ballistics, Daytona Beach-USA, 1976

26. Taylor, G.I., Analysis of Explosion of a Long Cylindrical Bomb Detonated at One End, Scientific Papers of Sir G.I.Taylor, Vol.III, 277-286, Cambridge University Press, 1941

27. Pugh, E.M., Eichelberger, R.J., and Rosteker, N., Theory of Jet Formation by Charges with Lined Conical Cavities, Journal of Applied Physics, 23, 532-526, 1976

28. Hirsch, E., Scaling of the Shaped Charge Jet Break-up Time, Propellants, Explosives, Pyrotechnics, 31, 230-233, 2006

29. Pack, D.C., Evans, W.M., Penetration by High Velocity Jets: I, Proceedings of Physics Soc. (London), B64, 198

30. AUTODYN Theory Manual, ANSYS-Century Dynamics, Rev.4.3, 2005